NPS-69-87-012

AD-A191 226

NAVAL POSTGRADUATE SCHOOL
Monterey, California

UNSTEADY FLOW ABOUT CAMBERED PLATES

T. SARPKAYA

S. I. M. MOSTAFA

P. D. MUNZ

October 1987

Final Report for Period October 1986-October 1987

NAVAL POSTGRADUATE SCHOOL
Monterey, California

Rear Admiral R. C. Austin   K. T. Marshall
Superintendent   Acting Provost

    Reproduction of all or part of this report is
authorized.

    This report was prepared by:

                                TURGUT SARPKAYA
                                Distinguished Professor
                                of Mechanical Engineering

Reviewed by: Released by:

Anthony J. Healey, Chairman   G. E. Schacher, Dean of
Department of Mechanical   Science and Engineering
Engineering

A191 226

REPORT DOCUMENTATION PAGE

1a REPORT SECURITY CLASSIFICATION Unclassified	1b RESTRICTIVE MARKINGS
2a SECURITY CLASSIFICATION AUTHORITY	3 DISTRIBUTION/AVAILABILITY OF REPORT Approved for public release: distribution unlimited.
2b DECLASSIFICATION/DOWNGRADING SCHEDULE	

4 PERFORMING ORGANIZATION REPORT NUMBER(S) NPS-69-87-012	5 MONITORING ORGANIZATION REPORT NUMBER(S)

6a NAME OF PERFORMING ORGANIZATION Naval Postgraduate School	6b OFFICE SYMBOL (If applicable) 69SL	7a NAME OF MONITORING ORGANIZATION Sandia National Laboratories

6c ADDRESS (City, State, and ZIP Code) Monterey, CA 93943-5000	7b ADDRESS (City, State, and ZIP Code) Albuquerque, NM 87185

8a NAME OF FUNDING/SPONSORING ORGANIZATION Sandia National Laboratories	8b OFFICE SYMBOL (If applicable)	9 PROCUREMENT INSTRUMENT IDENTIFICATION NUMBER DN-04-2212

8c ADDRESS (City, State, and ZIP Code) Albuquerque, NM 87185	10 SOURCE OF FUNDING NUMBERS			
	PROGRAM ELEMENT NO	PROJECT NO	TASK NO	WORK UNIT ACCESSION NO

11 TITLE (Include Security Classification)
Unsteady Flow About Cambered Plates

12 PERSONAL AUTHOR(S) T. Sarpkaya, S. I. M. Mostafa, P. D. Munz

13a TYPE OF REPORT Final	13b TIME COVERED FROM 10/86 TO 10/87	14 DATE OF REPORT (Year, Month, Day) 1987/10/01	15 PAGE COUNT 174

16 SUPPLEMENTARY NOTATION

17	COSATI CODES		18 SUBJECT TERMS (Continue on reverse if necessary and identify by block number)
FIELD	GROUP	SUB-GROUP	Unsteady flow, Discrete Vortex Model, Cambered plate, Parachute, Experiments, Analysis

19 ABSTRACT (Continue on reverse if necessary and identify by block number)

Impulsively-started uniform flow, decelerating at specified rates, about two-dimensional cambered plates with included angles of 120, 180, and 240 degrees has been investigated both theoretically and experimentally. The experiments were conducted in a vertical water tunnel. The forces acting on the cambered plates have been determined as a function of the relative displacement of the fluid. The evolution of the vortices was visualized by means of various dyes and polystyrene beads. A numerical analysis was carried out through the use of the discrete vortex model. Vorticity is represented by a distribution of discrete line vortices. Each vortex is convected in the velocity field according to the Biot-Savart law. The rollup of the vortex sheets, the distribution of velocity and pressure on the cambers, and the drag and lift forces are calculated at suitable time intervals for a prescribed time-dependent flow. The results are compared with those obtained experimentally.

20 DISTRIBUTION/AVAILABILITY OF ABSTRACT [X] UNCLASSIFIED/UNLIMITED ☐ SAME AS RPT ☐ DTIC USERS	21 ABSTRACT SECURITY CLASSIFICATION Unclassified
22a NAME OF RESPONSIBLE INDIVIDUAL T. Sarpkaya	22b TELEPHONE (Include Area Code) (408) 646-3425	22c OFFICE SYMBOL 69SL

DD FORM 1473, 84 MAR   83 APR edition may be used until exhausted   SECURITY CLASSIFICATION OF THIS PAGE
All other editions are obsolete

SUMMARY

A theoretical and experimental investigation of an Impulsively-started uniform flow, decelerating at specified rates, about two-dimensional cambered plates with included angles of 120, 180, and 240 degrees has been carried out.

The results have shown that:

1.   For a given camber, the drag coefficients prior to the onset of deceleration are nearly identical.   The drag coefficients after the onset of deceleration are simply shifted in time by an amount equal to the difference between the durations of their steady states.

2.   For the Models A (120 degree camber) and B (180 degree camber), the drag coefficient decreases rapidly at the onset of deceleration, goes through zero near the middle of the deceleration period, and through a negative value at the end of the deceleration period.   Then, the drag coefficient gradually decreases to zero.

3.   For the Models A and B, the flow separates at the sharp edges right from the start and remains there throughout the rest of the motion.   Two, highly stable, symmetrical, primary vortices form and continue to grow during the periods of initial acceleration and subsequent steady fluid motion.   The regions of secondary flow near the rear edges of the camber are quite small.   During the period of deceleration, the vortices move towards the camber, develop three-dimensional instabilities, and give rise to oppositely-signed circulation at the edges of the camber.   Subsequently, the vortices continue to move sideways and the force acting on the camber reduces to zero as the vortices are diffused by both molecular and turbulent diffusion.

4.   For the Model C (240 degree camber), the initial rise in the drag coefficient is followed by a sharp decrease and then by a rise to a larger maximum. Subsequently, the drag coefficient decreases rapidly at the onset of deceleration, goes through zero near the middle of the deceleration period, and through a relatively small (negative) minimum value at the end of the deceleration period.

5.   For the Model C, the flow does not separate immediately at the sharp edges of the camber.   The separation begins at the bottom stagnation point and leads to the formation and growth of two small vortices. Subsequently, these vortices move towards the rear of the camber (the time at which the drag coefficient decreases

sharply) and the separation points move rapidly to the edges of the camber. Then two large primary vortices develop and quickly swallow the two small ones. As in the case of the Models A and B, the vortices become three dimensional during the period of flow deceleration.

6. For all models, the occurrence of a negative drag force during the second half of the deceleration period is thought to be one of the major reasons for the inception of the parachute collapse.

7. The discrete vortex model developed in the present investigation can be used to predict the characteristics of time-dependent flows about cambered plates with relatively small included angles (e.g., 120 deg.). The predictions of the model and the drag coefficient in particular, become poorer, particularly in the later stages of a decelerating flow, as the camber angle increases. This is attributed to three primary reasons: occurrence of rear-face separation, development of three-dimensional instabilities in the vortices, and the effects of molecular and turbulent diffusion.

8. The evolution of the wake is remarkably similar (including the formation of the secondary vortices at the sharp edges) to that obtained in flow visualization experiments.

9. The drag coefficient calculated through the integration of the instantaneous pressure distribution agrees more closely with that obtained experimentally.

10. The development of negative differential pressures near the central region of the camber is thought to be primarily responsible for the inception of the partial collapse of a parachute at high rates of deceleration. This phenomenon takes place even when the total drag force acting on the parachute is still positive. Extensive analysis and small scale experiments coupled with few judiciously selected field tests may help to arrive at practically and phenomenologically sound parachute designs.

2

ACKNOWLEDGEMENTS

Accesion For		
NTIS CRA&I		☑
DTIC TAB		☐
Unannounced		☐
Justification		
By		
Distribution /		
Availability Codes		
Dist	Avail and/or Special	
A-1		

3

TABLE OF CONTENTS

LIST OF FIGURES

6

9

TABLE OF SYMBOLS AND ABBREVIATIONS

$4b$	Chord Length of the Cambered Plate
C_d	Drag Coefficient, $D/(2\rho bU_0^2)$
C_l	Lift Coefficient
C_p	Pressure Coefficient
c	Radius of the Circular Cylinder
D	Drag Force per Unit Length
F	Total Drag Force
i	$= \sqrt{-1}$
L	Active Length of the Camber
q	Velocity Vector
p	Pressure
$R[\ ]$	Real Part of a Complex Quantity
Re	Reynolds Number
r	Radial Distance
T^*	Normalized Time, $U_0 t/c$
t	Time
U	Velocity
U	Acceleration, dU/dt
U_0	Steady Ambient Velocity
U_s	Velocity at Separation Point
u	x-Component of Velocity
V_1	Tip Velocity
V_2	Velocity at the Inner edge of the Shear Layer
V_t	Tangential Velocity Component
v	y-Component of Velocity

W	Complex Potential Function
z	$= x + iy$
z_n	Location of the n-th Vortex
z_t	Tip Coordinate in the Physical Plane
t	Time Increment
Γ_n	Circulation of the n-th Vortex
2α	Included Camber Angle
ϵ	Radial Incremental Location of the Nascent Vortex
ζ	$= \xi + i\eta$, Nondimensional Location in the Circle Plane
ζ_t	Coordinate of the Edge of the Camber in the Circle Plane
ζ_o	Location of the Nascent Vortex in the Circle Plane
θ	Angular Coordinate Measured Counter-Clockwise
θ_s	Angular Position of the Separation Point
ν	Kinematic Viscosity
ρ	Density of Water

DECELERATING FLOW ABOUT CAMBERED PLATES

1   INTRODUCTION TO EXPERIMENTS

The determination of the deployment sequence of an axisymmetric porous parachute and the unsteady aerodynamic loads acting on it presents a very complex coupled problem. The development of an analytical or numerical model which takes into account the effects of porosity, gaps, and variable opening schemes would allow numerical experiments on a large class of parachutes, reduce the number of the expensive field tests to a few judiciously selected ones, and enable the designer to calculate the time history of the fall of the parachute and the strength required to survive the aerodynamic loads. However, the development of such a model is hampered by a number of difficulties, the most important one being the lack of controlled laboratory experiments. It is in light of the foregoing that one acquires a greater appreciation of the difficulties associated with the solution of the aforementioned coupled problem and of the ingenious approximations introduced into the early models during the past two decades.

The previous models for parachute loads are based by and large on empirical assumptions (see e.g., McVey 1972;

Heinrich and Saari 1978; Cockrell 1987). They rely on the observation that families of parachutes open in a characteristics length and seem to have aerodynamic properties that relate well to the projected area of the parachute. The apparent mass is assumed to be a function of the projected area only and is not a function of the prevailing flow characteristics. The vortex sheet analysis was used by Klimas (1977) to derive the acceleration-independent apparent mass coefficient for arbitrary-shaped axisymmetric surfaces. Muramoto and Garrard (1984) used a continuous-source model to predict the steady-state drag of ribbon parachutes. These analyses did not, however, deal with the evolution of the unsteady wake and its interaction with the canopy.

It is in view of the foregoing that an experimental study of the separated time-dependent flow about two-dimensional rigid cambered plates was undertaken. Clearly, the flow about a rigid cambered plate is considerably simpler than that about a porous, axisymmetric, and flexible parachute and the experimental data, regardless of the degree of their agreement with corresponding analyses, may not have direct relevance to the practical problem under consideration. But the object of this investigation was the understanding of the evolution of the wake under controlled laboratory conditions rather than to provide a design tool. It is

13

hoped that an investigation of this type will reveal the underlying physics of the phenomenon (particularly that of the parachute collapse), help to interpret the full-scale results and will provide inspiration for the development of suitable numerical models with which the dynamics of axisymmetric, porous, and flexible parachute canopies can be investigated.

2 EXPERIMENTAL EQUIPMENT AND PROCEDURES

2.1 Vertical Water Tunnel

The experiments were conducted in a 17 ft (5.2 m) high, 2 ft by 2 ft (0.61 m x 0.61 m) cross-section vertical water tunnel (see Fig. 1). A quick-release valve located at the base of the tunnel is used to create an impulsively-started flow of desired velocity history. A partial drawing of the mushroom-like seating surface of the quick release valve is shown in Fig. 2.

In order to prevent distortion of the force measurements, the water side profile of the mushroom valve has been especially designed to ensure continuous undisturbed flow past the seat while the valve is in open position. As shown in Fig. 2, when the valve is closed, it is in the fully open position. It seats against an 'O' ring inserted on the bottom of the seating surface so that no leakage is present prior to initiating fluid motion.
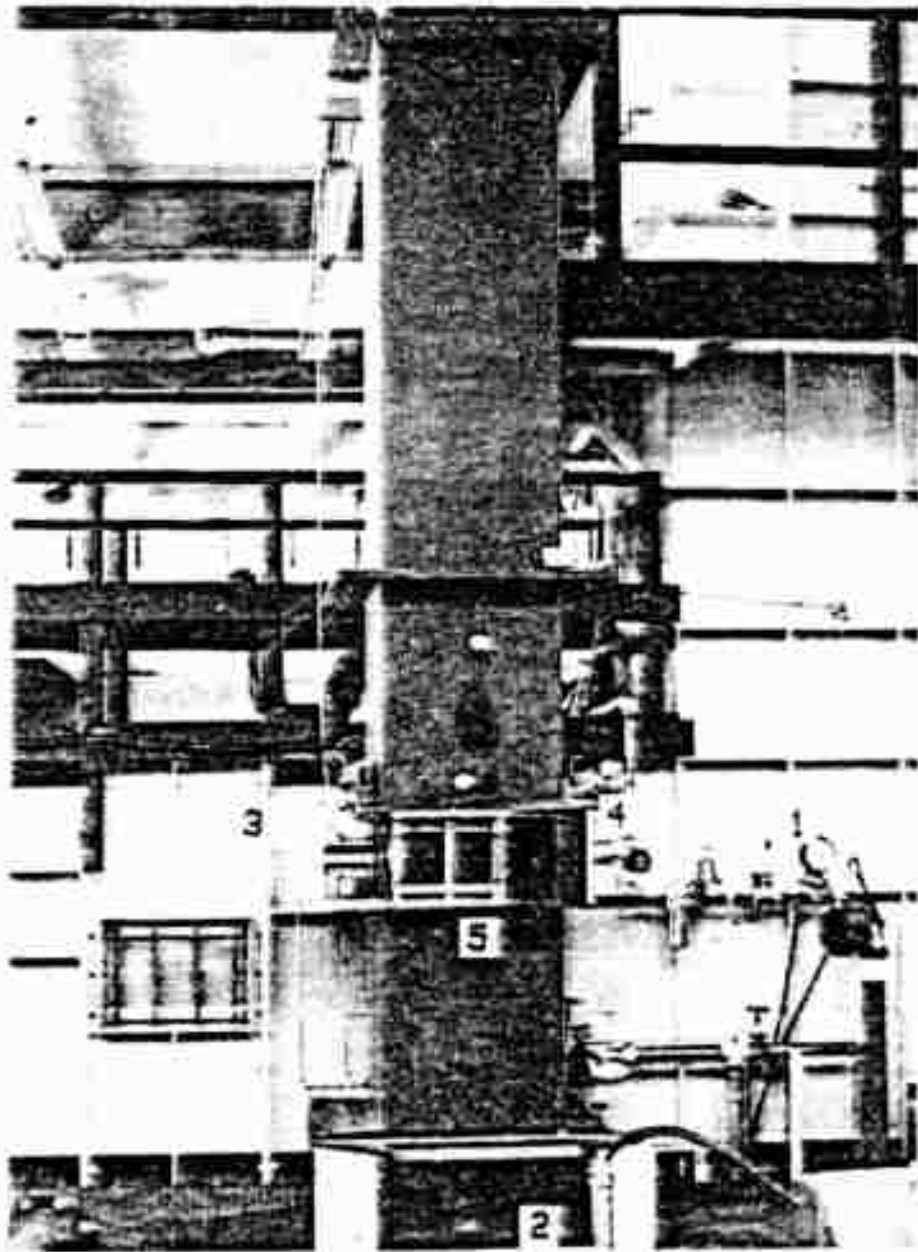
(1) Two-Way Air Supply Valve; (2) Quick-Release Valve
(3) and (4) Force Gages; (5) Light and Shadow Box

Fig. 1   Vertical Water Tunnel
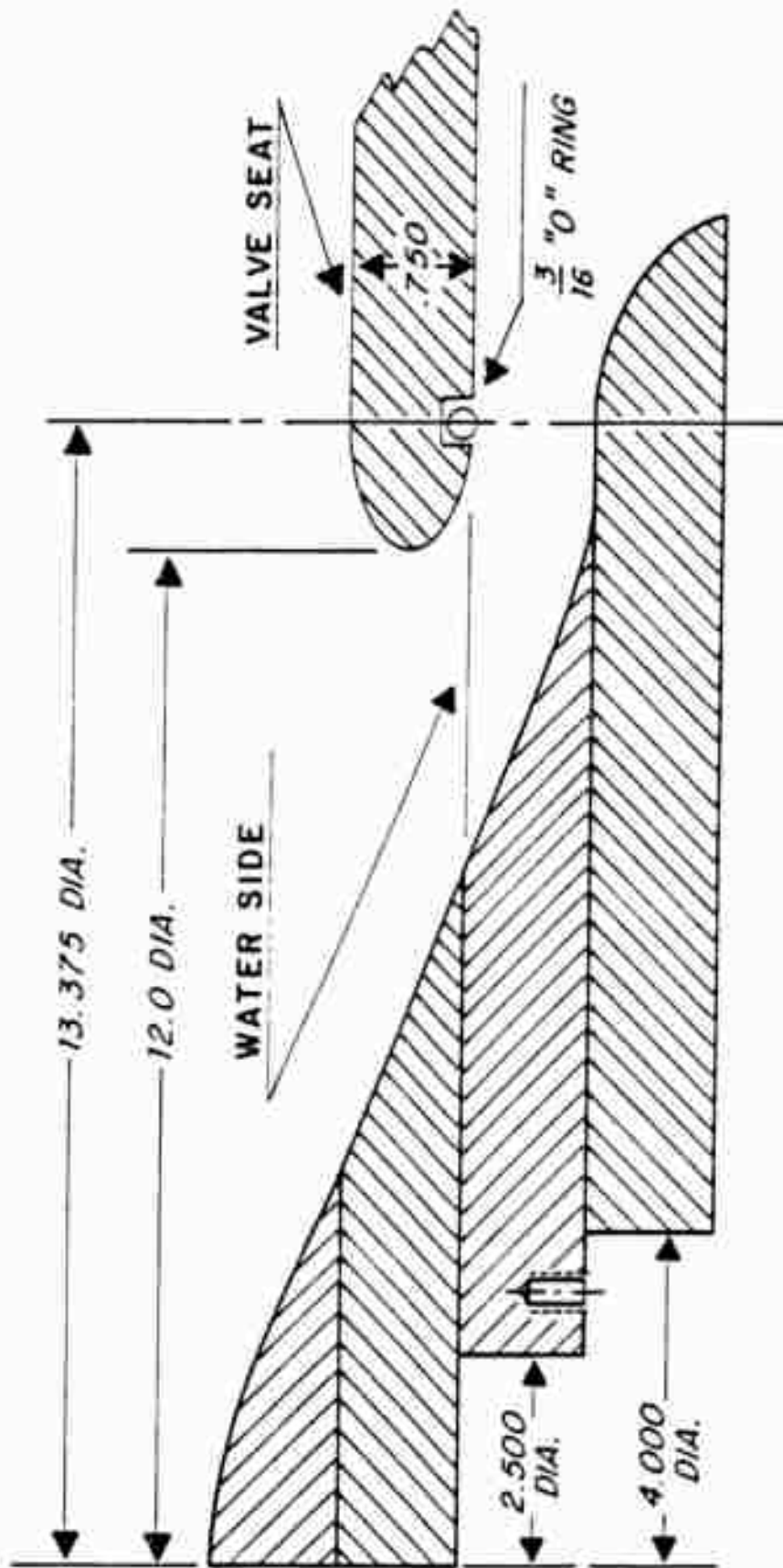
Fig. 2   Mushroom Valve Cross-Section (Not to Scale)

16

The vertical position of the mushroom valve is controlled by a three-way valve mounted beneath the tunnel (Fig. 3). The stem extends downward from the mushroom valve and is directly coupled to the control valve piston assembly. Compressed air is provided to the two air chambers in the upper part of the valve. Two computer-controlled two-way valves in the air supply line control the motion of the mushroom-shaped valve and, therefore, the flow itself.

Upon opening the air supply valves, the differential pressure between the two air chambers in the upper part of the control valve initiates motion of the piston, rapidly opening the mushroom valve. Thus, the flow is initiated and the fluid drains out into a reservoir beneath the tunnel. Subsequent valve motion is regulated by the vertical motion of the piston in the lower part of the control valve, the viscosity of oil in the liquid chamber, and the differential pressure between the two chambers. The area of the opening (and consequently the amount of resistance which the piston encounters) between the liquid chamber and the upper air chamber can be varied by opening or closing the dual ports in the piston (Fig. 4). Oil viscosity and supply air pressure can also be adjusted.

These adjustments allow constant velocities at desired rates (maximum 2 ft/s) to be obtained. Following
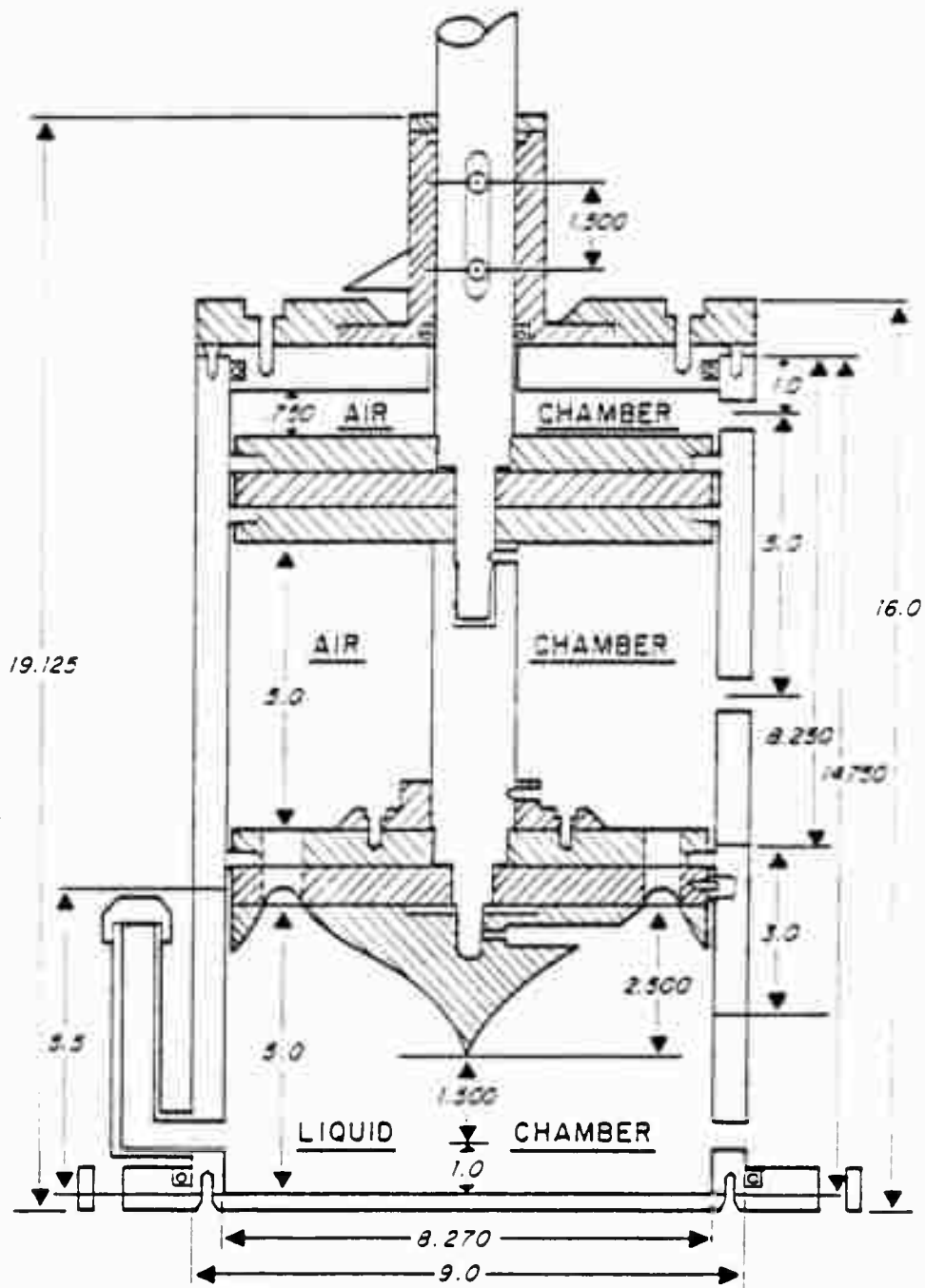
Fig. 3   Three-Way Valve Cross-Section (Not to Scale)

18
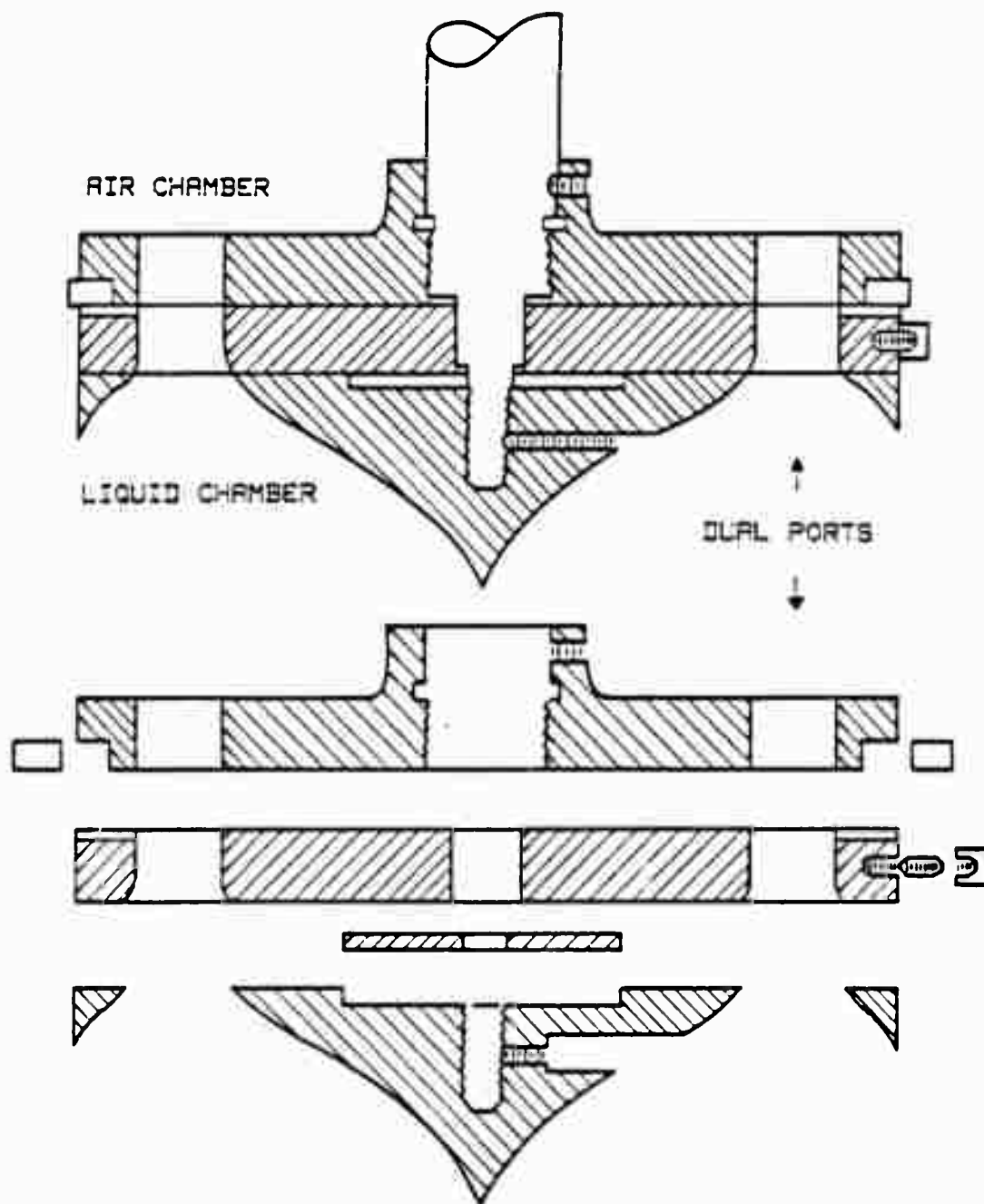
Fig. 4   Three-Way Valve Piston Cross-Section (Not to scale)

the rapid initial opening, which accelerates the flow in about 0.1 seconds, the mushroom-shaped valve may be either closed at a desired rate through the use of the computer-controlled air valves, so as to achieve a desired rate of flow deceleration, or maintained steady so as to achieve a continuous steady flow.

2.2   Test Bodies

Three circular arcs of radius 1.5 in. (3.80 cm), length 24.5 in. (62.2 cm), and included angles of 120 deg. (Model A), 180 deg. (Model B), and 240 deg. (Model C) were used in the experiments (see Fig. 5). The edges of the cambered plates were first cut razor sharp and then gently rounded with sand paper.

Each end of a model was terminated with a 0.25 in. (6.4 mm) long, 3 in. (7.62 cm) diameter circular section (part of the original pipe from which the model was cut out).   These end sections served several purposes. First, they prevented the distortion of the cambered plates during their manufacture. Second, they provided a clear view of the flow for visualization and photography when imbedded rigidly in a plexiglass window (however, and unavoidably, this circle shows in the pictures). Third, they enabled the measurement of the drag force when fitted with circular metal discs (aluminum mounts). In this case, the end sections were placed in special

Model A
120 degree arc
Radius = 1.5 in.

Model B
180 degree arc
Radius = 1.5 in.

Model C
240 degree arc
Radius = 1.5 in.
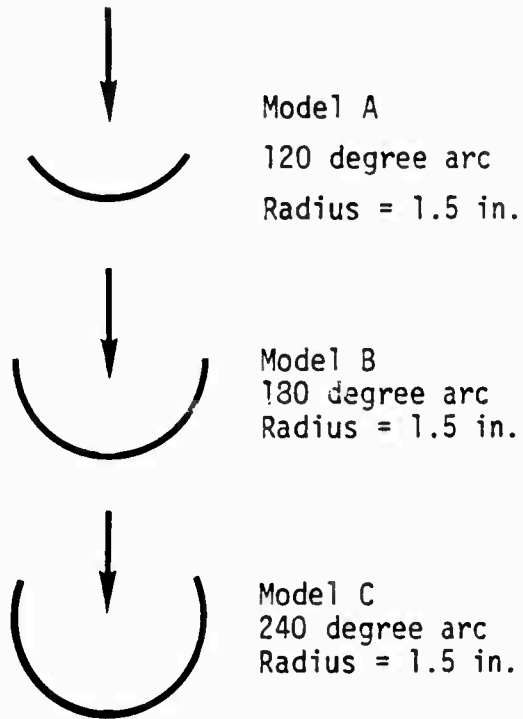
Fig. 5   Cambered Plate Models

housings cut out of the plexiglass window. The length and the diameter of the housing were such that there was a gap of approximately 0.04 in. (1 mm) between the housing and the end section. Each metal disc was attached to a circular rod which, in turn, was attached to the self-aligning bearing of the force transducer (see Fig. 6). The flow side of the metal discs were flush with the tunnel walls, i.e., there was no obstruction to the flow before it reached the cambered test plate. These will be described in more detail later.

2.3 Velocity, Acceleration, and Force Measurements

Velocity was determined both from the derivative of the elevation-time record and from the integration of the instantaneous acceleration. A ten foot long platinum wire, placed vertically in the tunnel and mounted away from the walls, provides water level indication to a data acquisition system (amplifiers, analog/digital data converter, computer, and recorder assembly). Prior to conducting any experiments, impulsive flow was initiated several times to check the operation of the system. Adjustments to the quick release valve control system were made, as necessary, to ensure the repeatability of the desired variation in velocity.

Acceleration of the falling liquid column was measured by means of a differential pressure transducer.

22
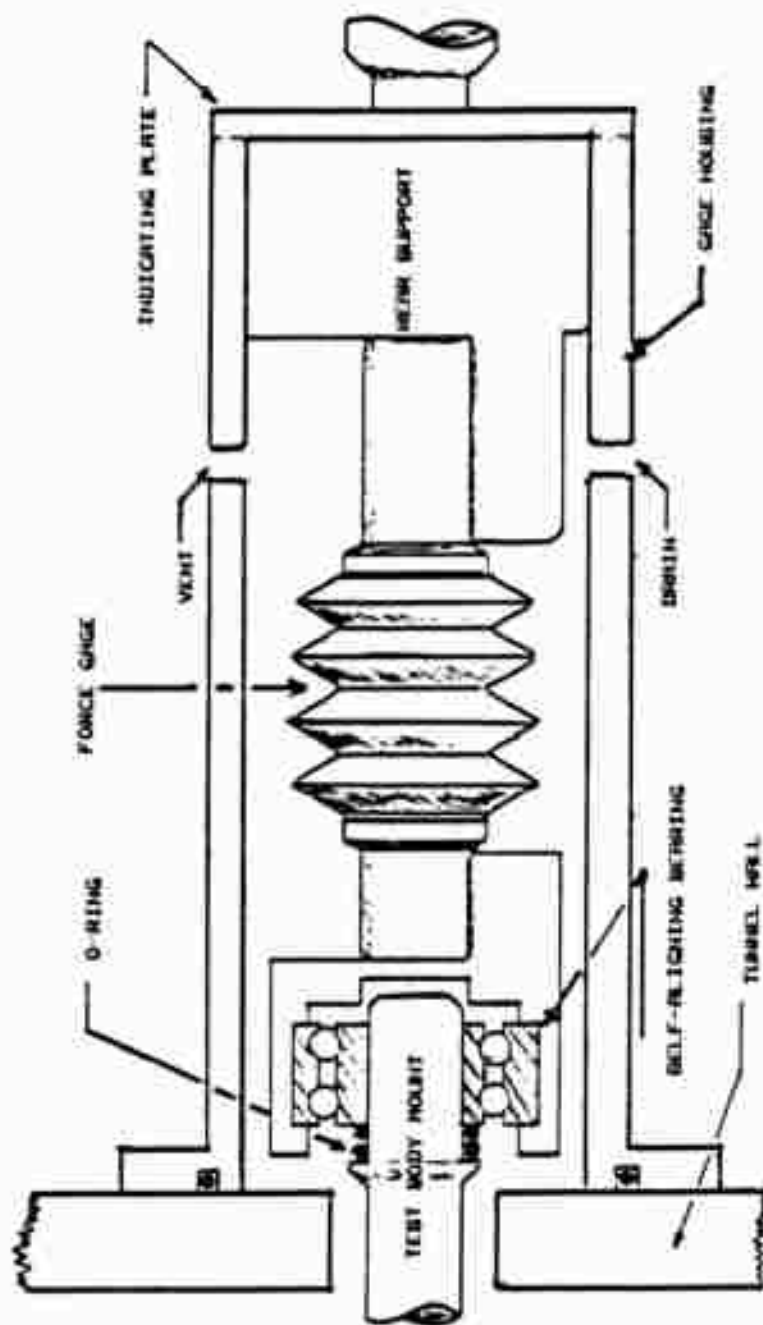
Fig. 6   Force Transducer (Not to Scale)

23

Two pressure taps, placed on the tunnel wall two feet (0.61 m) apart and vertically above each other, were connected to the pressure transducer. The acceleration was then directly calculated from $dU/dt = \Delta p/(2\rho\ell)$ where Δp is the differential pressure and ρ is the density of water. The hydrostatic part of the differential pressure was nulled out during the balancing of the carrier amplifiers. The instantaneous velocity was then calculated through the numerical integration of the instantaneous acceleration. The velocities obtained from the two methods noted above agreed with each other within 3 percent.

Two shear-force gages of 10 kg capacity (with an over-load capacity of 100 percent) were used to measure the instantaneous drag force acting on the test bodies (see Fig. 6). Special housings were built for each gage so that they could be mounted on the tunnel wall at each end of the test body. The bellows protecting the strain gages were filled with Dow Corning RTV coating for water proofing and then the ends of the bellows were sealed air tight. These gages as well as the platinum wire and the differential pressure transducer were recalibrated at the start and at the end of each test day. No change was ever encountered during the entire series of tests.

One end of each test body was mounted in a self-aligning bearing (see Fig. 6) whose housing was connected

to the force transducer. This allowed the test body to be freely mounted and accurately aligned. The other end of the test body was connected to the other force gage with a male-female coupling and a pin which allowed rotation only in the vertical plane. The angular position of the coupling was adjusted so as to make the sharp edges of the model align in a horizontal plane in both the x- and y-directions.

Prior to and at the end of each test day, calibration of the force gages was conducted in both air and water. Known loads of up to 10 kg were placed at the mid-length of each body. Note that the shear-force gages do not require that the load be placed **exactly** in the middle of the body. The amplifier-recorder attenuation settings were adjusted and compared for each different load to ensure linearity, consistency, and repeatability. Following the completion of the load calibrations in air, the tunnel was filled with water to its full operational height and the calibrations were repeated in order to make sure that the slight expansion of the tunnel and the hydrostatic loading of the force gages did not affect the calibration. A simple remote control arm was used to place or remove the loads from the model. The net weight as well as the buoyant force acting on each load were known prior to the calibrations. As will be noted later, the same remote arm was used to pour dye in the model for purposes of flow visualization.

25

Figures 7 through 9 show sample traces of elevation, acceleration and force for the Models A, B, and C, respectively. The polarity of the force traces in Figs. 8 and 9 has been reversed relative to that of Fig. 7. The small oscillations in the elevation, acceleration and force traces are due to the fact that the data have not been filtered.

Following the initial rise in acceleration due to the impulsive start of the motion, the fluid reaches a constant velocity and then decelerates rapidly. The duration of the period of constant velocity and the shape and magnitude of the deceleration are dictated by the initial setting of the control valves.

A typical test run lasted about 2 seconds. Each model was tested approximately hundred times for various durations of the initial steady flow and magnitudes and shapes of the subsequent deceleration. At least three runs were conducted at each velocity and deceleration setting. Thus, three hundred elevation, acceleration, and force traces, similar to those shown in Figs. 7 through 9, were obtained for each model.

2.4 Flow Visualization

The fluid motion was visualized with dye and beads and recorded on video tapes. A plane of light across the camber was provided through slits approximately one foot

ELEVATION

ACCELERATION

FORCE

TIME (50 mm = 1 s)
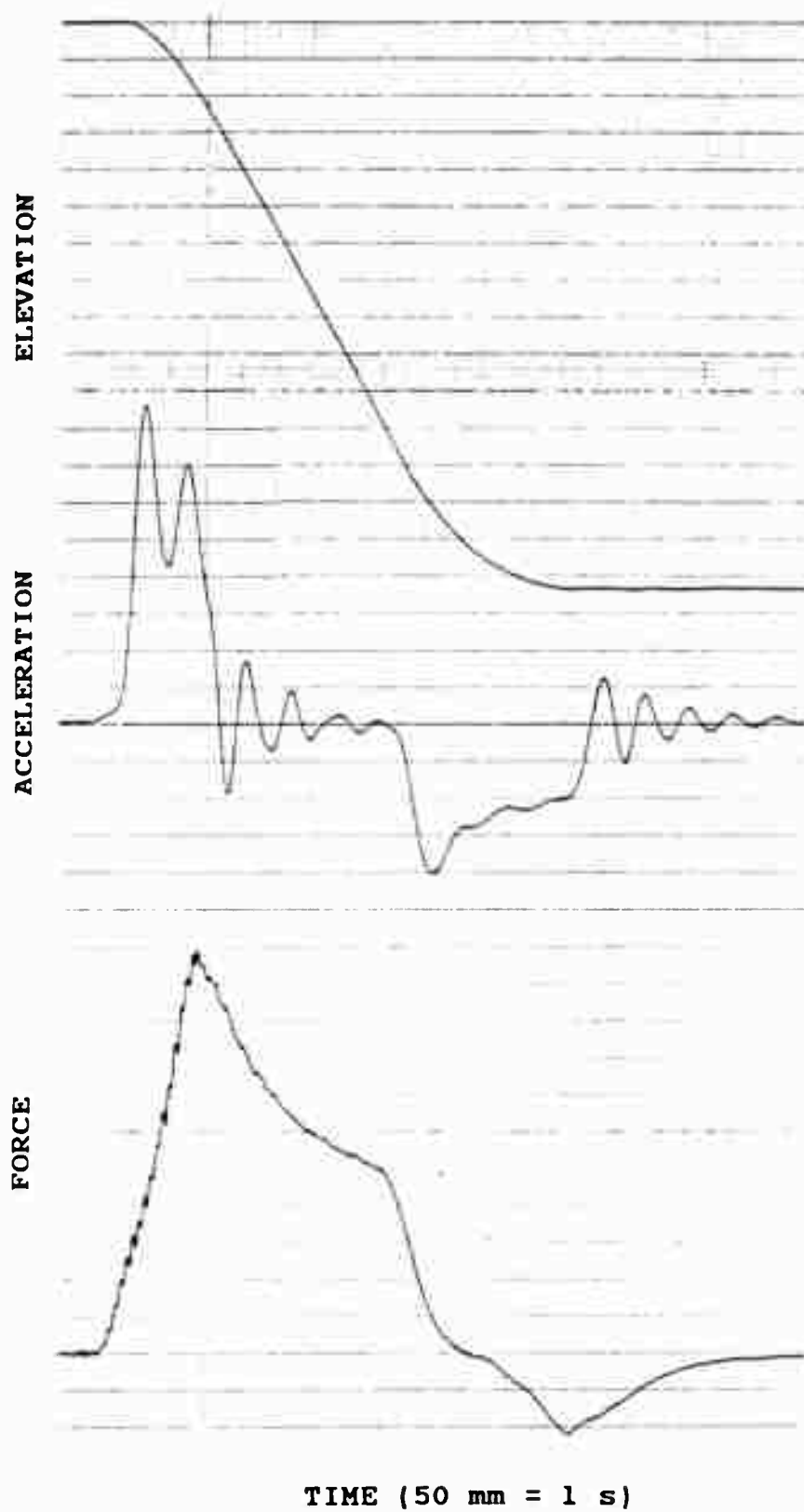
Fig. 7   Sample Elevation, Acceleration,
          and Force Traces for Model A

27
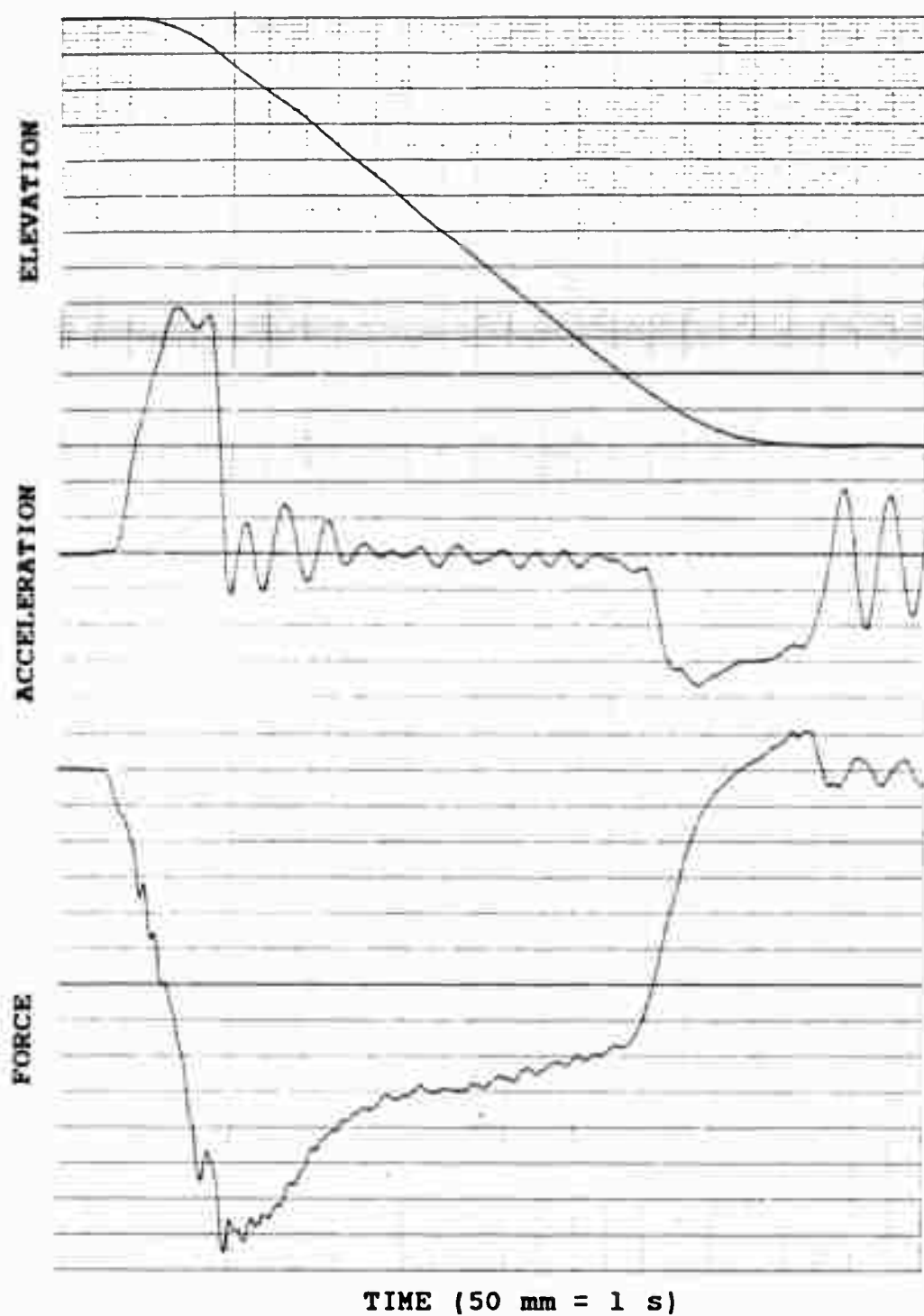
Fig. 8   Sample Elevation, Acceleration,
          and Force Traces for Model B

TIME (50 mm = 1 s)
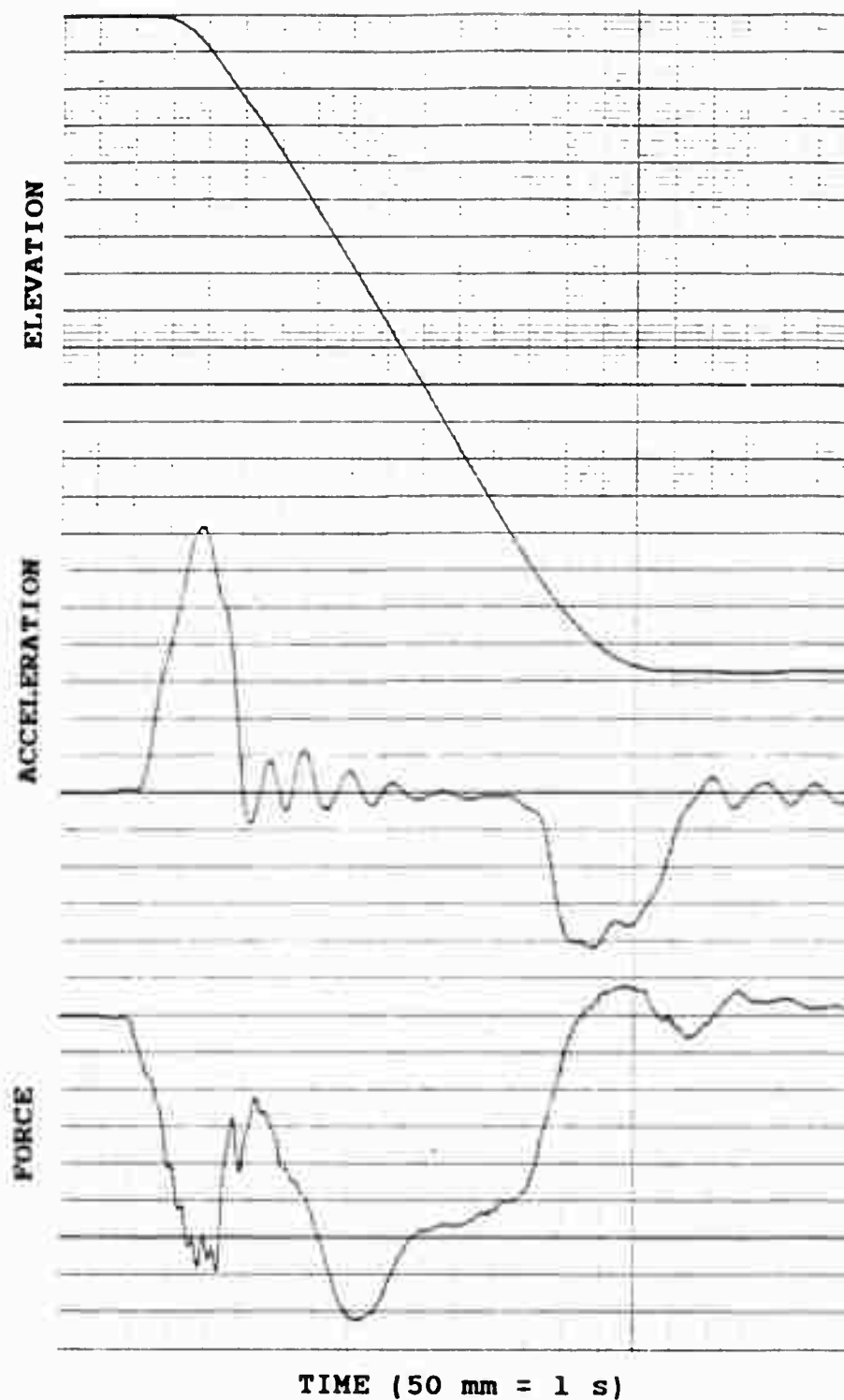
Fig. 9   Sample Elevation, Acceleration,
and Force Traces for Model C

29

long, cut into the front and rear walls of the tunnel. Shadow boxes were attached externally to the tunnel (see Fig. 1) into which were mounted high intensity lights.

In one series of tests, fluorescent dye was used for flow visualization. A small amount of salt was added to the dye to make it slightly heavier than water. After insuring that the water in the tunnel was calm, the dye mixture was poured slowly into the camber through the use of the remote control arm. The mixture stayed in the camber prior to the commencement of the experiment.

In another series of experiments, neutrally-buoyant, fluorescent, polystyrene beads were dropped into the filled tunnel from directly over the plane of light. After allowing the beads to slowly sink down to the level of the camber, while continuing to add more, the quick release valve was tripped to initiate the flow for the already running video system. Also recorded on the video tape was the time in seconds and 1/100 seconds. The timer was started few seconds prior to the inception of the flow. However, both the time differences between successive frames and the actual time from the inception of the motion can be determined easily from the pictures.

Figure 10 shows the evolution of flow about the Model A for a particular acceleration-deceleration history. Figures 11 and 12 show similar examples of the flow development for the Models B and C, respectively.
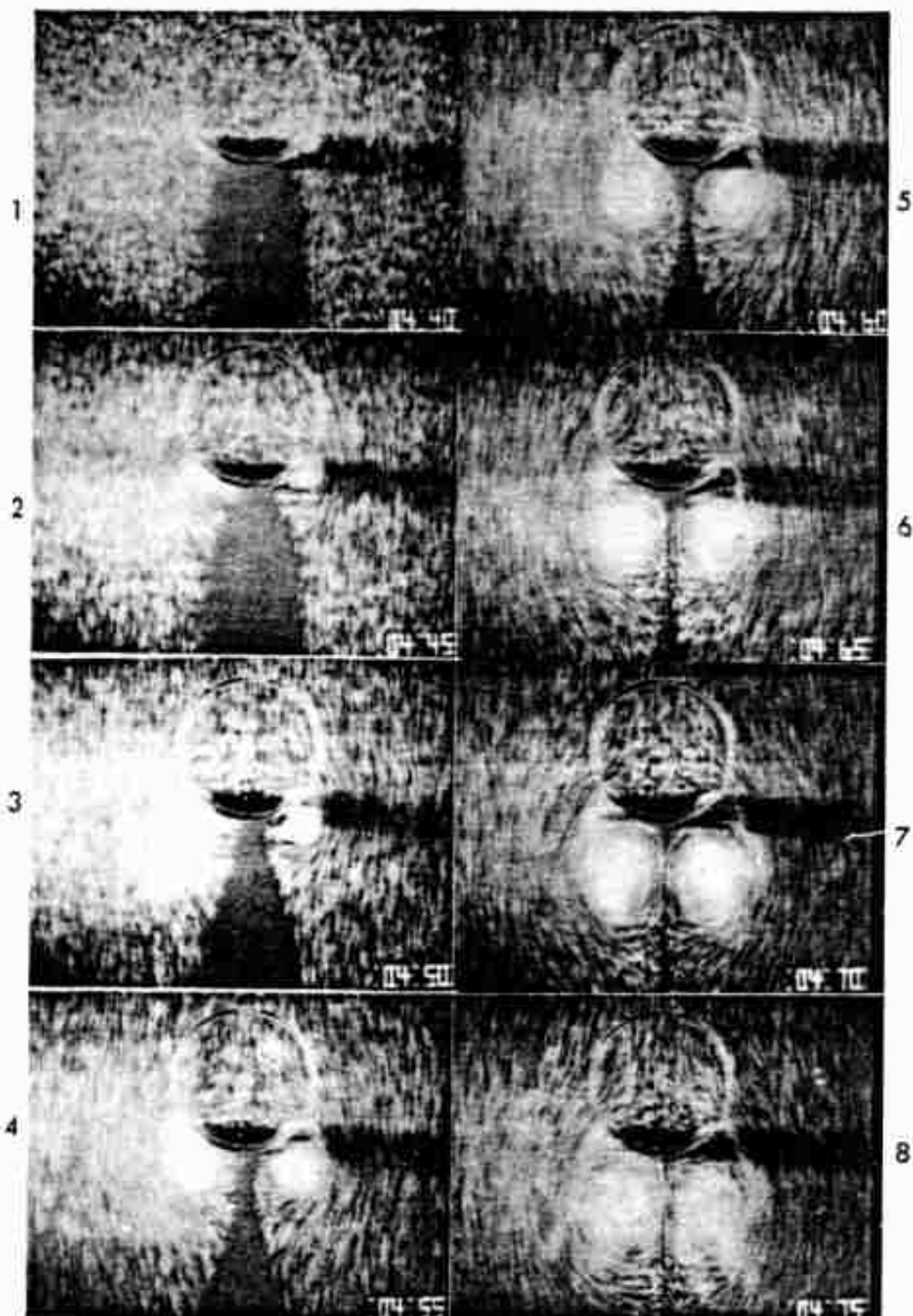
Fig. 10   Evolution of Flow about the Model A

31

Fig. 10 Evolution of Flow about the Model A (Continued)

32
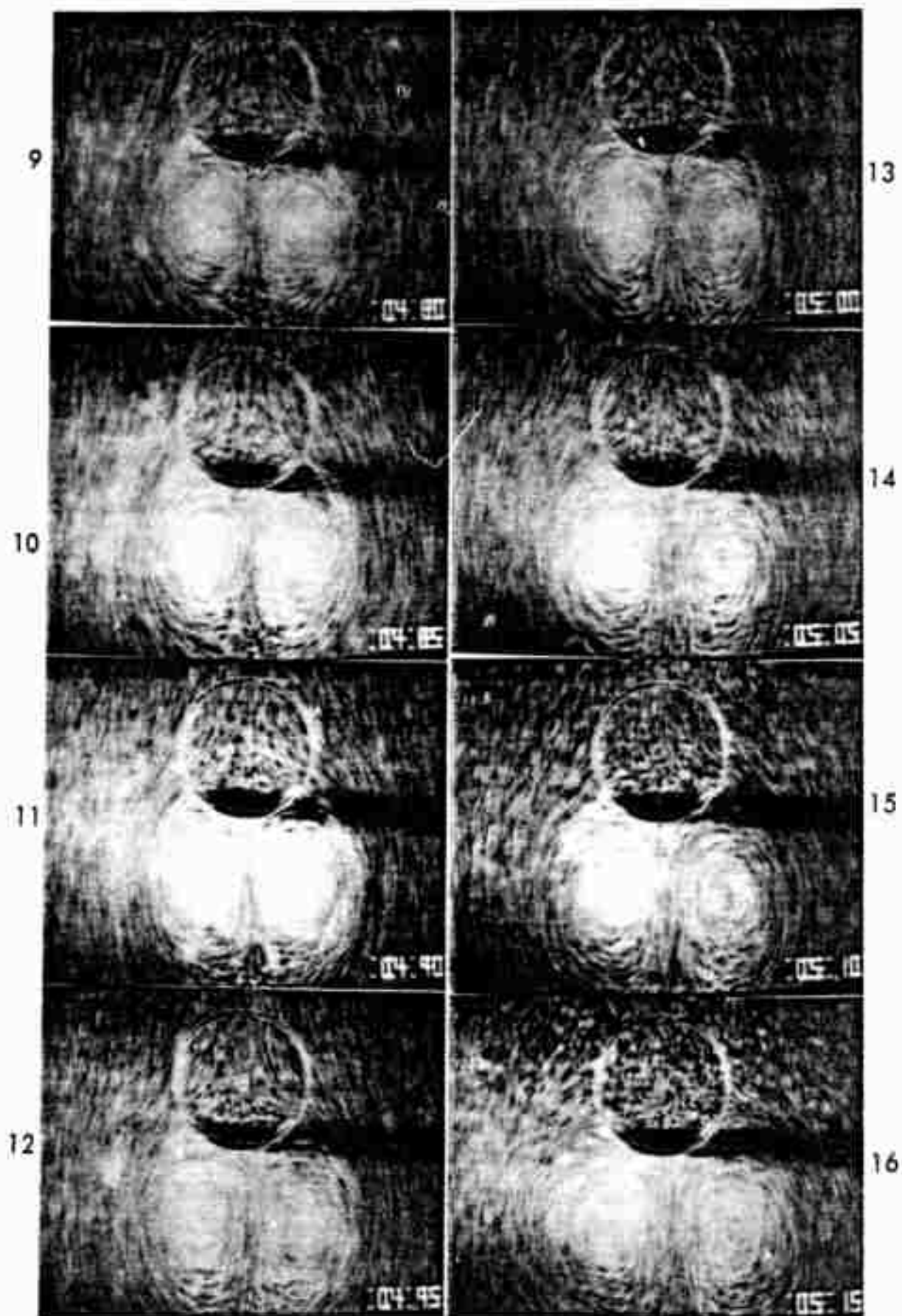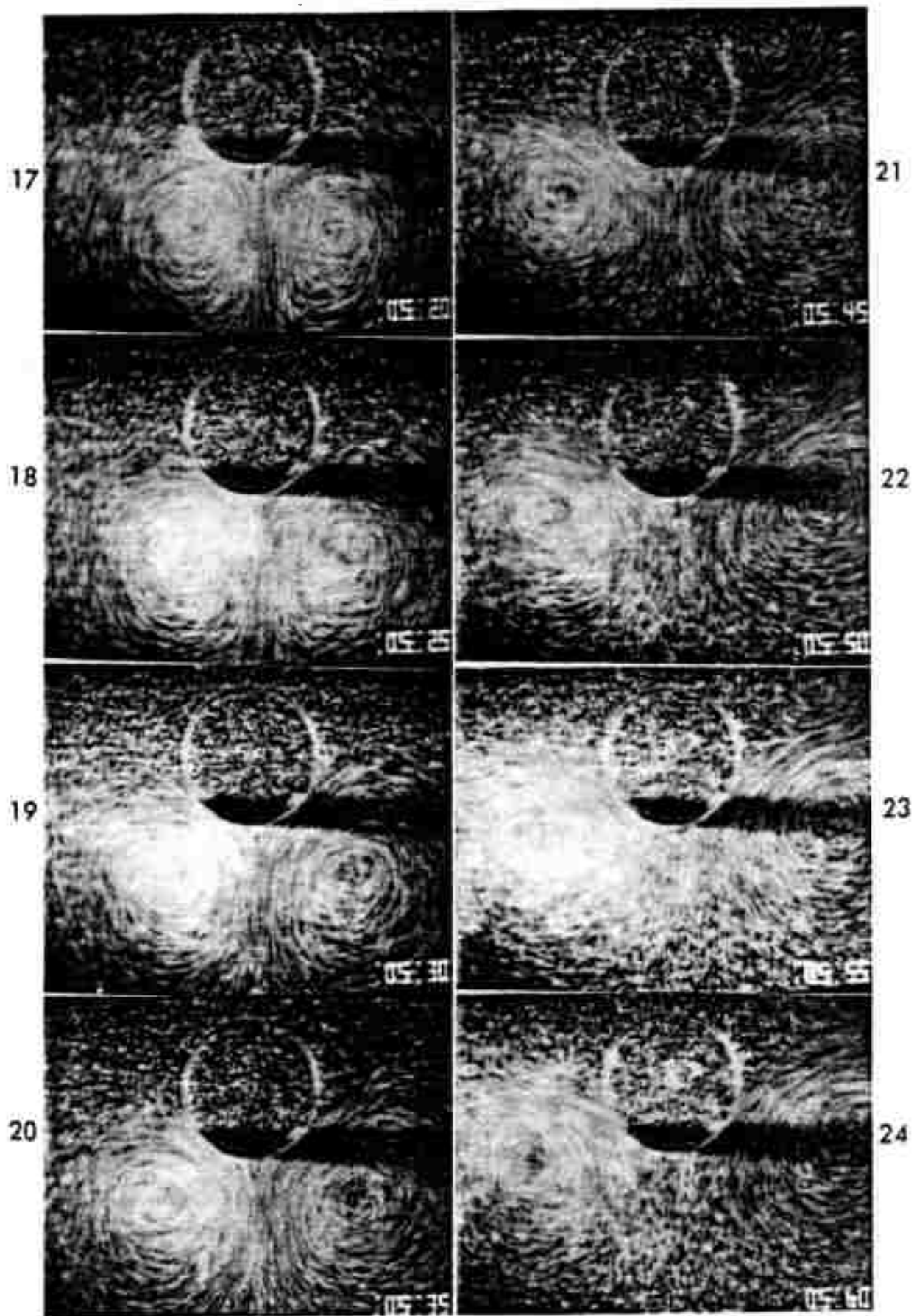
Fig. 10   Evolution of Flow about the Model A (Continued)

Fig. 10 Evolution of Flow about the Model A (Continued)
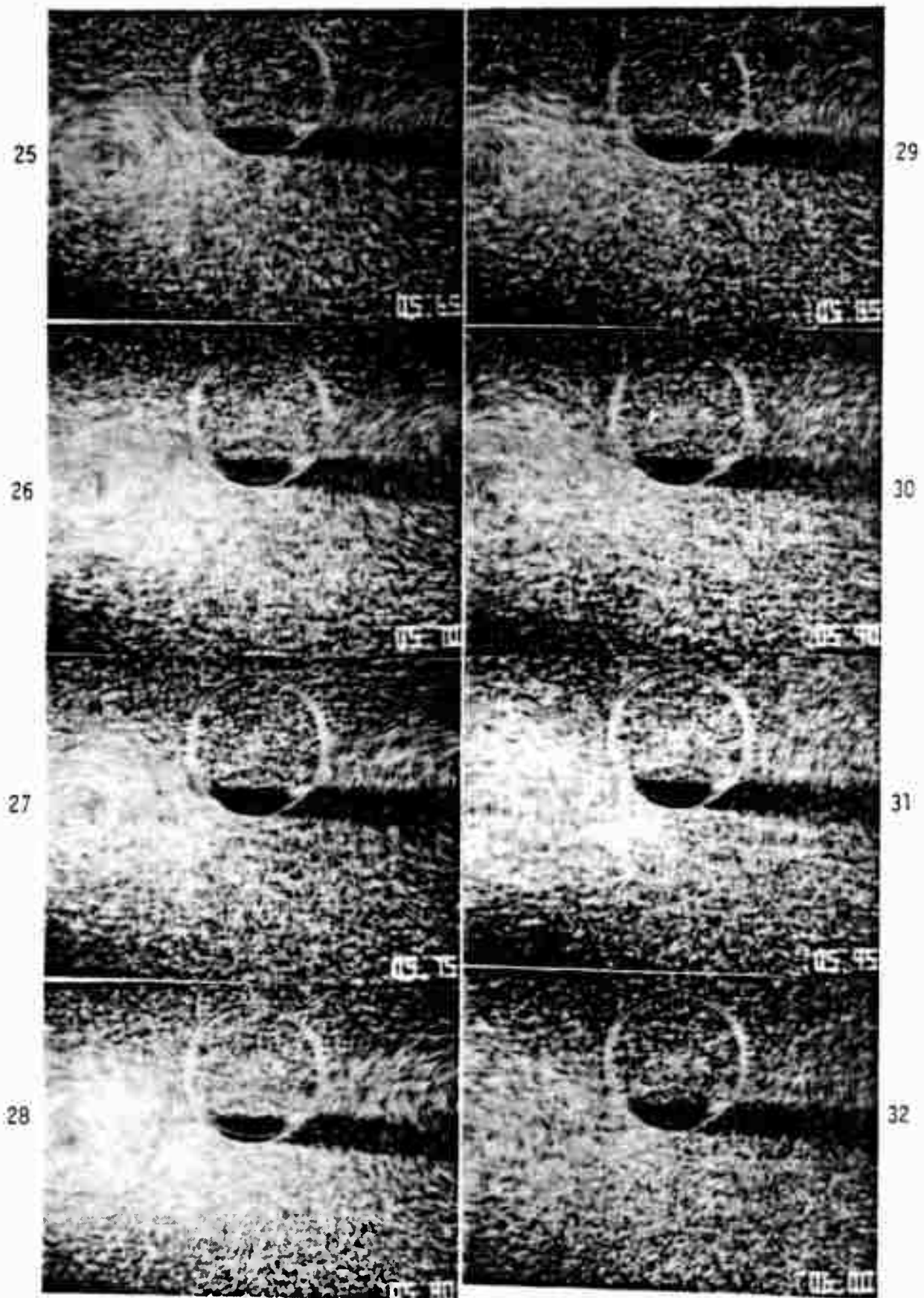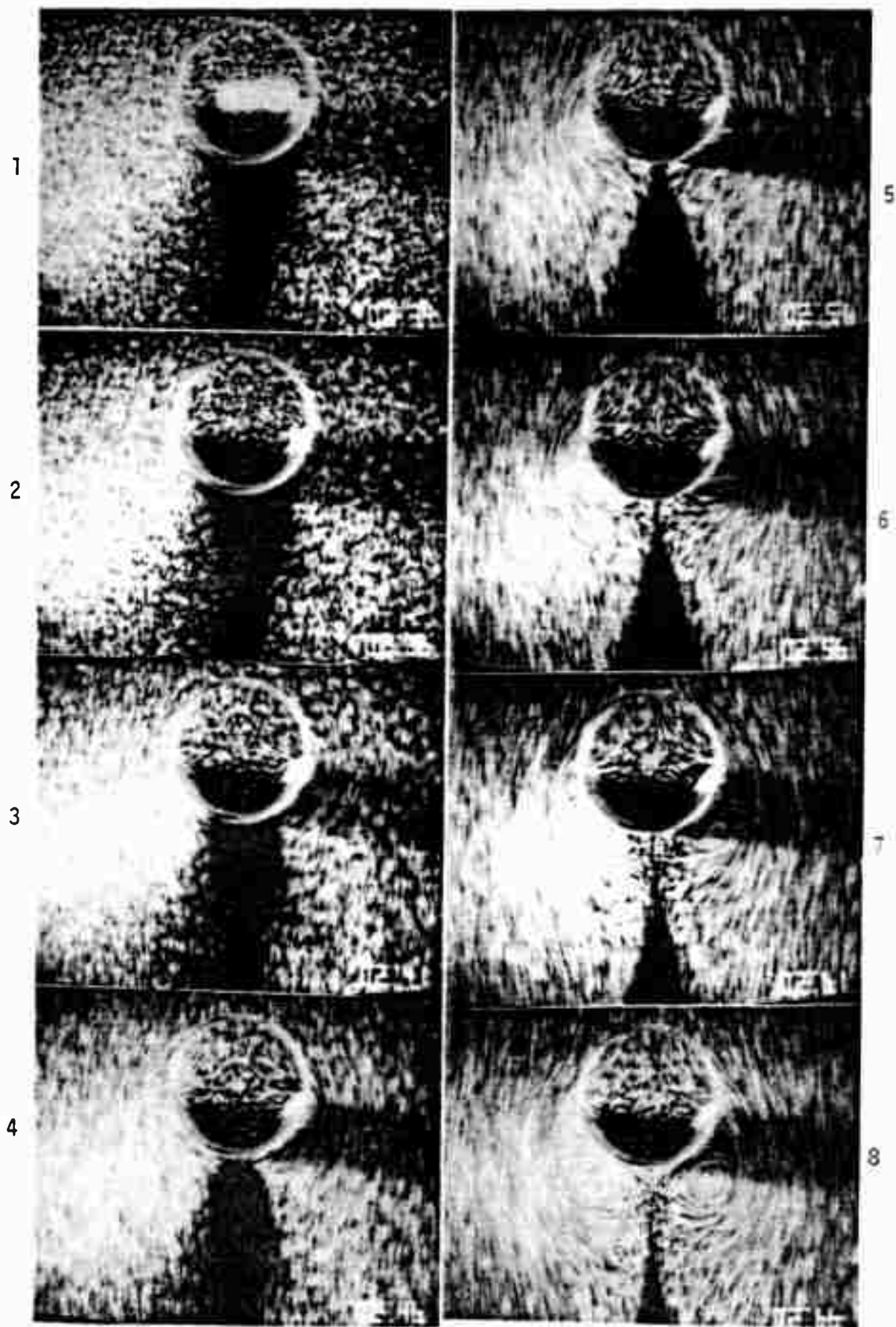
34

Fig. 11 Evolution of Flow about the Model B

35

Fig. 11 Evolution of Flow about the Model B (Continued)

36

Fig. 11 Evolution of Flow about the Model B (Continued)

37

Fig. 11 Evolution of Flow about the Model B (continued)

38
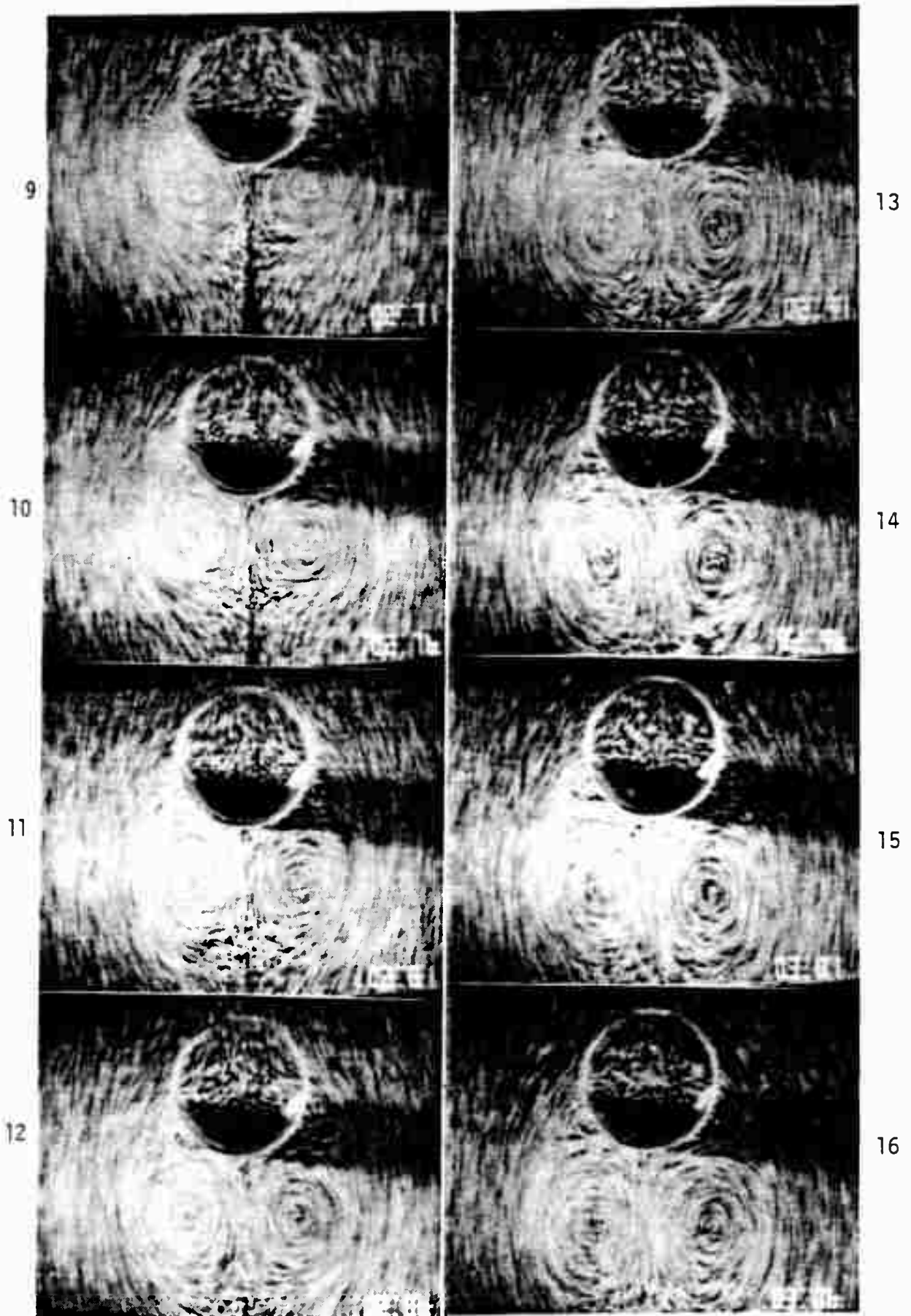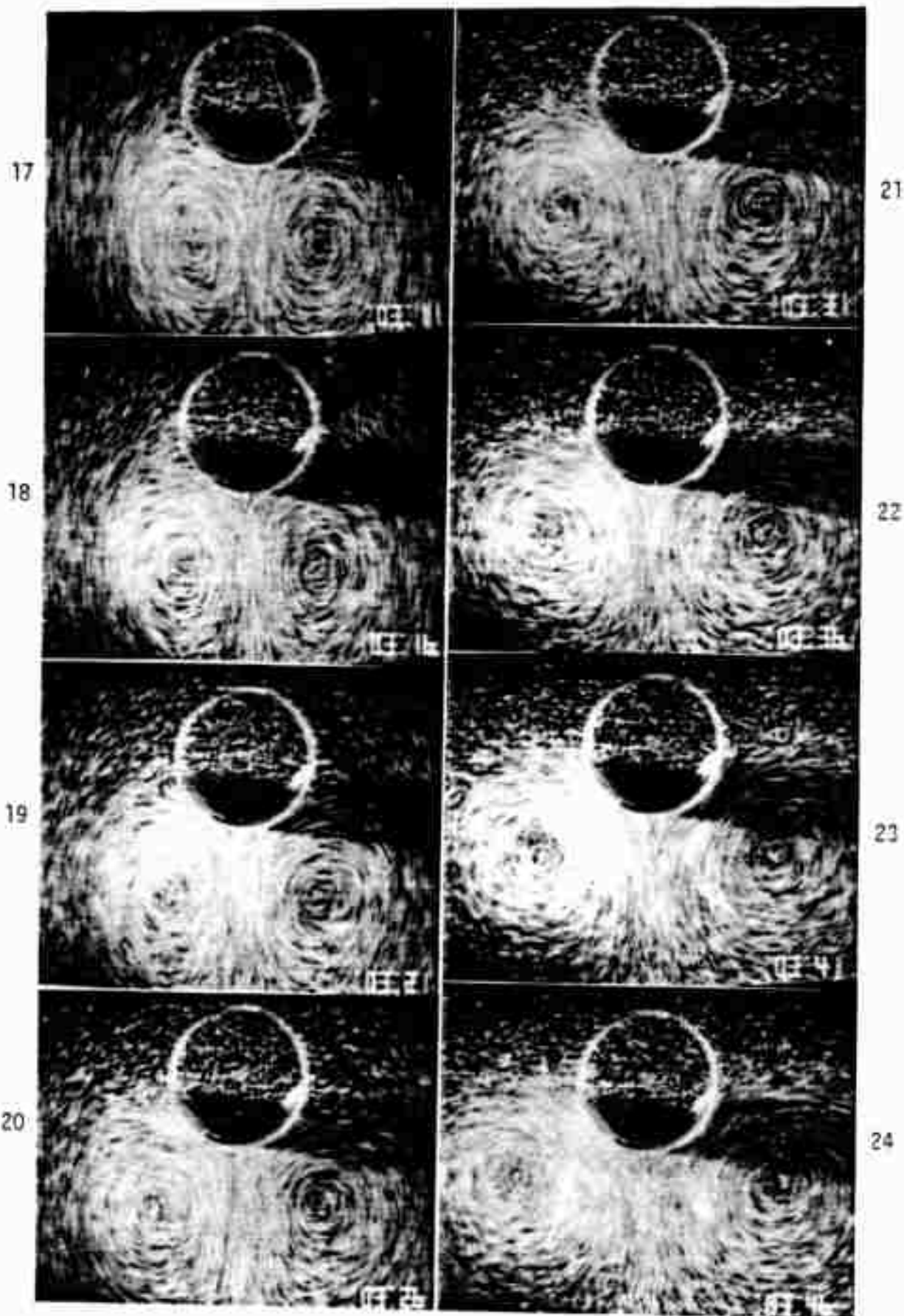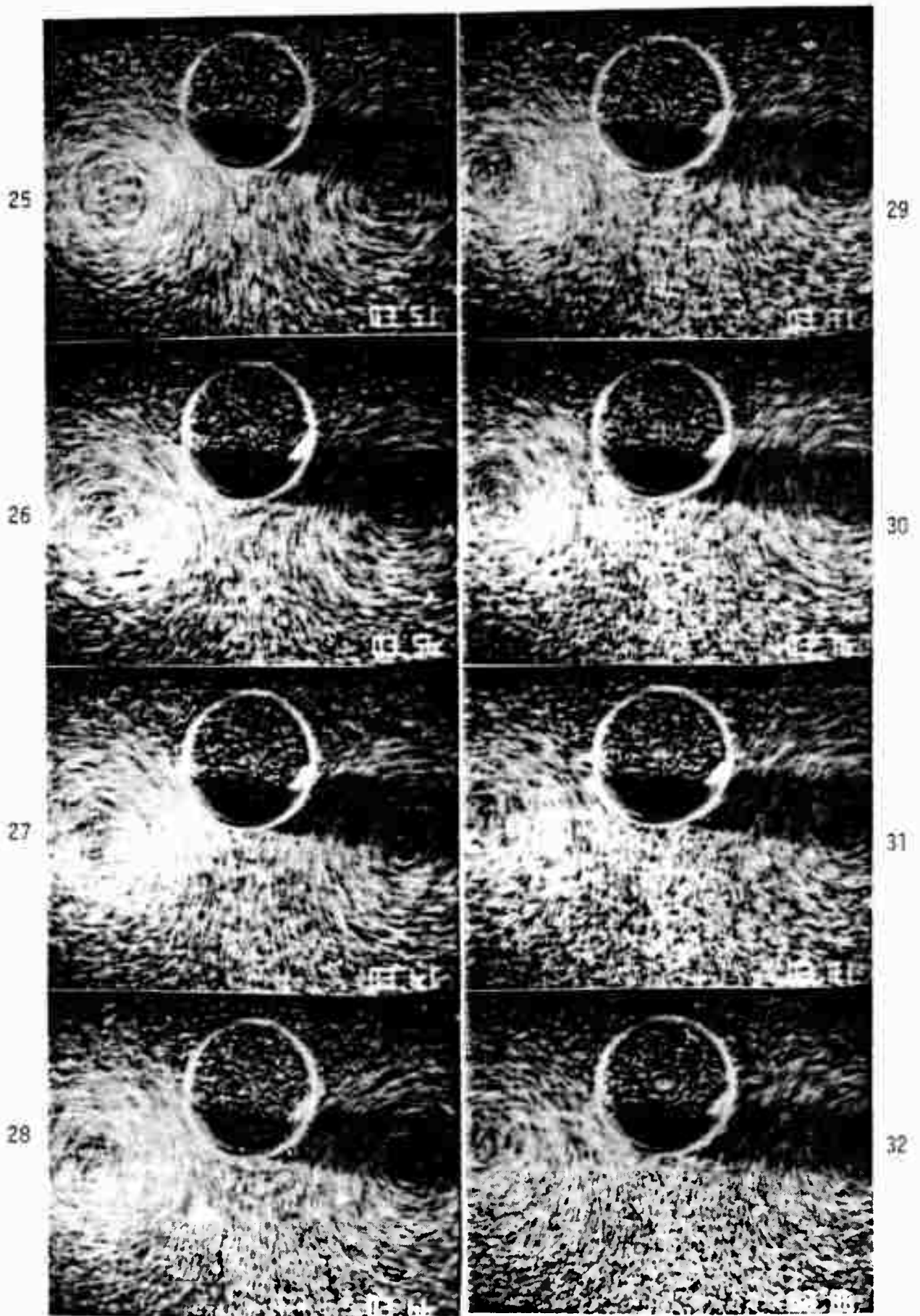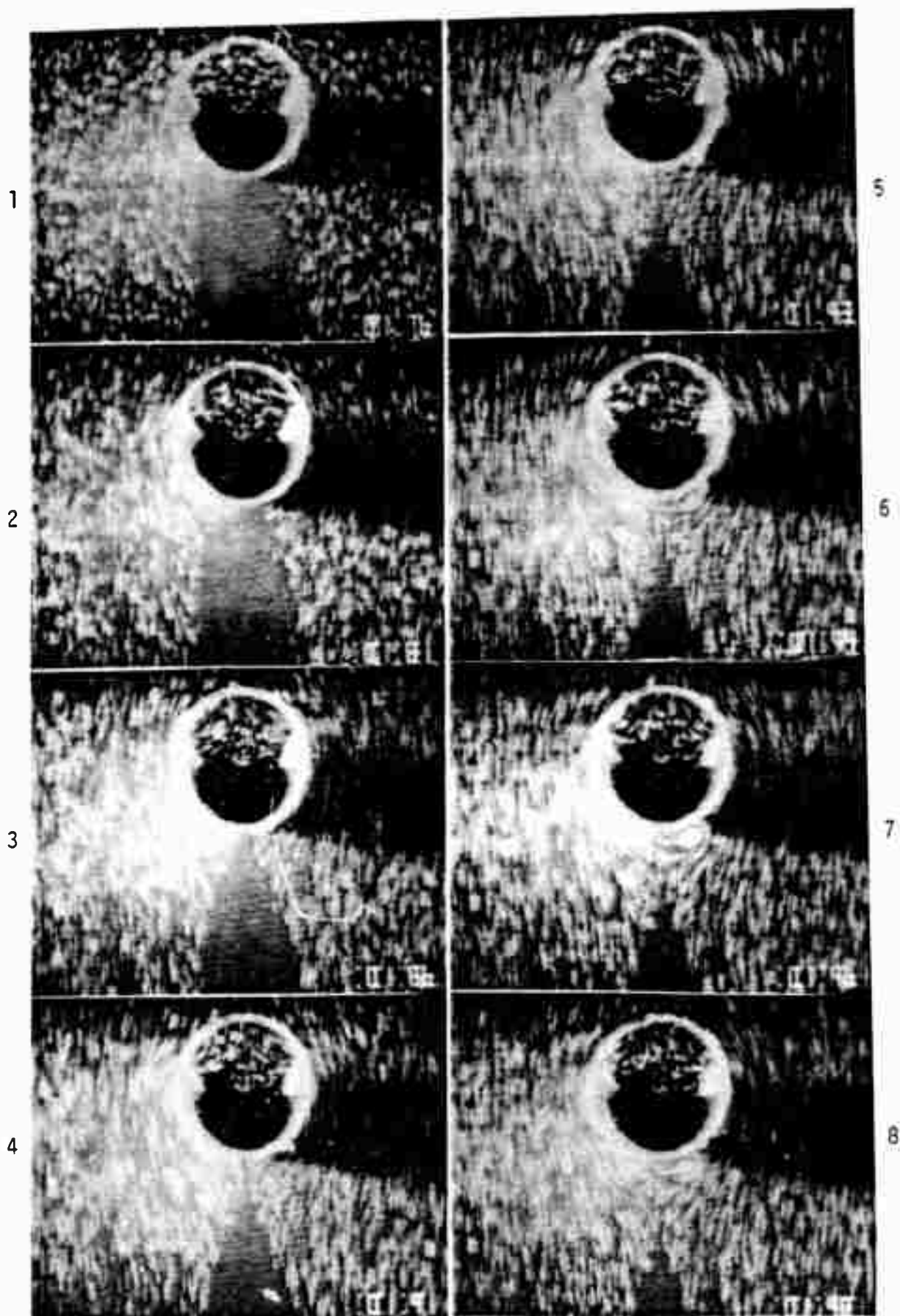
Fig. 12   Evolution of Flow about the Model C

Fig. 12 Evolution of Flow about the Model C (Continued)
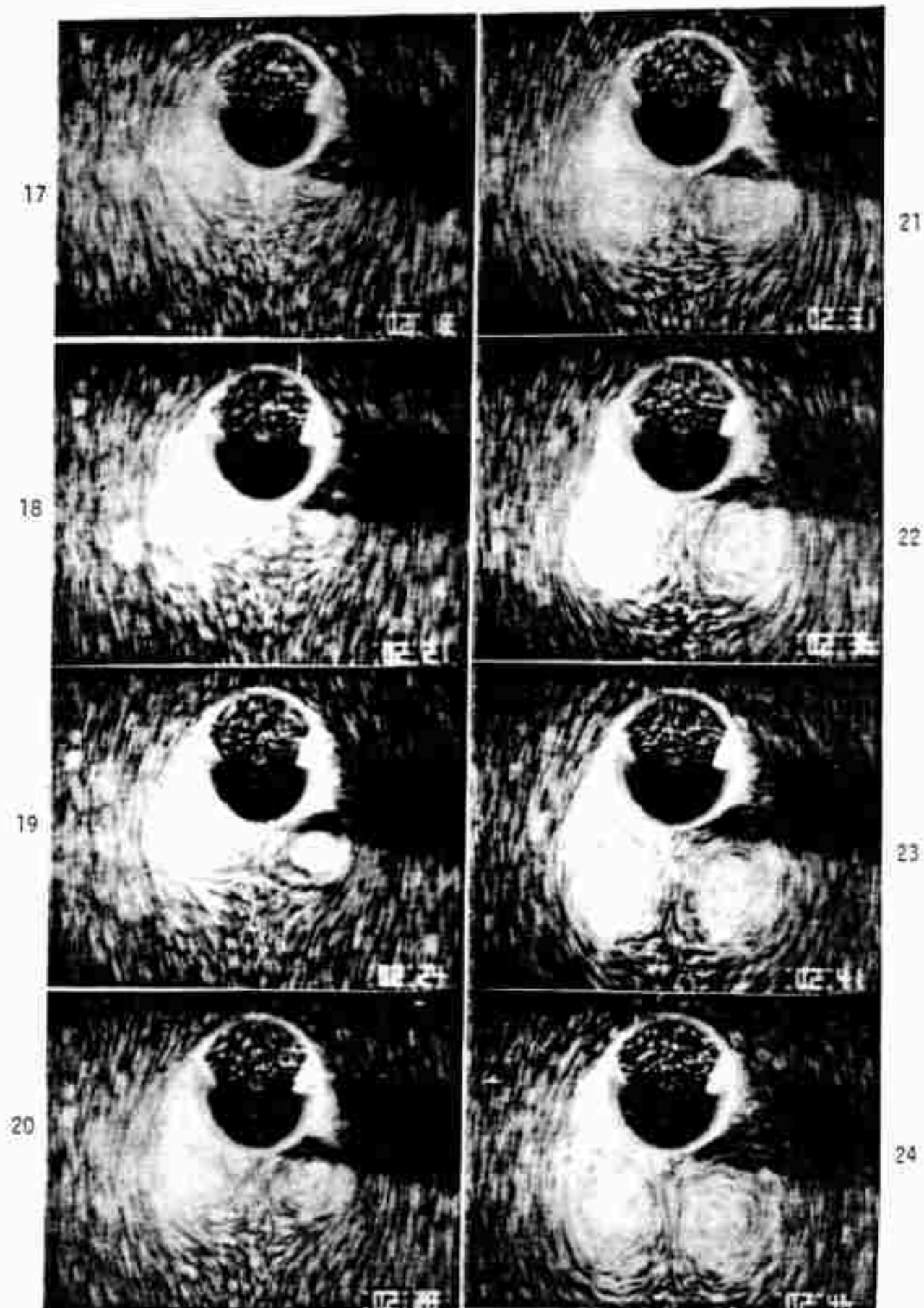
40

Fig. 12   Evolution of Flow about the Model C (Continued)

41

Fig. 12   Evolution of Flow about the Model C (continued)

42
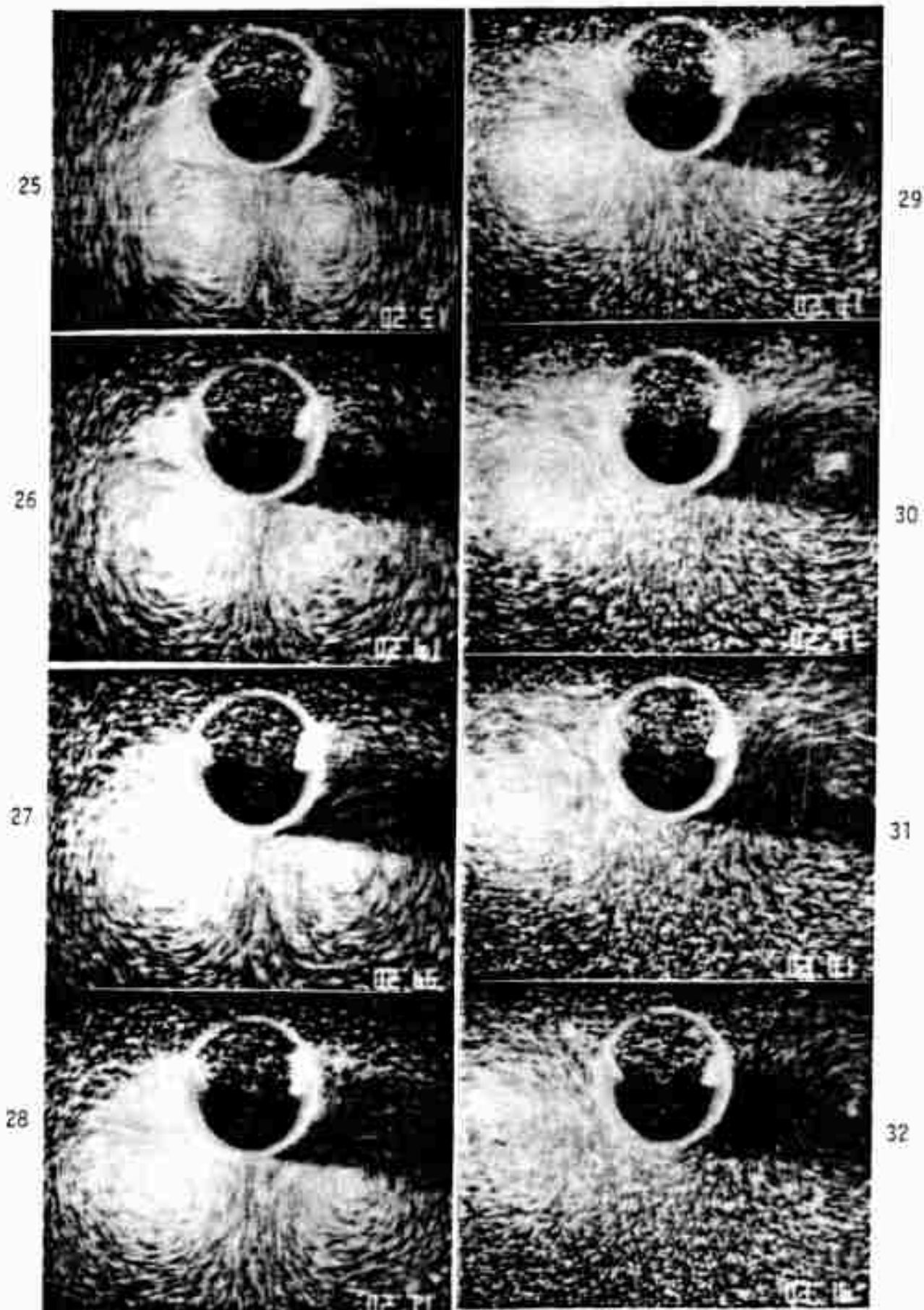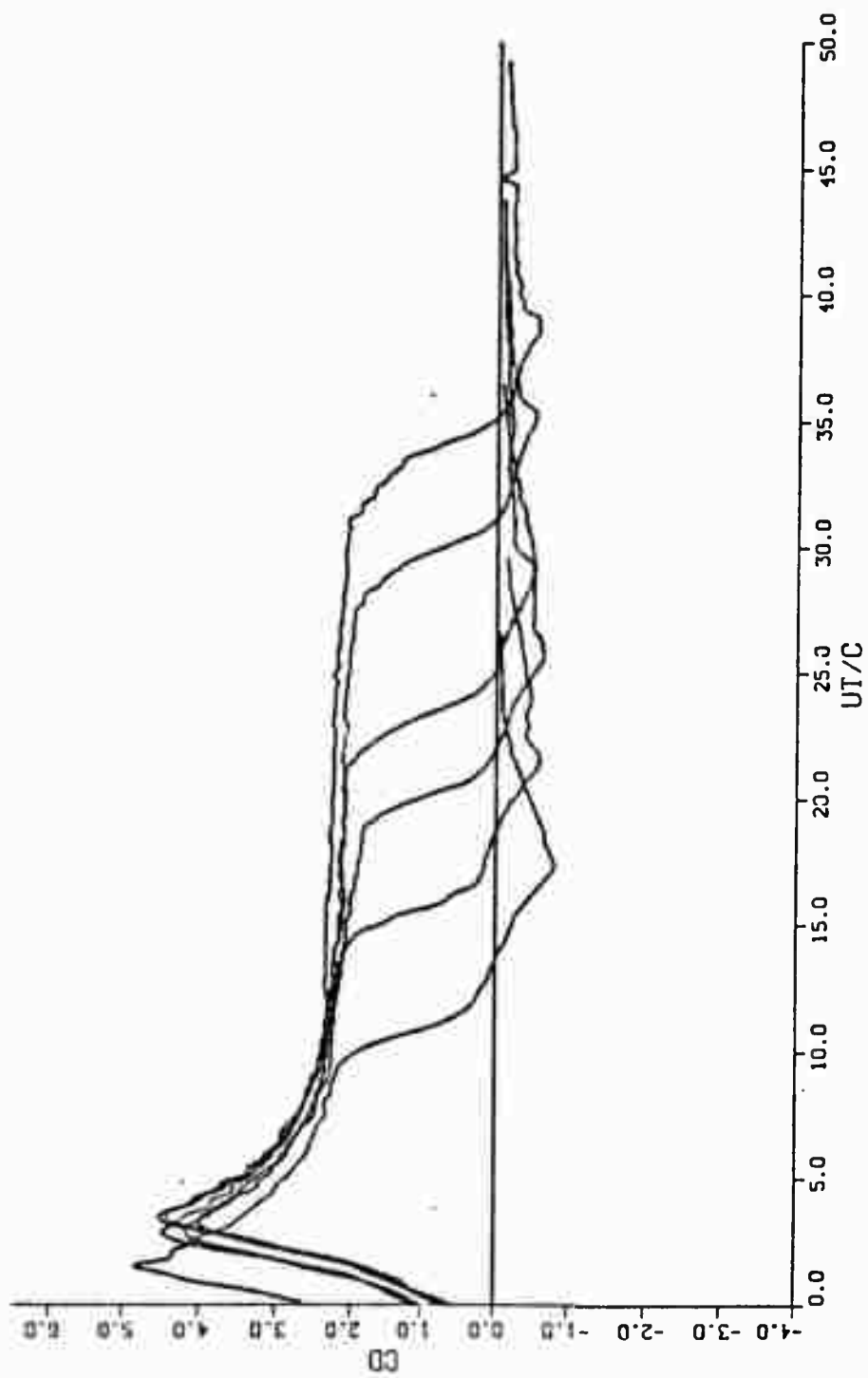
Fig. 13 Drag Coefficient versus T' for the Model A

The time shown in the lower right-hand corner of each frame is in seconds and 1/100 seconds. Time zero does not correspond to the inception of flow. In Figs. 10 through 12, the flow is started at times 4.40 (the first frame), 2.41 (the third frame), and 1.81 (second frame), respectively.

3 DISCUSSION OF EXPERIMENTAL RESULTS

The results will be discussed first in terms of the representative force data and then in terms of the evolution of the wake.

The drag coefficient is defined as

$$C_d = 2F/(\rho LWU_o^2)$$

where L and W represent, respectively, the length (2 ft or 0.61 m in this investigation) and the projected width of a model. U_o is the steady flow velocity prior to the onset of deceleration. Note that for the models A and B, the projected width is equal to the distance between the sharp edges of the model, i.e., W = 2.6 in. for the Model A and W = 3.0 in for the Model B. However, for the Model C, the projected width is still 3.0 in., i.e., the diameter of the generating circle. The drag coefficient is plotted as a function of the dimensionless time $T^* =$

44

$U_o t/c$ where t is the time and c is the radius of the camber, (c = 1.5 in. in the experiments).

3.1 Model A

Figure 13 shows a comparison of the drag coefficients for the Model A for various periods of the initial steady flow, prior to the onset of deceleration. These data are reduced from force-time records similar to those shown in Fig. 7. Several important facts may be deduced from a perusal of Figs. 7, 10 and 13.

The drag coefficients prior to the onset of deceleration are nearly identical. The drag coefficients after the onset of deceleration are simply shifted in time by an amount equal to the difference between the durations of their steady-states. In other words, the force acting on Model A is not materially affected by the duration of the ambient steady flow within the range of the parameters encountered in the present study (the Reynolds number defined as Re $= U_o W/\nu$ ranged from approximately 20,000 to 50,000).

Considering a particular run in Fig. 13, one observes that the drag coefficient rises rapidly to a value of about 4.5 (due to the rapid accumulation of vorticity in the growing vortices) and then begins to decrease as the vortices develop under the influence of a constant ambient velocity. Subsequently, C_d approaches a

45

constant value of about 2 (for runs with longer periods of steady ambient flow) prior to the onset of deceleration. For a flat plate normal to a steady flow, the drag coefficient is nearly equal to 2 and is independent of the Reynolds number. However, the similarity of the two drag coefficients cannot be taken too seriously. There are fundamental kinematical and dynamical differences in the wakes of the two flows.

The drag coefficient decreases rapidly at the onset of deceleration, goes through zero near the middle of the deceleration period, and through its minimum (negative) value at the end of the deceleration period (see Fig. 7). Subsequently, C_d gradually decreases to zero. The occurrence of a negative drag during the second half of the deceleration period is of fundamental importance and may be regarded as the cause of the inception of the collapse of a parachute. A deeper understanding of the relationship between these two phenomena, however, requires further detailed investigation.

Figure 10 shows a sample sequence of the pictures depicting the growth and motion of vortices behind the Model A (no attempt has been made to select the frames at equal time intervals). In these pictures, the 'circle' is the 1/4 in. long end piece, imbedded in the plexiglass window, as noted in Section 2.2.

46

It is clear from the first few frames that the flow
separates immediately at the sharp edges of the camber
and gives rise to two symmetrical vortices. The regions
of secondary separation near the rear edges of the camber
(see e.g., the 12th frame) are quite small. The vortices
continue to grow until the onset of deceleration (at
about the 15th frame). Subsequently, the vortices move
upward and sideways (see e.g., the 24th frame). It is
important to note that the separation points remain at
the edges of the camber throughout the deceleration
period.

One additional observation is worth noting. The
video pictures of the vortices along their span have
shown that the vortices cease to remain rectilinear,
particularly during the period of flow deceleration, and
acquire highly complex but continuous spiralling forms.
This is in spite of the fact that the model and the
starting flow were both made as two-dimensional as one
can possibly make them. Thus, the relatively small drag
force measured during the deceleration period is an
integrated average of the effects of this three-
dimensional instability on the pressure distribution.

It has been known for quite sometime that the three-
dimensional vortex dynamics plays an important role in
fluid mechanics. Even if the vortices are shed from the
body in a two-dimensional manner, three-dimensional

47

vortex instabilities distort the filament and the spanwise coherence of the pressure distribution, particularly when the flow is subjected to deceleration or when the vortex filaments are forced to return to their creator. The distortion of the vortex filament changes the core structure and gives rise to a self-induction velocity. The consequences of these changes are not yet calculable. However, it is rather fortunate that during the acceleration period the vortices grow rapidly and move away from the body and this seems either to prevent or delay the onset of the three-dimensional instability.

3.2 Model B

Figure 14 shows a representative plot of the variation of the drag coefficient with T^*. This figure is obtained from force-time records similar to those shown in Fig. 8. The comparison of the drag coefficients for the Model B, for various periods of the initial steady flow, also have shown that the drag coefficients prior to the onset of deceleration are nearly identical (the additional data are not shown in Fig. 14 for sake of clarity). As in the case of the Model A, the drag coefficients after the onset of deceleration are simply shifted in time by an amount equal to the difference between the durations of their steady-states. In other

48
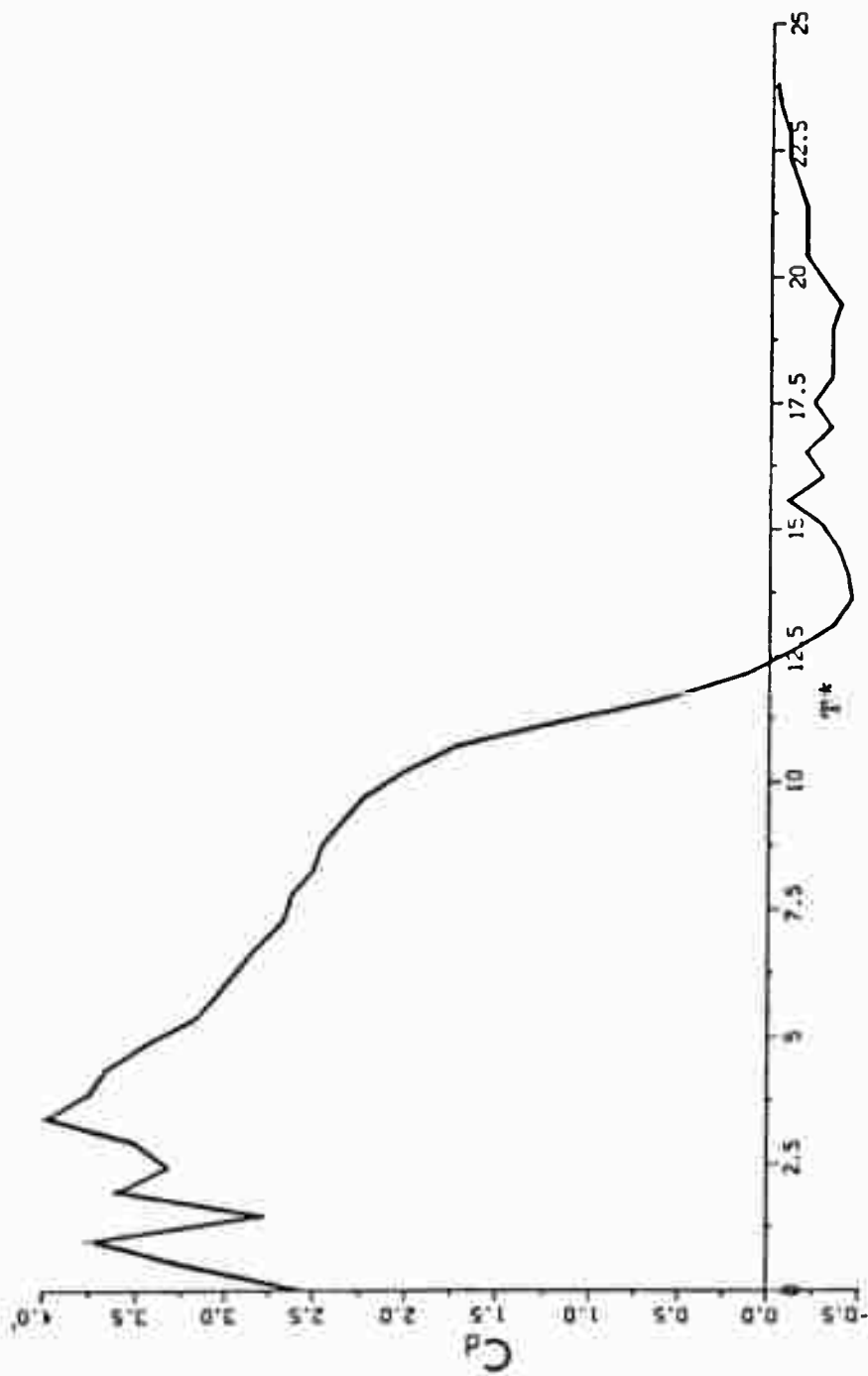
Fig. 14   Drag Coefficient versus T* for the Model B

49

words, the force acting on Model B is not materially affected by the duration of the ambient steady flow within the range of the parameters encountered in the present investigation.

As in the case of the Model A, the drag coefficient decreases rapidly at the onset of deceleration, goes through zero near the middle of the deceleration period, and through its minimum (negative) value at the end of the deceleration period (see Fig. 8). Subsequently, C_d gradually decreases to zero.

Figure 11 shows a sample sequence of the pictures depicting the growth and motion of vortices behind the Model B (no attempt has been made to select the frames at equal time intervals). In these pictures, the 'circle' is again the 1/4 in. long end piece, imbedded in the plexiglass window, as noted in Section 2.2.

It is clear from the first few frames that the flow separates immediately at the sharp edges of the camber and gives rise to two symmetrical vortices. The regions of secondary separation near the rear edges of the camber (see e.g., the 9th frame) are somewhat larger than those of the Model A. The vortices continue to grow until the onset of deceleration (at about the 16th frame). Subsequently, the vortices move upward and sideways (see e.g., the 20th frame) while the separation points remain at the edges of the camber.

50

The video pictures of the vortices along their span have also shown that the vortices cease to remain rectilinear, as in the case of the Model A, particularly during the period of flow deceleration, and acquire highly complex but continuous spiralling forms. Thus, the relatively small drag force measured during the deceleration period is, in fact, an integrated, spanwise averaged, three-dimensional pressure distribution.

3.3 Model C

Figure 15 shows a representative plot of the variation of the drag coefficient with T^*. This figure is obtained from force-time records similar to those shown in Fig. 9. The comparison of the drag coefficients for the Model C, for various periods of the initial steady flow, also have shown that the drag coefficients prior to the onset of deceleration are nearly identical. Furthermore, the drag coefficients after the onset of deceleration are simply shifted in time by an amount equal to the difference between the durations of their steady-states. In other words, the force acting on Model C is not materially affected by the duration of the ambient steady flow within the range of the parameters encountered in the present investigation.

Unlike the previous cases, however, the initial rise in the drag coefficient is followed first by a sharp
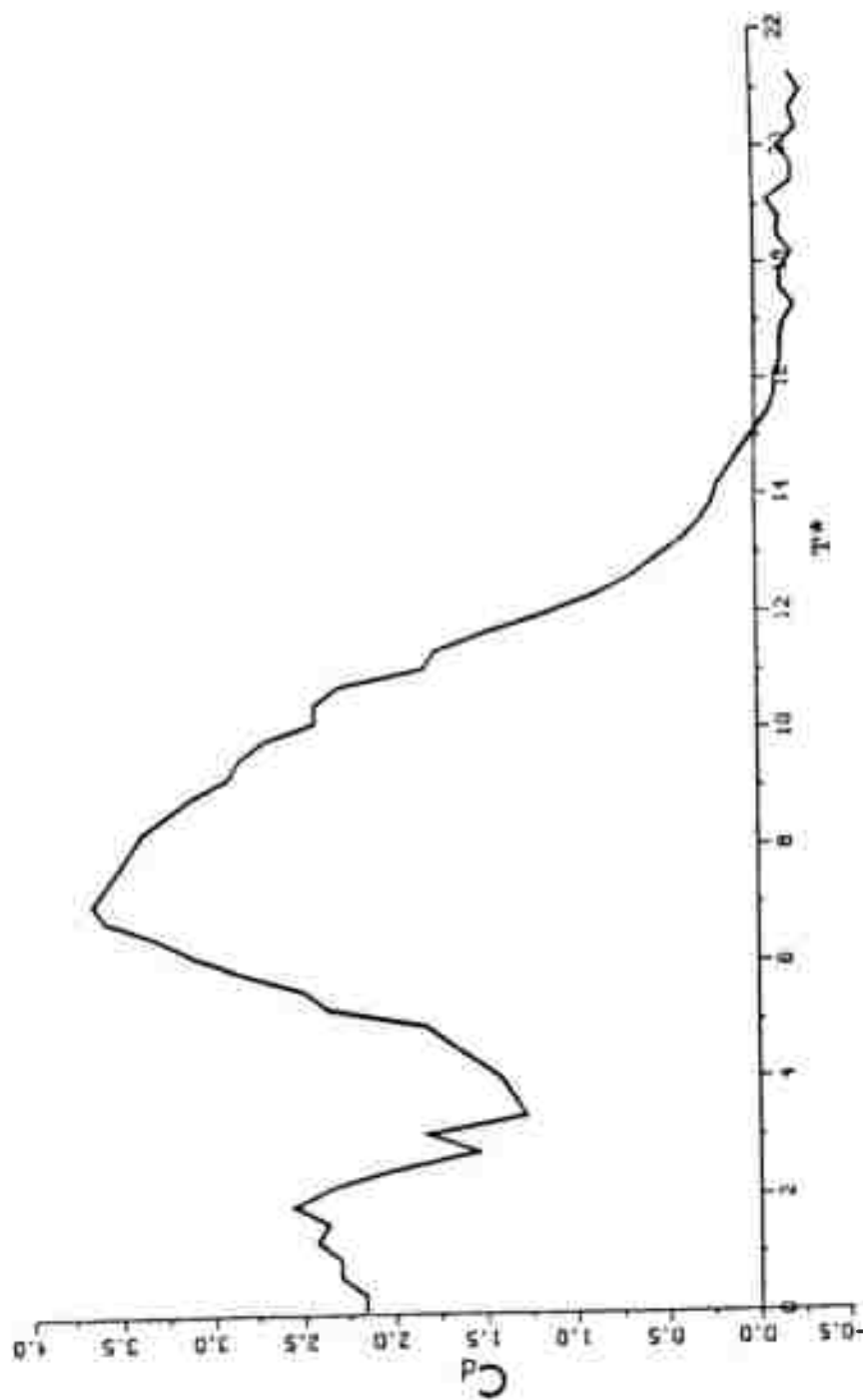
Fig. 15 Drag Coefficient versus T' for the Model C

decrease and then by a rise to a larger maximum. Subsequently, the drag coefficient decreases rapidly at the onset of deceleration, goes through zero near the middle of the deceleration period, and through a relatively small minimum (negative) value at the end of the deceleration period (see Fig. 9). Subsequently, C_d gradually decreases to zero.

Figure 12 shows a sample sequence of the pictures depicting the growth and motion of vortices behind the Model C. It is clear from the first few frames that the flow does not separate immediately at the sharp edges of the camber as in the previous two cases. The separation begins at the bottom stagnation point (see the 4th and 5th frames) and leads to the formation and growth of two small vortices (see the frames 7-12). The initial rise of the drag is partly due to the acceleration of the flow and partly due to the formation of these two small vortices. Subsequently, these vortices move towards the rear of the camber (the time at which the drag decreases sharply) and the separation points move rapidly to the edges of the camber (see frames 13 and 14). There is a time period during which there are four vortices in the wake (the two small vortices and the two larger vortices, resulting from the separation at the sharp edges), (see Frames 12-16). Subsequently, the small scale vortices are overtaken by or merge with the larger ones (see

frames 20-21). This merging takes place in a very short time (in about 0.03 seconds). The remaining vortices grow rapidly and give rise to two relatively large regions of secondary separation near the rear edges of the camber (see e.g., the 24th frame). The vortices continue to grow until the onset of deceleration (at about the 25th frame). Subsequently, the vortices move upward and sideways (see e.g., the 29th frame). It is important to note that separation during the period of deceleration occurs not only at the sharp edges but also at the downstream face of the camber (at about 30 degrees downstream from the edges) partly due to the presence of the large after body (240 degree arc) and partly due to the large velocities induced on it.

The video pictures of the vortices along their span have also shown that the vortices cease to remain rectilinear, as in the case of the Models A and B, particularly during the period of flow deceleration, and acquire highly complex but continuous spiralling forms. Thus, the relatively small drag force measured during the deceleration period is an integrated, spanwise averaged, complex, three-dimensional pressure distribution.

DISCRETE VORTEX MODEL OF UNSTEADY FLOW
ABOUT TWO-DIMENSIONAL CAMBERED PLATES

4.   INTRODUCTION TO ANALYSIS

4.1 Separated Flows

The separated flow about bluff bodies has been almost completely unyielding to both analysis and numerical simulation for a number of mathematical reasons and fundamental fluid dynamic phenomena.   Separation gives rise tc the formation of free shear layers which roll up into vortex rings or counter-rotating vortices. They, in turn, interact with each other, with the counter-sign vorticity generated at the base of the body, and with the motion of often unknown separation points. The wake becomes unsteady even for a steady ambient flow and the problem of the determination of the characteristics of the wake becomes coupled to the conditions prevailing upstream of the separation points. Evidently, viscosity modifies radically the inviscid flow, which, in this case, cannot serve even as a first approximation to the actual flow.   The boundary layer equations are not applicable beyond the separation points and are, therefore, of limited use in bluff-body flow problems.

The separated unsteady flow situations involving wake return, as in the case of a decelerating or

oscillating body, are an order of magnitude more complex than those where the vortices continuously move away from the body. The net effect of the wake return is twofold. Firstly, the proximity of the large vortices dramatically affects the boundary layer, outer flow, pressure distribution, and the generation and survival rate of the new vorticity. Secondly, the vortices not only give rise to additional separation points and/or additional vortices, but also strongly affect the motion of the primary vortices. These effects are further compounded by the diffusion and decay of vortices and by the three-dimensional nature of the flow.

The existing finite difference and finite element methods cannot yet treat the high Reynolds number flows with sufficient accuracy for a number of reasons. The finite difference schemes require a very fine grid, a turbulence model, and a very large computer memory. It seems that the modelling of the turbulent stresses in the wake, particularly in time-dependent flows will be the major source of difficulty in all future calculations. Whether or not it will ever be practical to apply the finite difference and finite element methods to high Reynolds number flows is unknown. The inherent difficulties are certainly significant enough to warrant exploring other solution methods.

Certain separated time-dependent flows may be simulated through the use of the discrete vortex model (DVM). The free shear layers which emanate from the sides of the body are represented by an assembly of discrete vortices. The strength of the elemental vortices are determined through the use of the Kutta condition. The use of a suitable convection scheme enables one to march in time and to calculate the evolution of the wake, the velocity and pressure distributions, and the lift and drag forces acting on the body. The work described herein deals with the application of the DVM to decelerating flow about two-dimensional cambered plates.

4.2 Flow About Parachutes: The Genesis of the Problem

The determination of the deployment sequence of an axisymmetric porous parachute and the unsteady aerodynamic loads acting on it presents a very complex coupled problem. The development of an analytical or numerical model which takes into account the effects of porosity, gaps, and variable opening schemes would allow numerical experiments on a large class of parachutes, reduce the number of the expensive field tests to a few judiciously selected ones, and enable the designer to calculate the time history of the fall of the parachute and the strength required to survive the aerodynamic

loads.   However, the development of such a model is
hampered by a number of difficulties.   In fact, it has
become evident that finite-difference or finite-element
solutions of complex, unsteady, separated, three-
dimensional flows at high Reynolds numbers will not be
possible before few decades, even for rigid bodies.   In
recent years, the vortex methods have been gaining
momentum because they offer a true alternative to Navier-
Stokes solutions (with a suitable closure model for
turbulence).   However, the vortex methods (often one
method per paper) have not yet become a reliable tool
which could be used to make predictions rather than to
mimic the observations and measurements through suitable
assumptions and fine tuning.   In fact, the method has
been both used and abused by many investigators.   It is
in light of the foregoing that one acquires a greater
appreciation of the difficulties associated with the
solution of the aforementioned coupled problem and of the
ingenious approximations introduced into the early models
during the past two decades.

The previous models for parachute loads are based by
and large on empirical assumptions (see e.g., Heinrich
and Saari 1978; McVey 1972; Cockrell 1987).   They rely on
the observation that families of parachutes open in a
characteristics length and seem to have aerodynamic
properties that relate well to the projected area of the

parachute. The apparent mass is assumed to be a function of the projected area only and is not a function of the prevailing flow characteristics. The vortex sheet analysis was used by Klimas (1977) to derive the acceleration-independent apparent mass coefficient for arbitrary-shaped axisymmetric surfaces. Muramoto and Garrard (1984) used a continuous-source model to predict the steady-state drag of ribbon parachutes. These analyses did not, however, deal with the evolution of the unsteady wake and its interaction with the canopy.

It is in view of the foregoing that a fundamental study of the separated time-dependent flow about two-dimensional rigid cambered plates were undertaken. Clearly, the flow about a rigid cambered plate is considerably simpler than that about a porous, axisymmetric, and flexible parachute and the results, regardless of the degree of their agreement with corresponding experiments, may not have direct relevance to the practical problem under consideration. But the object of this investigation was the understanding of the evolution of the wake under controlled conditions rather than to provide a design tool. It is hoped that an investigation of this type will reveal the underlying physics of the phenomenon (particularly that of the parachute collapse), help to interpret the full-scale results and will provide inspiration for the development

59

of more general vortex models with which the dynamics of axisymmetric, porous, and flexible parachute canopies can be investigated. Efforts directed towards the development of a general numerical model, driven by the ever-present pressures of practical considerations, are deemed somewhat premature. Such efforts will have to face not only the problem itself but also the deficiencies of the vortex models and attempt to address to both of them simultaneously. The model presented herein removes the ambiguities associated with the use of the discrete vortex model and provides results which are for the cambers of smaller included angle in excellent agreement with those obtained experimentally.

5   ANALYSIS

5.1   Transformations and the Complex Velocity Potential

The calculation of the velocity of any one of the vortices and the force acting on the body requires a conformal transformation (in which the camber becomes a circle), a complex-velocity potential representing the vortices, their images, and the two-dimensional irrotational flow around the body, and the use of the generalized Blasius theorem.

The flow in the circle plane may be transformed to that about a cambered plate through the use of two successive transformations, one from ζ plane to the ζ° plane and the other from the ζ° plane to the z plane. These are given by (see Fig. 16)

$$z = \zeta^\circ - \frac{b^2}{\zeta^\circ} , \quad \text{and } \zeta^\circ = \zeta + m \tag{1}$$

Combining the two, one has a direct transformation from the ζ plane to the z plane as

$$z = \zeta + m - \frac{b^2}{\zeta + m} \tag{2}$$

It is easy to show that the camber in the z plane is a circular arc.

The y-axis in the z plane passes through the tips of the camber.   It is advantageous to locate the origin of
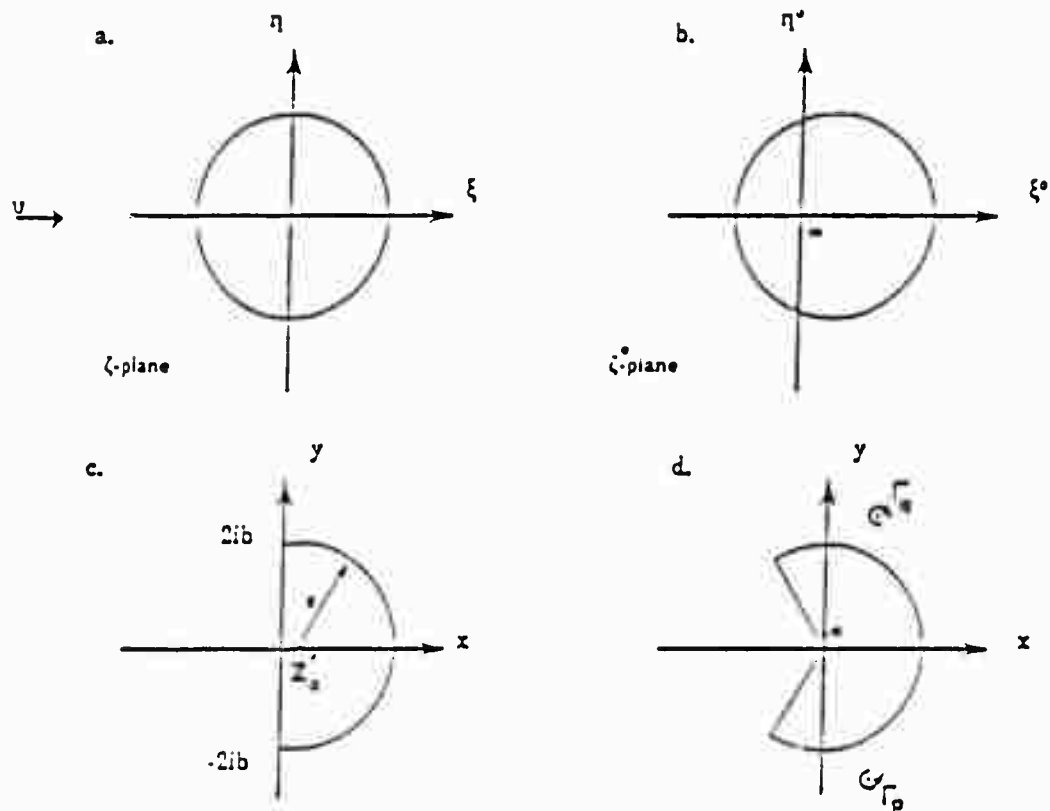
61

Fig. 16 Circle and Physical Planes

the coordinate axes at the geometric center of the camber, i.e., at the center of the circle part of which represents the camber. This is easily accomplished by shifting the origin of the coordinate axes by

$$z'_o = \frac{2m^2 - 1}{m} \qquad (3)$$

where z'_o is the x coordinate of the origin of the circle

in the z plane. Thus, one has

$$z = \zeta + m - \frac{b^2}{\zeta + m} + z_0 \quad \text{with } z_0' = -z_0 \qquad (4)$$

which transforms the circle in Fig. 16a to the physical plane in Fig. 16d. Table 1 summarizes the relationship between m, z_0', the included angle of the camber, b, and the radius of the camber.

Table 1   Summary of the parametric relationships

m	z_0'	2	b	R=1/m
cos60 = 0.5	-1	120	0.866	2
cos45 = 0.707	0	180	0.707	$\sqrt{2}$
cos30 = 0.866	$1/\sqrt{3}$	240	0.5	$2/\sqrt{3}$

The complex potential function w in the circle plane (see Fig. 16a) which describes a uniform flow U (assumed to be time-dependent) with a doublet at the origin to simulate the cylinder, $\Gamma_{k,q}$ clockwise-rotating vortices (called q-vortices), $\Gamma_{k,p}$ counter-clockwise-rotating vortices (called p-vortices), and the images of all the p- and q-vortices in the circle plane may be written as

$$W = -U\left(\zeta + \frac{c^2}{\zeta}\right) + \frac{i\Gamma_{0p}}{2\pi}\text{Ln}(\zeta - \zeta_{0p}) - \frac{i\Gamma_{0p}}{2\pi}\text{Ln}\left(\zeta - \frac{c^2}{\overline{\zeta}_{0p}}\right)$$

$$+ \sum_{k=1}^{m}\frac{i\Gamma_{kp}}{2\pi}\text{Ln}(\zeta - \zeta_{kp}) - \sum_{k=1}^{m}\frac{i\Gamma_{kp}}{2\pi}\text{Ln}\left(\zeta - \frac{c^2}{\overline{\zeta}_{kp}}\right) - \frac{i\Gamma_{0q}}{2\pi}\text{Ln}(\zeta - \zeta_{0q})$$

$$+ \frac{i\Gamma_{0q}}{2\pi}\text{Ln}\left(\zeta - \frac{c^2}{\overline{\zeta}_{0q}}\right) - \sum_{k=1}^{m}\frac{i\Gamma_{kq}}{2\pi}\text{Ln}(\zeta - \zeta_{kq}) + \sum_{k=1}^{m}\frac{i\Gamma_{kq}}{2\pi}\text{Ln}\left(\zeta - \frac{c^2}{\overline{\zeta}_{kq}}\right) \quad (5)$$

in which Γ_{kp} and ζ_{kp} represent respectively the strength
and location of the k-th p-vortex, Γ_{kq} and ζ_{kq} the
strength and location of the k-th q-vortex, and c the
radius of the cylinder; an overbar indicates a complex
conjugate. The need for the separate identification of
the p- and q-vortices and for the singling out of one of
the vortices in each shear layer (namely, Γ_{0p} and Γ_{0q},
the nascent vortices) will become apparent later.

5.2 Complex Velocities of Vortices

The convection of the vortices and the calculation
of the forces acting on the body require the evaluation
of the velocities at the vortex centers. For the
velocities in the circle plane this reduces to
subtracting from Eq. (5) the complex potential
corresponding to the vortex for which the velocity
components are to be determined and evaluating the

64

derivative of the remaining terms at $\zeta = \zeta_k$. To determine the velocities in the physical plane, however, one has to subtract $(i\Gamma_k/2\pi)Ln(z - z_k)$ from Eq. (5) or, in terms of ζ, the terms (see e.g., Sarpkaya 1967, 1975)

$$\frac{i\Gamma_k}{2\pi} Ln\,(\zeta - \zeta_k) + \frac{i\Gamma_k}{2\pi} Ln\left[1 + \frac{b^2}{(\zeta + m)(\zeta_k + m)}\right] \qquad (6)$$

It should be noted that the first term in Eq. (6) is the complex function corresponding to the k-th vortex in the ζ plane. The second term appears merely as a consequence of the transformation used.

The above procedure may be generalized as follows. Consider the potential function for a single vortex in the physical plane and ignore, for the time being, the multiplier in front of the logarithmic term (i.e., $i\Gamma_k/2\pi$). Then one has

$$Ln(z - z_v) = Ln[\,f(\zeta) - f(\zeta_v)\,] \quad \text{with } z = f(\zeta) \qquad (7)$$

Equation (7) may be written as

$$Ln\,(z - z_v) = Ln\,(\zeta - \zeta_v) + Ln\frac{f(\zeta) - f(\zeta_v)}{\zeta - \zeta_v} \qquad (8)$$

Evidently, the first term on the right hand side of Eq. (8) represents the vortex in the circle plane. Let us

65

now examine the derivative of the second term with respect to z. One has,

$$\frac{dW}{dz}_P = \left[\frac{d}{d\zeta}\left(\frac{f(\zeta) - f(\zeta_v)}{\zeta - \zeta_v}\right)\right]\left(\frac{f(\zeta) - f(\zeta_v)}{\zeta - \zeta_v}\right)^{-1} \frac{d\zeta}{dz} \qquad (9)$$

where $dz/d\zeta = f'(\zeta)$. In the neighborhood of ζ_v the function $f(\zeta)$ may be expanded as follows,

$$f(\zeta) - f(\zeta_v) = (\zeta - \zeta_v)f'(\zeta_v) + \frac{(\zeta - \zeta_v)^2}{2}f''(\zeta_v) + \dots \qquad (10)$$

Thus, one has

$$\frac{dW}{dz}_P = \lim_{\zeta \to \zeta_v}\left[\frac{1/2\, f''(\zeta_v)}{\dfrac{f(\zeta) - f(\zeta_v)}{\zeta - \zeta_v}}\right]\frac{1}{f'(\zeta)} \qquad (11)$$

or

$$\frac{dW}{dz}_P = \frac{f''(\zeta_v)}{2f'^2(\zeta_v)} \qquad (12)$$

Thus, the complex velocity in the physical plane reduces to

66

$$-u_x + iv_y = \frac{d}{d\zeta}\left[W(\zeta) - \frac{i\Gamma}{2\pi} \text{Ln}\,(\zeta - \zeta_v) \right] \frac{1}{f'(\zeta)}\bigg|_{\zeta\,=\,\zeta_v} - \frac{i\Gamma}{4\pi} \frac{f''(\zeta_v)}{f'^2(\zeta_v)} \qquad (13)$$

in which for a p-vortex

$$f'(\zeta_{kp}) = 1 + \frac{b^2}{(\zeta_{kp} + m)^2} \qquad (14)$$

and

$$f''(\zeta_{kp}) = -\frac{2b^2}{(\zeta_{kp} + m)^3} \qquad (15)$$

The last term in Eq. (13) reduces to

$$-\frac{i\Gamma_{kp}}{2\pi} \frac{(-b^2)(\zeta_{kp} + m)}{[(\zeta_{kp} + m)^2 + b^2]^2} \qquad (16)$$

This result could have been deduced directly from Eq. (6). However, the generalization of the method enables one to apply Eq. (13) to any vortex for any transformation between the circle and the physical plane.

67

5.3 Kutta Condition

The fact that the flow separates tangentially with a finite velocity at the edges of the plate (Kutta condition) may be expressed by requiring

$$\frac{dW}{d\zeta} = 0 \qquad \text{at } \zeta = \zeta_t = -m \pm ib \qquad (17)$$

Thus, inserting Eq. (5) in Eq. (17), one has

$$+\frac{i\Gamma_{0p}}{2\pi}\left(\frac{1}{\zeta_t - \zeta_{0p}} - \frac{1}{\zeta_t - \frac{c^2}{\bar{\zeta}_{0p}}}\right) - \frac{i\Gamma_{0q}}{2\pi}\left(\frac{1}{\zeta_t - \zeta_{0q}} - \frac{1}{\zeta_t - \frac{c^2}{\bar{\zeta}_{0q}}}\right)$$

$$+\sum_{k=1}^{m}\frac{i\Gamma_{kp}}{2\pi}\left(\frac{1}{\zeta_t - \zeta_{kp}} - \frac{1}{\zeta_t - \frac{c^2}{\bar{\zeta}_{kp}}}\right) - \sum_{k=1}^{m}\frac{i\Gamma_{kq}}{2\pi}\left(\frac{1}{\zeta_t - \zeta_{kq}} - \frac{1}{\zeta_t - \frac{c^2}{\bar{\zeta}_{kq}}}\right)$$

$$-U\left(1 - \frac{c^2}{\zeta_t^2}\right) = 0. \qquad (18)$$

Equation (18) may be decomposed into two parts as

$$+\frac{i\Gamma_{0p}}{2\pi}\left(\frac{1}{\zeta_t - \zeta_{0p}} - \frac{1}{\zeta_t - \frac{c^2}{\bar{\zeta}_{0p}}}\right) - \frac{i\Gamma_{0q}}{2\pi}\left(\frac{1}{\zeta_t - \zeta_{0q}} - \frac{1}{\zeta_t - \frac{c^2}{\bar{\zeta}_{0q}}}\right)$$

$$+ (-u_o + iv_o) = 0. \qquad (19)$$

where the terms containing the strength of the nascent vortices represent the velocity induced at the tip of the

camber by the nascent vortices and the term in parenthesis the velocity at the tip due to all other vortices (and their images), the doublet at the center of the circle in the ζ plane and the ambient velocity.

Equation (19) represents two coupled equations for the strengths and positions of the nascent vortices. Thus, the solution of the said quantities does, in general, require an iteration. However, this iteration may be avoided by noting that the velocity induced by a nascent vortex at the opposite tip is very small and certainly negligible. Thus, Eq. (19) for one of the nascent vortices may be reduced to

$$-\frac{i\Gamma_{0q}}{2\pi}\left(\frac{1}{\zeta_t - \zeta_{0q}} - \frac{1}{\zeta_t - \dfrac{c^2}{\overline{\zeta}_{0q}}}\right) + (-u_o + iv_o) = 0 \qquad (20)$$

A similar expression may be written for the other nascent vortex. The use of the Kutta condition, as expressed by Eq. (20), will be explained further later following the discussion of the tip velocity. It suffices to note that all nascent vortices satisfying the Kutta condition do not yield either the same tip velocity or the same velocity distribution in the neighborhood of the tip. There are, in fact, certain preferred positions for the nascent vortices which yield physically realistic

velocity distributions near the tips of the cambered plate. These nascent vortex positions will be discussed later.

5.4 Tip Velocity

According to the Kutta condition the tangential velocity at the tip is finite. The purpose of the following is to determine this finite velocity. It may be determined either through the use of l'Hopital's rule or through the use of a more general expression which is valid for all other transformations.

The velocity at the tip is given by

$$\frac{dW}{dz} = \frac{dW}{d\zeta} \cdot \frac{d\zeta}{dz} \qquad \text{at} \quad z_t = z_o \pm 2ib \tag{21}$$

For an arbitrary point z, Eq. (4) yields,

$$\frac{d\zeta}{dz} = \frac{1}{2} \pm \frac{\sqrt{ib}}{2\sqrt{z - z_t}} \tag{22}$$

In general, one may write Eq. (22) as

$$\frac{d\zeta}{dz} = \frac{1}{2} \pm \frac{(z - z_o)}{2\sqrt{(z - z_o)^2 + 4b^2}} \tag{23}$$

or multiplying both sides with $\sqrt{(z-z_t)}$, one has,

$$f(z) = (z - z_t)^{1/2} \frac{d\zeta}{dz}$$

$$= \frac{1}{2} (z - z_t)^{1/2} \pm \frac{(z - z_0)}{2\sqrt{z - (z_0 \pm 2ib)}} \tag{24}$$

Thus, for $z_t = z_0 \pm 2ib$, one has

$$f(z_t) = (z - z_t)^{1/2} \frac{d\zeta}{dz} = \frac{1}{2} \sqrt{ib} \tag{25}$$

or

$$\frac{d\zeta}{dz} = \frac{\sqrt{ib}}{2\sqrt{(z - z_t)}} = \frac{2f^2(z_t)}{\zeta - \zeta_t} \tag{26}$$

Expanding $dw/d\zeta$ in the neighborhood of ζ_t, one has

$$\frac{dW}{d\zeta} = (\zeta - \zeta_t) W''(\zeta_t) + \dots \tag{27}$$

Combining Eqs. (26) and (27) one finally has,

$$\left. \frac{dW}{dz} \right|_{z = z_t} = 2 \frac{d^2W}{d\zeta^2} f^2(z_t) \tag{28}$$

Noting that for the case under consideration $f^2(z_t) = ib/4$, one has,

71

$$\left.\frac{dW}{dz}\right|_{z=z_t} = \frac{d^2W}{d\zeta^2} \cdot \left(\frac{ib}{2}\right) \tag{29}$$

Equation (29) yields the desired finite tip velocities. It is easy to show that it may be obtained directly from Eq. (21) through the use of l'Hopital's rule.

5.5 Time-Dependent Forces

The force acting on the body in the physical plane may be calculated either through the use of the pressure distribution or through the use of the rate of change of impulse.

Bernoulli's equation for unsteady flow is given by

$$\left(\frac{P_1}{\rho} + \frac{V_1^2}{2}\right) - \left(\frac{P_2}{\rho} + \frac{V_2^2}{2}\right) - \int_1^2 \frac{\partial V}{\partial t}\, ds = f(t) \tag{30}$$

where the indices indicate two points on the body in the physical plane. Since there is no pressure drop across the shear layer and since the integral term in Eq. (30) is zero at the tip (i.e., ds = 0), one has

$$f(t) = \frac{V_{t1}^2}{2} - \frac{V_{t2}^2}{2} \tag{31}$$

72

where V_{t1} and V_{t2} represent the tangential velocities on the upstream and downstream faces of the tip. It is important to note that $f(t)$ in Eq. (31) is also the time rate of change of circulation, i.e., the rate at which vorticity is shed into the wake from the tip of the cambered plate.

The normalized form of Bernoulli's equation between any two points then becomes

$$\frac{P_m - P_n}{\rho U_o^2/2} = \frac{V_{t1}^2 - V_{t2}^2}{U_o^2} + \frac{V_n^2 - V_m^2}{U_o^2} + \frac{\partial}{\partial t} \int_m^n 2 \frac{V}{U_o^2} ds \qquad (32)$$

The integration of the differential pressure between the upstream and downstream faces of the camber yields the force components in the x and y directions, i.e., the drag and lift forces.

The force acting on the body can also be calculated through the rate of change of impulse. It is given by

$$F = 4\pi\rho c^2 \dot{U} (1 - \frac{m^2}{2c^2}) + \frac{\partial}{\partial t}[\, \Gamma_n (z_n - z_{ni}) \,] \qquad (33)$$

which may be written as

$$C_d + i\, C_L = \frac{F}{2\rho U_o^2 b} = 2\pi(\frac{c\dot{U}}{U_o^2})(\frac{c}{b})(1 - \frac{m^2}{2c^2})$$

$$+ \frac{c}{2b} \frac{\partial}{\partial(U_o t/c)} \{\frac{\Gamma_k}{U_o c} [f(\frac{\zeta_k}{c}) - f(\frac{c}{\bar{\zeta}_k})]\} \qquad (34)$$

73

in which U_o is the reference velocity; $\dot{U}$, the rate of deceleration of flow and $z = f(\zeta_k)$, i.e., the transformation given by Eq. (4). Equation (34) may also be deduced directly from the generalized Blasius equation. It is important to note that the force calculated from Eq. (34) includes the effect of the rate of change of circulation between two successive time steps. Thus, it may be smaller or larger (depending on the sign of Γ) than the force calculated through the integration of the instantaneous differential pressure [Eq. (32)]. This is because of the fact that the instantaneous pressure depends only on the prevailing flow conditions and does not account for the rate of change of total circulation between successive time steps. In the calculations to follow U_o and c are taken as unity for sake of simplicity.

5.6 Method of Calculation

The use of the discrete vortex model (DVM) requires certain decisions to be made regarding the flux of vorticity; introduction of the nascent vortices; the convection, cancellation and combination of all other vortices; and the time interval to be used in the creation and convection of the vortices. Even though some subjective decisions are required in the selection

74

of the proper values and procedures (which makes one application of DVM differ from another), it is important that the basic and experimentally observed facts are not contradicted, the numerical procedure used to implement the method is stable, and that the results do not critically depend on the magnitude of disposable parameters introduced.

The methods used in the past in the determination of the rate of vorticity may be roughly classified into two broad categories. The first of these involves the use of variable nascent vortex positions (see e.g., Sarpkaya 1968, 1975) and the second the use of fixed nascent vortex positions (see e.g., Clements 1973-1975).

The method of fixed positions involves the selection of a suitable fixed point in the flow near the separation point and the use of the velocity U_s at that point to calculate the rate at which vorticity is shed into the wake from

$$\frac{\partial \Gamma}{\partial t} = \frac{1}{2} U_s^2 \tag{35}$$

In this method the positions of the nascent vortices are the crucial parameters. The previous applications of this method did not examine the effect of the position of the nascent vortices on the velocity distribution in the

75

neighborhood of the separation point. Only the distance of the fixed point to the body was varied and bracketed between two subjective limits by comparing the calculated results with those obtained experimentally. In this method no interaction is allowed between the shed vortices and the amplitude of oscillation of the point or the time of appearance of the nascent vortices. Furthermore, the time interval is chosen more or less arbitrarily (Kiya and Arie 1977) (repeating a few calculations with a single program with only the time step changed and also by referring to the results of the previous investigations). Thus, the velocities at the outer edges of the shear layers are only indirectly related to the strength of the nascent vortices and the fixed time interval. Evidently, the velocities in the inner and outer edges of the shear layers, the time interval, the strength and position of the nascent vortices, and the Kutta condition are interdependent and that both the position of the nascent vortices and the time interval cannot be chosen arbitrarily, even if they are chosen judiciously on the basis of previous experience and trial calculations.

Sarpkaya (1975) used the method of variable nascent vortex positions and determined the rate of shedding of vorticity from the relation

$$\frac{\partial \Gamma}{\partial t} = \frac{1}{2} U_{sh}^2 \qquad (36)$$

where U_{sh} is interpreted as the velocity in the shear
layers calculated by using the average of the transport
velocities of the first four vortices in each shear
layer. The positions of the nascent vortices are chosen
so as to satisfy the Kutta condition at the edges of the
body and thus they can move slightly with time. Thus,
this method simulates in a satisfactory manner the
mechanism of feedback from wake fluctuations to the
fluctuations in the rate of circulation. The number of
disposable parameters is reduced to a minimum and in this
sense this method is superior to the method of fixed
positions. However, the use of the average of the
transport velocities of the first four vortices remained
questionable.

It was often assumed that the vorticity flux could
not be calculated, at each time interval, as it is
applied to sharp-edged bodies, through the use of the
mathematically finite velocity occurring at the sharp
edges of the body. This assumption was based on the fact
that the separation points are singularities of the
transformation used and the numerical procedures may not
be stable.

It is on the basis of the foregoing that an original study was undertaken to establish once and for all a method whereby the nascent vortices may be introduced into the flow without any ambiguities. The method finally arrived at will be explained through the use of a series of figures and velocity plots.

Figures 17a and 17b show the tip region in the circle and physical planes, respectively. The regions A and B in Fig. 17a were discretized through the use of a suitable grid and a single vortex was placed at a grid point. The strength of the vortex was determined from the Kutta condition [Eq. (20)]. Then the velocity normal to the radial line OM in the physical plane (Fig. 17b) was calculated in the vicinity of the tip through the use of the complex velocity potential.
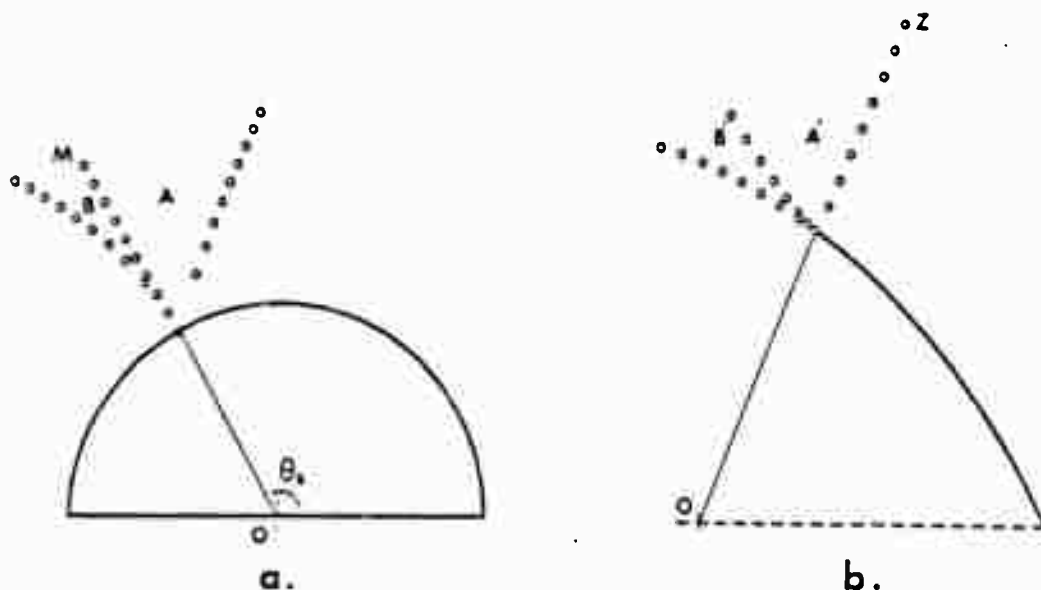
Fig. 17 Tip Region in the Circle and Physical Planes

Placing the vortex along the radial line OM (in the ζ plane) yields a single valued tip velocity independent of the strength and the position of the vortex and dependent on the plate geometry, i.e., b and 0_s. It is easy to show that the velocity at the edge of the plate reduces to $q_t = \pm (ib/2)\, e^{-3i\theta s}\, (-1 - e^{-2i\theta s})$. For the case of a 120-degree camber this gives an absolute value of 0.433 with a velocity direction opposite to that expected at the edge of the plate (Fig. 18).

Placing the nascent vortex to the right of the radial line OM in the circle plane (or along the circular arc in the physical plane) always requires a stronger vortex to satisfy the Kutta condition and thus results in a tip velocity which is unrealistic both in magnitude and direction (see Fig. 19).

Placing the nascent vortex along the radial line OZ in the physical plane or outside the region A shifts the point of maximum velocity away from the edge of the plate (towards the downstream side). This, in turn results in a leakage of fluid through the shear layer and requires a stronger vortex to satisfy the Kutta condition (see Fig. 20).

The entire region A enclosed by the transformation of the radial line OZ in the physical plane and the radial line OM in the ζ plane, is examined to determine
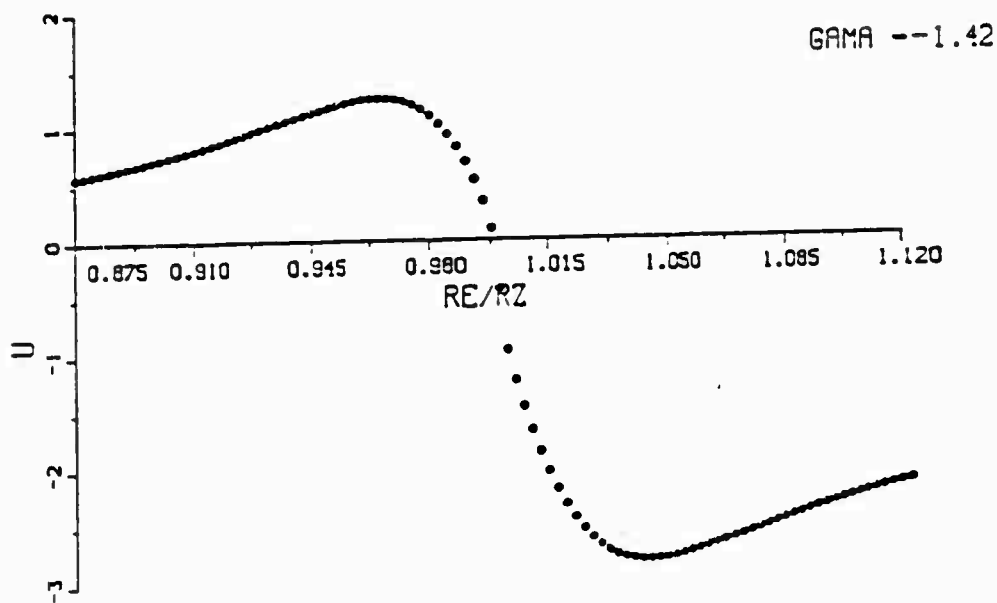
Fig. 18   Velocity Profile along the Radial Line
          (Nascent Vortex on OM)

GAMA --2.28
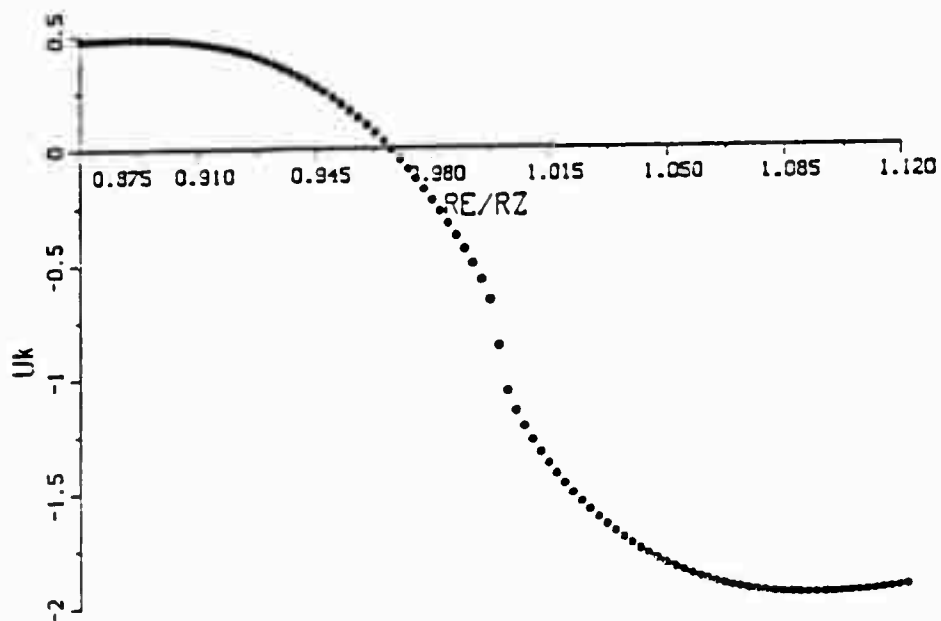
Fig. 19 Velocity Profile along the Radial Line
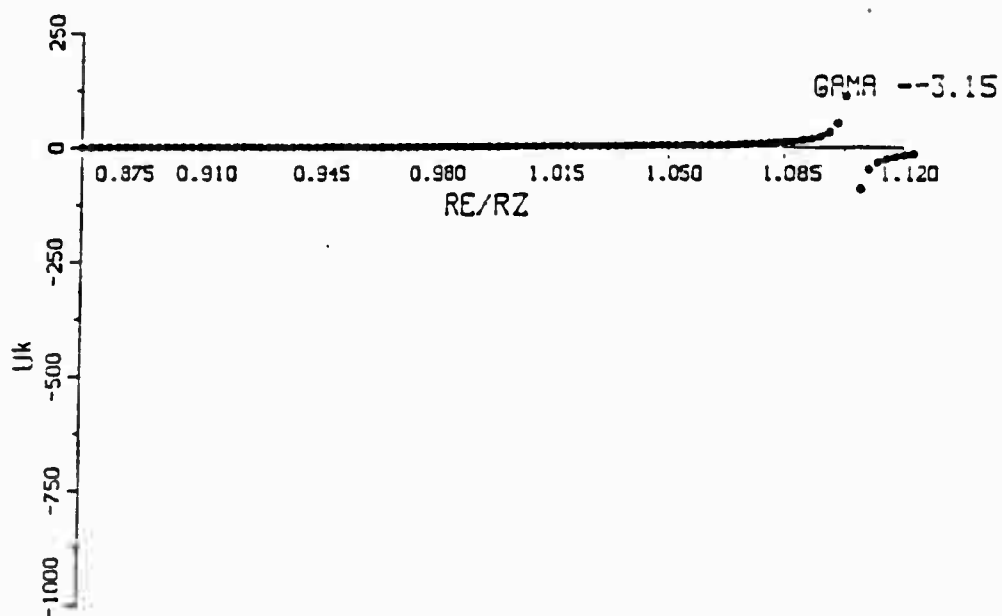(Nascent Vortex to the Right of OM)

nascent vortex

GAMA --3.15

RE/RZ

Uk

Fig. 20 Velocity Profile along the Radial Line
(Nascent Vortex on OZ)

82

the most appropriate positions of the nascent vortex. Figures 21 through 23 show a three-dimensional plot and the contour lines of Γ, U(max)/U(tip), and U(tip) as a function of the radial positions R and the angular positions Rθ for those locations of the nascent vortex for which $\Gamma<1$, U(max)/U(tip) < 6, and U(tip) < 6.

Figures 24 through 26 show three representative velocity profiles for three different positions of the nascent vortex in the region defined above. The most striking feature of these figures is that the maximum velocity near the tip can exceed considerably (and unrealistically) the velocity at the tip and that only for certain vortex positions does the maximum velocity (the velocity in the inner face of the camber near the tip) approach smoothly the finite velocity at the tip. This is in conformity with the fact that in inviscid flows the velocity and acceleration extrema can occur only on the body. Extensive calculations have shown that there is, in fact, a finite region in which the nascent vortices may be introduced in order to produce a tip velocity which is nearly equal to the maximum velocity in the vicinity of the tip. Clearly, it is only for unique combinations of the radial distance R and the angular position Rθ that the said velocity ratio is equal to unity (for additional details see: Mostafa 1987 and Munz 1987).
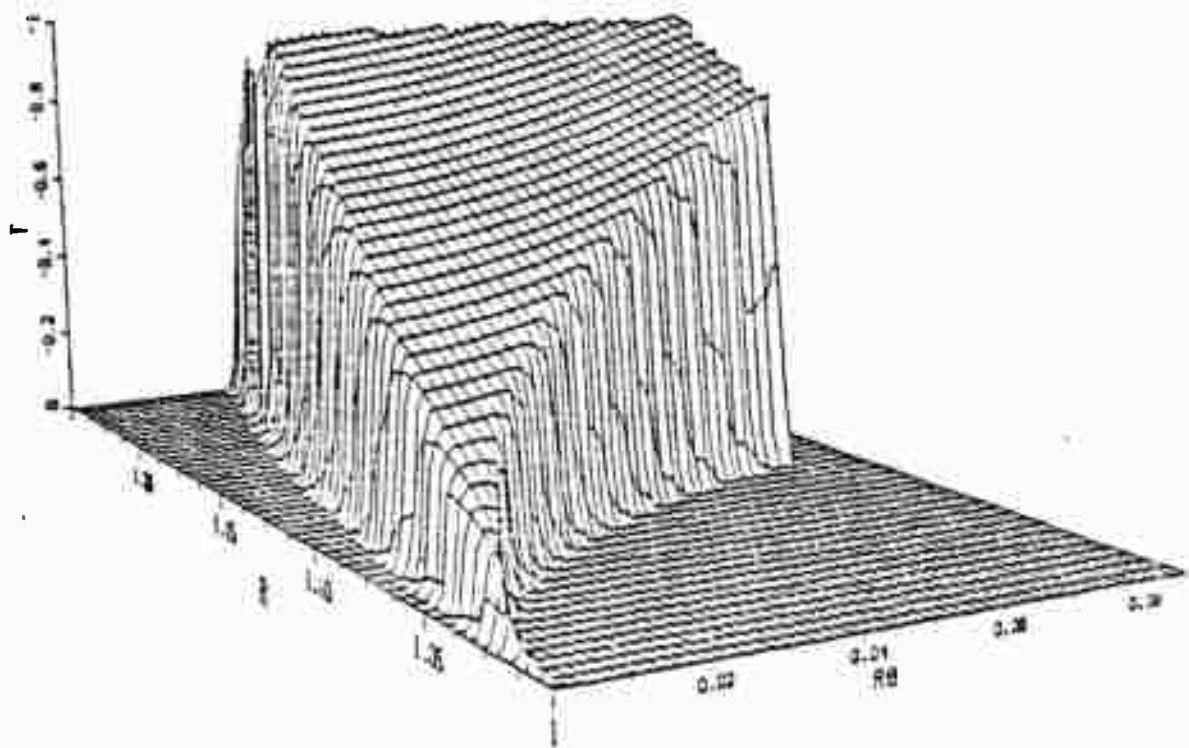
83
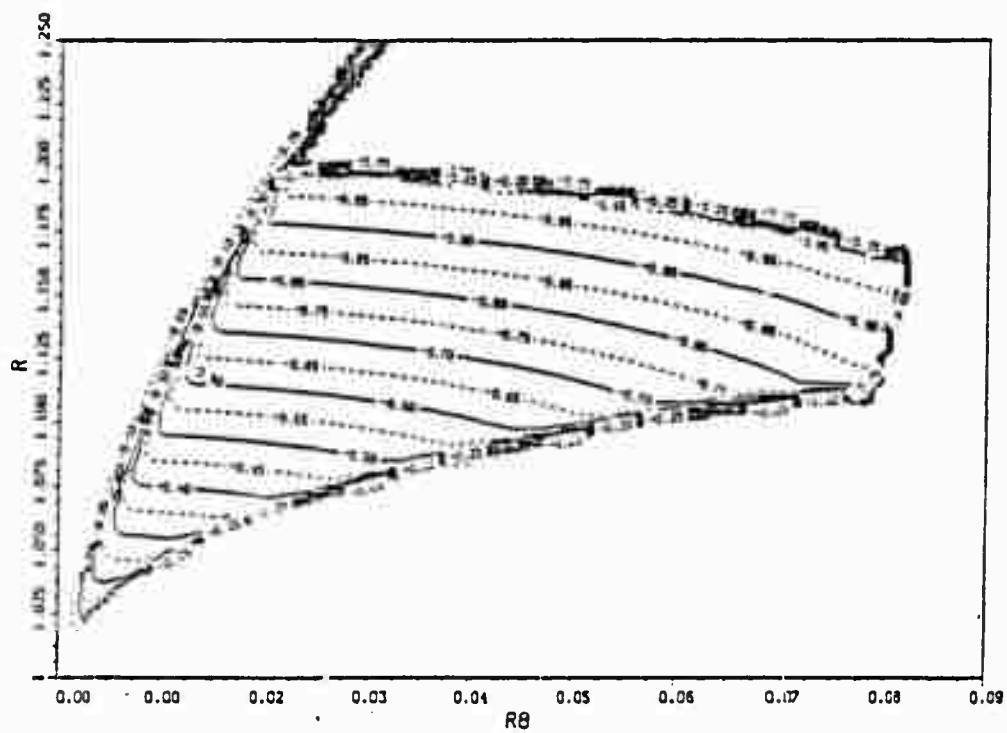
Fig. 21 Three-Dimensional Plot of and the Contour Lines for
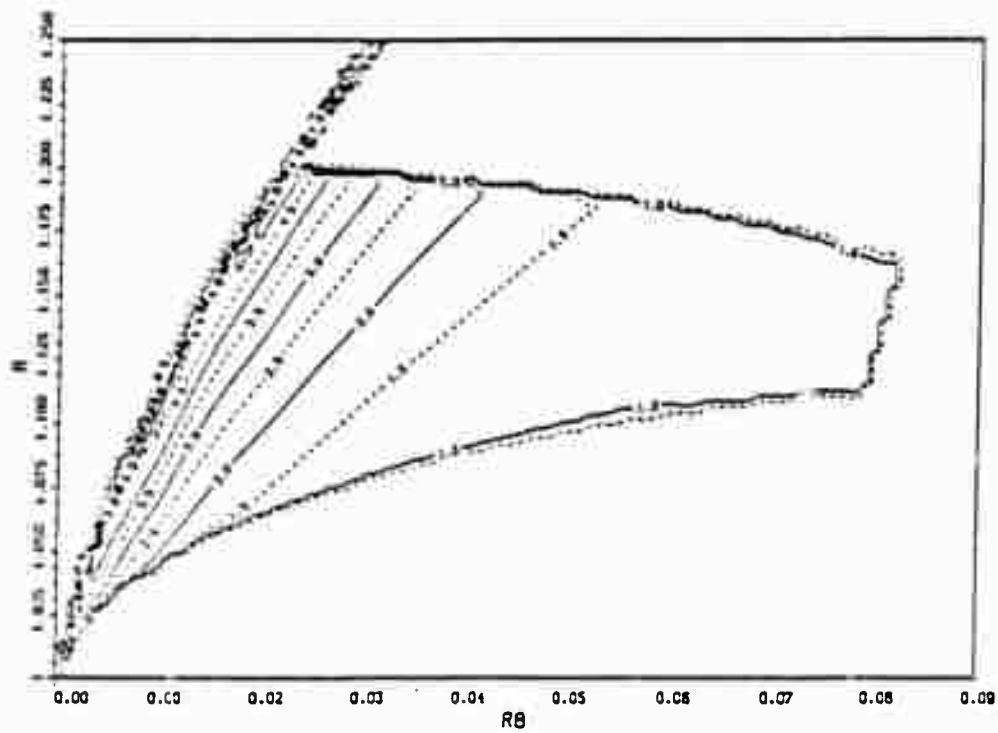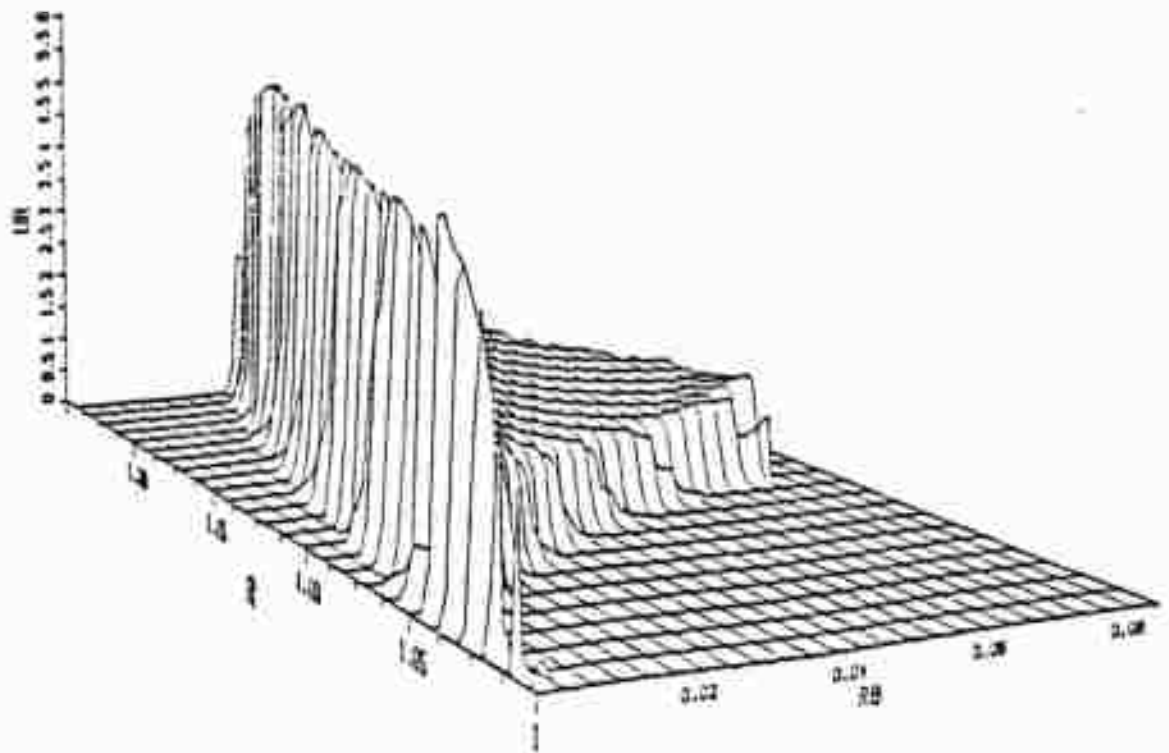Γ Distribution
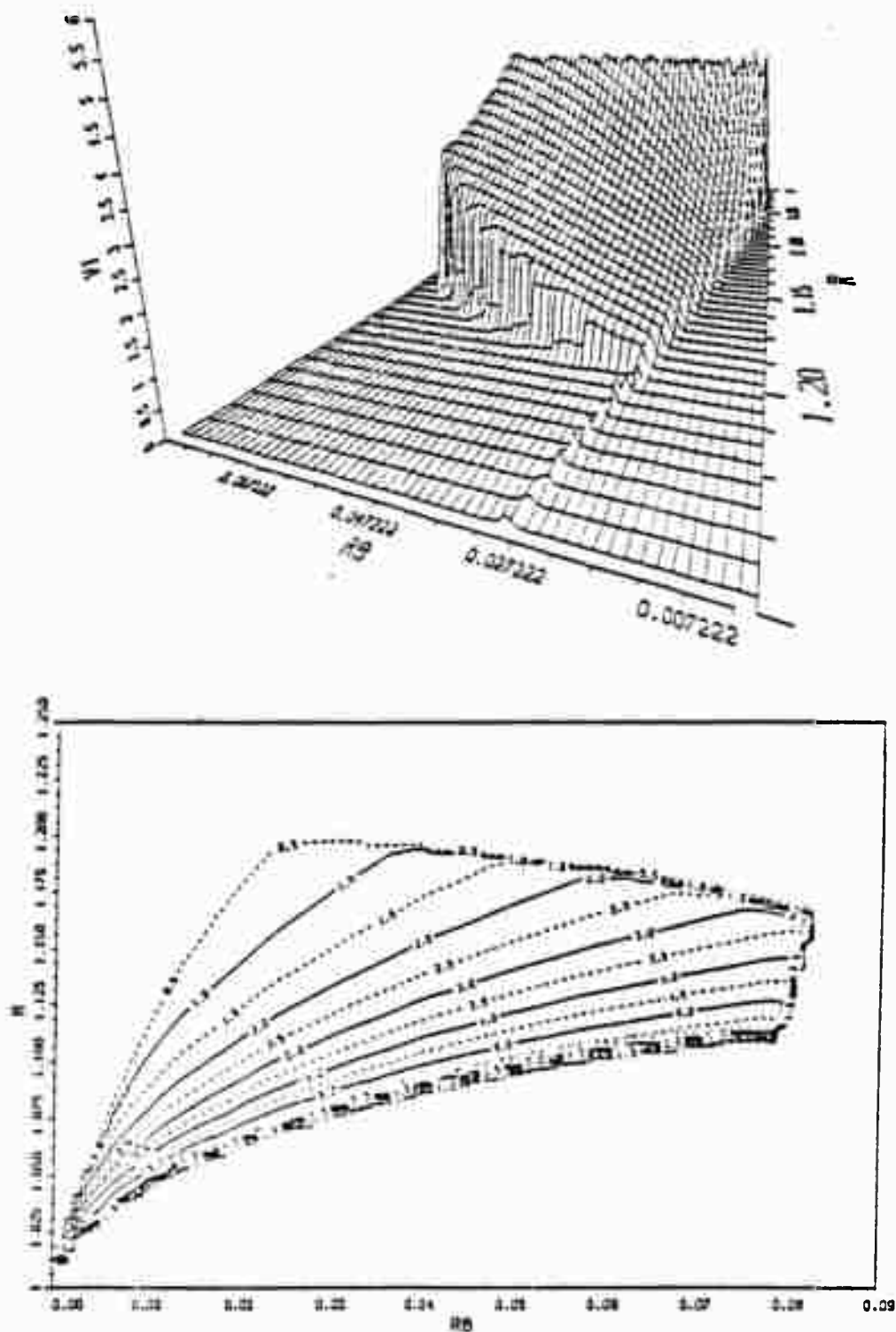
84

Fig. 22 Three-Dimensional Plot of the Velocity Ratio

85

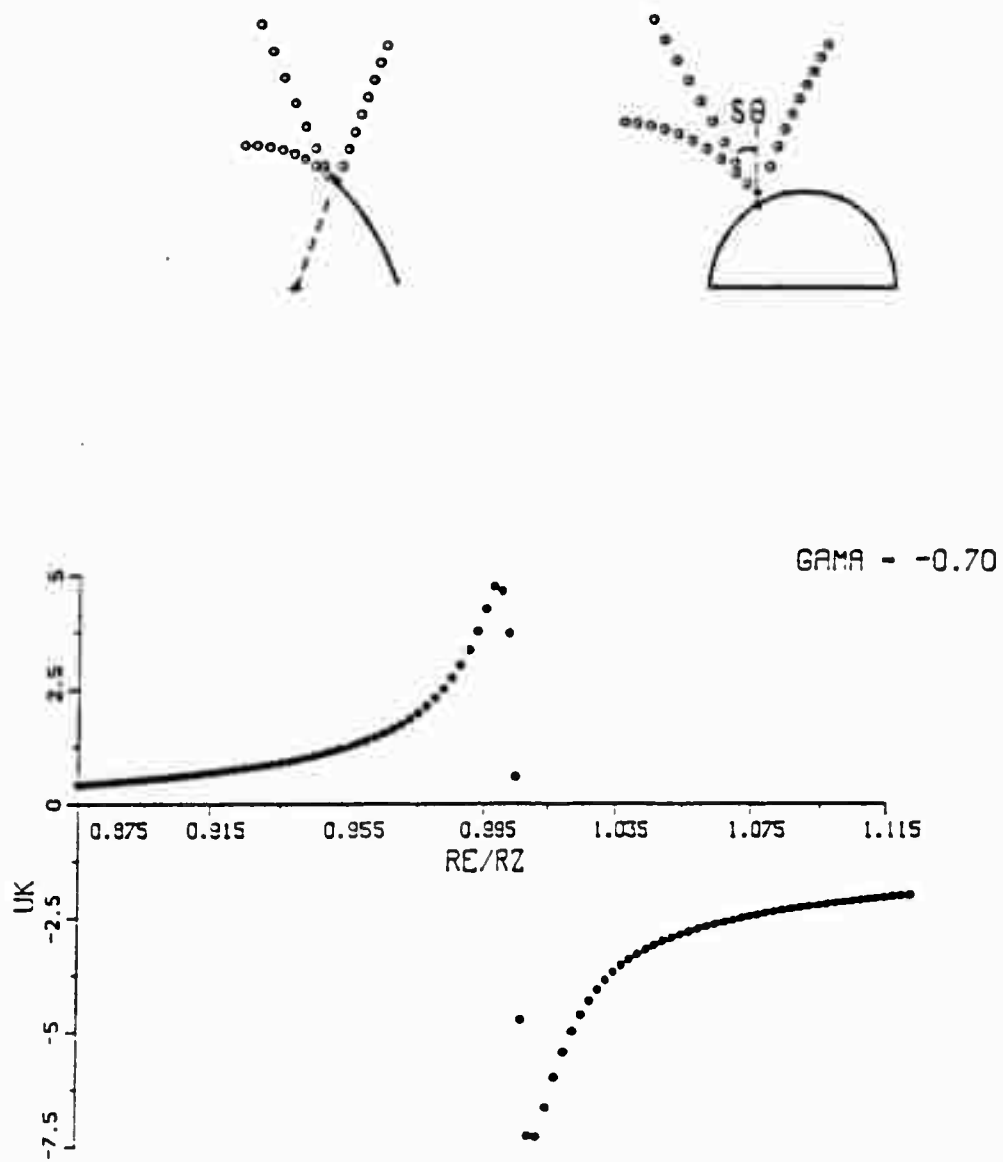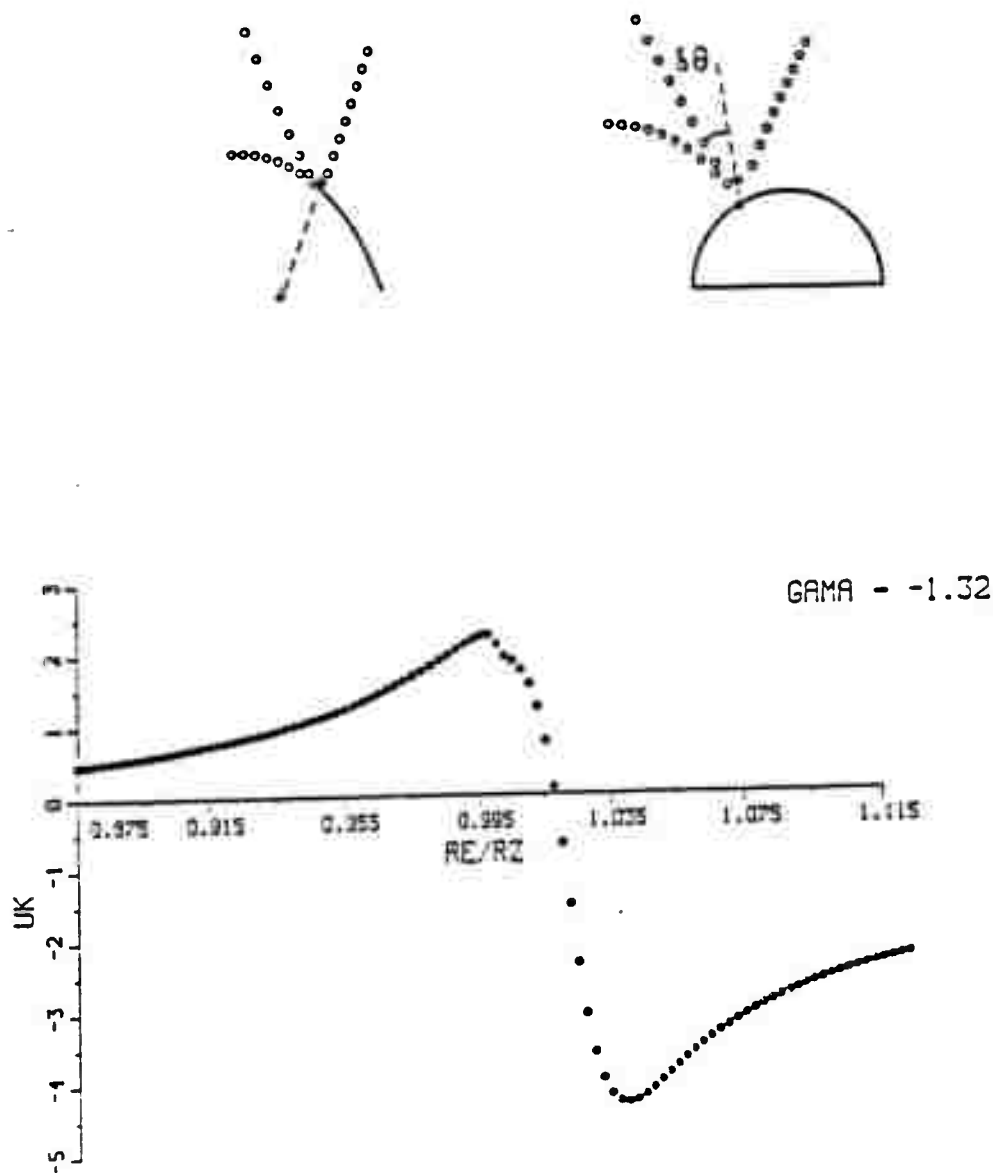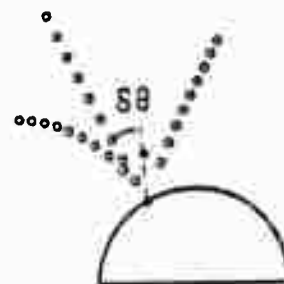Fig. 23 Three-Dimensional Plot of the Tip Velocity

GAMA - -0.70

Fig. 24 Velocity Profile along the Radial Line
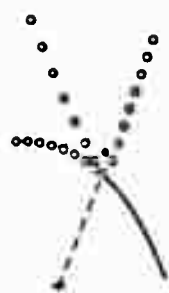(Nascent Vortex at $\varepsilon = 0.05$, $\delta\theta = 25^{\circ}$)

GAMA - -1.32

Fig. 25 Velocity Profile along the Radial Line
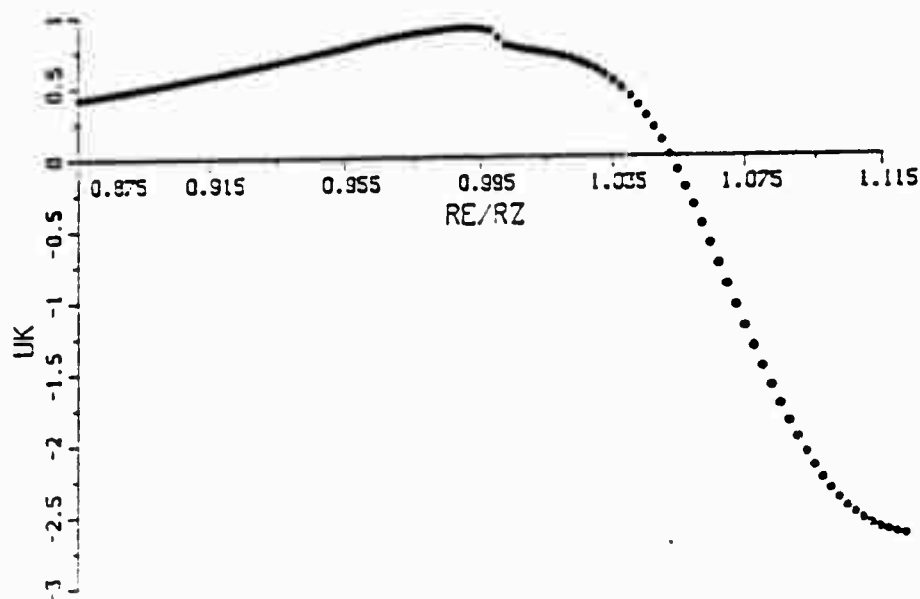(Nascent Vortex at $\epsilon = 0.10$, $\delta\theta = 25°$)

88

Fig. 26 Velocity Profile along the Radial Line
(Nascent Vortex at $\epsilon = 0.20$, $\delta\theta = 25^\circ$)

Figure 21 shows the required vortex strength as a function of the radial distance and θ. Even though these calculations were carried out with a single vortex, the subsequent calculations with large number of vortices have shown that the relationship between the maximum velocity and the tip velocity remains practically invariant if the nascent vortices are always introduced at the fixed point which produces $U(max)/U(tip) = 1$ for the single vortex. The reason for this is that the said velocity ratio is primarily dictated by the nascent vortex. The foregoing analysis led to the conclusion that the nascent vortices should be introduced at $r = 1.0925$ and $\theta = \theta_0 \pm 2.28°$, for the case of the 120-degree camber. To be more precise, the two nascent vortices are placed at the angular positions $\theta_p = \theta_{s1} - 2.28$, and $\theta_q = \theta_{s1} + 2.28$, during the period for which $V_1 - V_2 > 0.2$. For $V_2 > V_1$, the positions of the two nascent vortices switch to their corresponding images with respect to the radial line OM, i.e., they are placed at $\theta_{p1} = \theta_{s1} + 2.28$ and $\theta_{q1} = \theta_{s2} - 2.28$. Similar calculations have been carried out for the 180 deg. and 240 deg. cambers and the appropriate positions of the nascent vortices were found to be $\theta = \theta_0 \pm 2.05$ and $\theta = \theta_0 \pm 1.36$, respectively. Evidently, the nascent vortex position is not materially affected by the camber angle.

90

The evolution of the very early stages of the flow in the immediate vicinity of the tips of the camber is shown in Fig. 27.

In Fig. 27a the velocity field is a consequence of the first two nascent vortices introduced at the points noted above. Figures 27b through 27d show the development of the flow field and the starting tip vortex subsequent to the introduction of the 4th, 8th, and 11th nascent vortex, respectively.

The fact emerging from the foregoing analysis is that the nascent vortices **cannot** be placed arbitrarily (e.g., along the radial line in the circle plane or along the extension of the camber in the physical plane). Otherwise, the velocity distribution in the vicinity of the tip becomes unrealistic and unrepresentative of the evolution of the shear layers on either side of the camber. Furthermore, one is then forced to make arbitrary assumptions regarding the strength and the convection of the nascent vortices.

5.7 Vorticity Flux

There is not a unique procedure for relating the rate at which vorticity is shed into the wake, the Kutta condition, the velocity with which the nascent vortices are convected, and the time interval for the convection
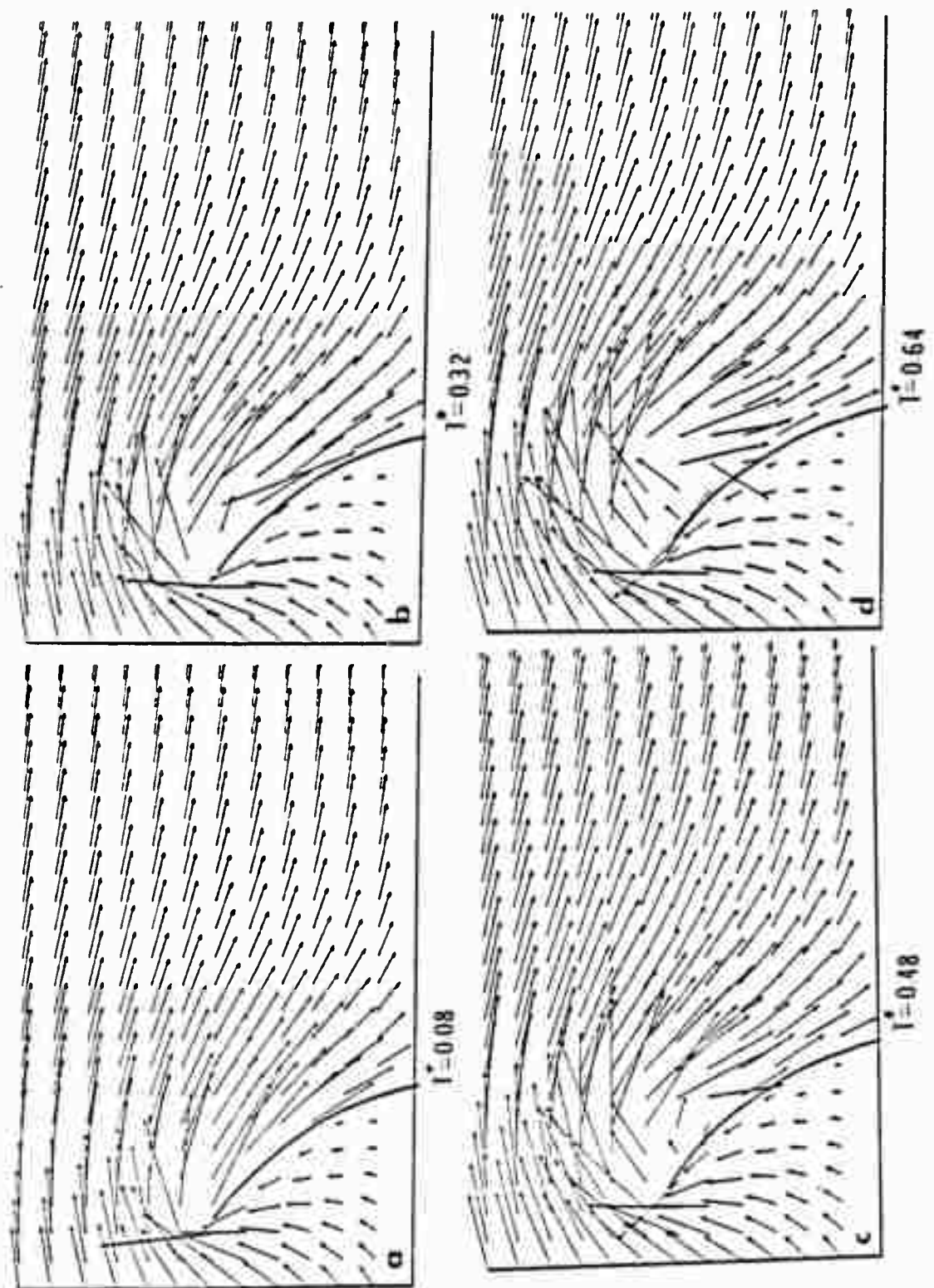
Fig. 27 Velocity Field in the Vicinity of the Tip

which help to reproduce the experimentally observed features of the free shear layers. Fage and Johansen (1928), through quite ingenious experiments with steady flow about various bluff bodies, have shown that vorticity is shed from the two sides of an axisymmetric body (a circular cylinder) or a sharp-edged body (a plate normal to the flow) at the same rate; that the motion in a sheet is steady near the body, except possibly near the inner edge of the shear layers; that fluid flows into a sheet through both edges, but at a greater rate through the outer edge; that at each section of the sheet the velocity rises from a small value to a well-marked maximum value (approximately $V_1/U = 1.45$) and then very slowly decreases to about 1.35 within a distance of approximately $y = 2c$, where the breadth of the sheet reaches a value $\Delta = c$; and finally, that the velocity V_1 at the outer edge of the sheet is much larger than the velocity V_2 at the inner edge (except during the deceleration period of the flow) and V_2 may be ignored in calculating the vorticity flux from $\partial\Gamma/\partial t = 0.5(V_1^2 - V_2^2)$.

In the present calculation the vortex strength, the velocities on either side of the shear layer, and the time interval are related by

$$\Gamma = 0.5 \ (V_1^2 - V_2^2) \ \Delta t \qquad\qquad (37)$$

93

in which Γ is the strength of the nascent vortex, $V_1 = U(\text{tip})$ and V_2 is the velocity at the downstream face of the camber near the tip. The velocity V_2 can be calculated correctly in a number of ways, to be described later. Suffice it to note that in general V_2 is very small (for steady flow) and that the method of its calculation has very little or no influence on the strength of the nascent vertex or on the time interval to be used for a given vortex strength. The velocity V_2 becomes important only when the wake begins to move towards the camber and when the included camber angle is large, i.e., when the regions of secondary separation are substantial as in the case of 180 and 240 degree cambers.

5.8 Computational Details

To explain the computational details of the method let us consider a particular time t after the start of the motion and assume t to be sufficiently large so that there are a number of vortices in the wake. Then the appearance and convection of vortices proceeds as follows, depending on whether a variable or constant time interval is used.

5.8.1 The variable time-interval method

(1)   Determine the strength of the nascent vortices from the Kutta condition [Eq. (20)];

94

(2) Place the nascent vortices at $\zeta_{o,p}$ and $\zeta_{o,q}$ and calculate the velocity V_1 at the two edges of the plate;

(3) Calculate V_2, representing the velocity at the inner boundary of the shear layer, as the integral average of the velocities along the radial line OZ in the physical plane, i.e., from $r = 1$ to $r = 1.1$;

(4) Calculate the time interval, for each edge of the plate, from Eq. (37) using the known values of Γ and the velocities V_1 and V_2. Store the average of the two time intervals for use in the subsequent calculations;

(5) Calculate the velocity induced at the centers of all other vortices;

(6) Convect the two nascent vortices with a velocity $0.5(V_1 + V2)$ for an average time interval Δt (note that the vorticity is convected with the average velocity of the shear layer). If the distance travelled by a nascent vortex is not within 0.05 ± 0.01, it is convected twice for a time interval $\Delta t/2$. The subsequent convections of the nascent vortices are made using the velocity induced at their center.

(7) Convect all other vortices for the same time-interval Δt using a second order scheme given by

$$z(t+\Delta t) = z(t) + 0.5[3\dot{z}(t) - \dot{z}(t-\Delta t)]\Delta t \quad (38)$$

in which $\dot{z} = u + iv$.

(8) Remove the vortices from the calculation whenever they come nearer than 0.05 to the camber in the physical plane (except the first 20 vortices from the tip);

(9) Coalesce vortices with a separation of less than 0.05 (in the physical plane, except the first 20 vortices);

(10) Calculate the tangential velocities and pressures on the inner and outer faces of the camber. Determine the drag and lift forces

95

through the integration of pressure and through the use of the rate of change of impulse. Make plots of suitable variables (e.g., velocity distribution near the tip, variation of nascent vortex circulation with time, evolution of wake, etc.);

(11) Check the flow conditions to determine the state of the calculations:

(a) If $V_1 - V_2 > 0.2$ repeat the foregoing steps;

(b) Stop the introduction of nascent vortices if $0 < V_1 - V_2 < 0.2$ and return to step No. 5;

(c) If $V_2 > V_1$ switch the angular positions of the nascent vortices to their image positions. Calculate V_2 as the integral average of the velocities at the upstream side of the tip of the camber and repeat the foregoing steps; and

(12) Make plots of the variations of various flow parameters (e.g., tip velocity, nascent vortex circulation, evolution of the wake, force coefficients, etc.) and terminate the run.

The foregoing steps are quite general and can be used for any camber, provided that the optimum points of placement of the nascent vortices are incorporated into the calculations.

5.8.2 The Constant Time-Interval Method

In this method the appearance and convection of the vortices are based on the use of variable nascent vortex positions and a constant time interval.

(1) Select a vortex position along the radial line defined by $\theta = 117.72°$ and use $r = 1.1$ as first trial;

96

(2) Calculate the strength of the nascent vortex which satisfies the Kutta condition. This is an exact solution and requires no iteration.

(3) Place the nascent vortex at the corresponding points in the circle and physical planes and calculate the tip velocity.

(4) Calculate a new nascent vortex strength from $0.5(V_1^2 - V_2^2)\Delta t$ where V_1 and V_2 are as defined before.

(5) Compare the newly calculated circulation with that obtained from the Kutta condition. If the difference between the two circulations is less than 0.001 proceed to the next step. If the said difference is larger than 0.001, carry out an iteration on the radial location of the nascent vortex as many times as necessary until the above condition is satisfied. If the circulation calculated from the Kutta condition is larger than that calculated from the tip velocities, the vortex must be moved towards the cylinder and vice versa. Also, each time the direction of the motion of the nascent vortex is changed (inward or outward), the marching distance is halved in order to accelerate the convergence of the two calculations.

(6) Calculate the velocity induced at the center of all other vortices.

(7) Convect the two nascent vortices with a velocity $0.5(V_1 + V_2)$ for a time interval Δt.

(8) Convect all other vortices for the same time interval using a second order scheme given by

$$z(t+\Delta t) = z(t) + 0.5[3\dot{z}(t) - \dot{z}(t-\Delta t)]\Delta t \qquad (38)$$

in which $\dot{z} = u + iv$.

(9) Remove the vortices from the calculation whenever they come nearer than 0.05 to the camber in the physical plane (except the first 20 vortices from the tip).

(10)	Coalesce the same sign vortices with a separation of less than 0.05 (in the physical plane, except the first 20 vortices).

(11)	Calculate the tangential velocities and pressures on the inner and outer faces of the camber. Determine the drag and lift forces through the integration of pressure and through the use of the rate of change of impulse. Make plots, as before, of suitable variables (e.g., velocity distribution near the tip, variation of nascent vortex circulation with time, evolution of the wake, etc.).

(12)	Check the flow conditions to determine the state of the calculations as in step No. 11 in Section 2.8.1.

(13)	Make plots of all the desired variables and terminate the run.

A particular run required about 150 vortices on each side of the camber. Extensive experience with the two versions of the code has shown that a run takes about 1.8 hours on a VAX 2200 and about 3.5 hours on an IBM PC/AT with no Turbo-Jet Accelerator. Furthermore, the constant-time-interval version of the program ran slightly faster than the variable-time-interval version, in spite of the iterations required for the nascent vortex position. Finally, it is important to note that both versions of the code yielded almost exactly identical results for a given camber and velocity history.

6. RESULTS AND COMPARISON WITH EXPERIMENTS

6.1 Model A

The calculations were carried out for two time-dependent normalized velocities. The first of these is given by

$$U/U_c = 1 \quad \text{for} \quad T^* < 8.65 \tag{39a}$$

$$U/U_o = 1 - 0.1539(T^* - 8.65) + 0.00531(T^* - 8.65)^2 \tag{39b}$$
$$\text{for} \quad 8.65 < T^* < 19$$

For this profile (see Fig. 28), the flow begins to decelerate at $T^* = 8.65$ and the velocity of the ambient flow reduces to zero at about $T^* = 19$.

The second velocity profile is given by

$$U/U_o = 1 \quad \text{for} \quad T^* < 9.72 \tag{40a}$$

$$U/U_o = 0.97\ T^* - 0.05\ T^{*2} - 3.70 \tag{40b}$$
$$\text{for} \quad 9.72 < T^* < 11.48$$

$$U/U_o = -0.3423\ T^* + 0.0072\ T^{*2} + 3.82 \tag{40c}$$
$$\text{for} \quad 11.48 < T^* < 17.95$$

For T^* larger than 18, the velocity and acceleration are zero (see Fig. 29).

The velocities and accelerations given above and shown in Figs. 28 and 29 correspond to that encountered
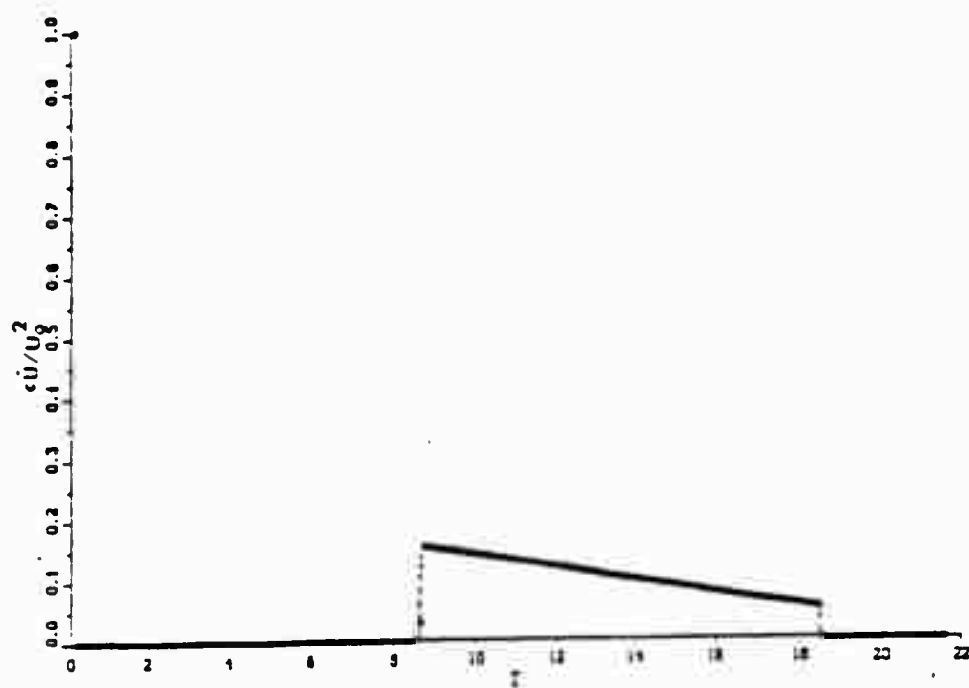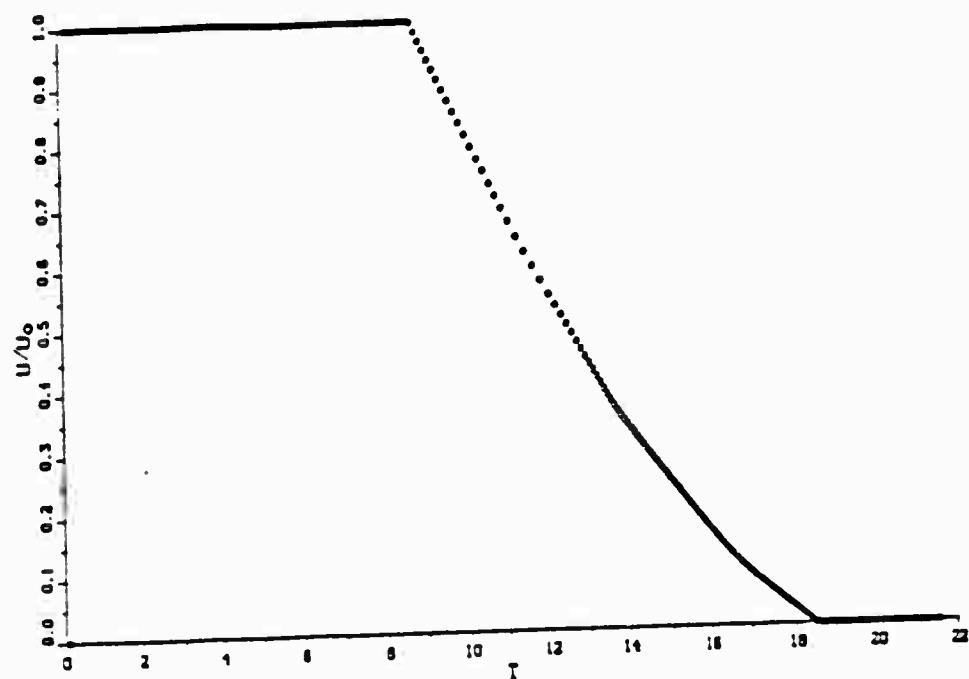
Fig. 28 Variations of the Velocity and Acceleration
(Case No. 1 for the Model A)

100
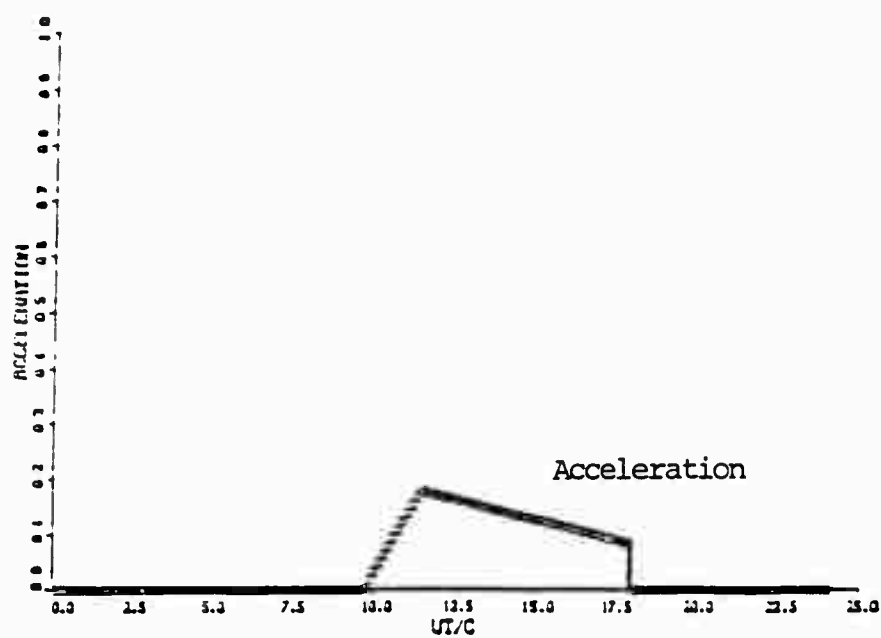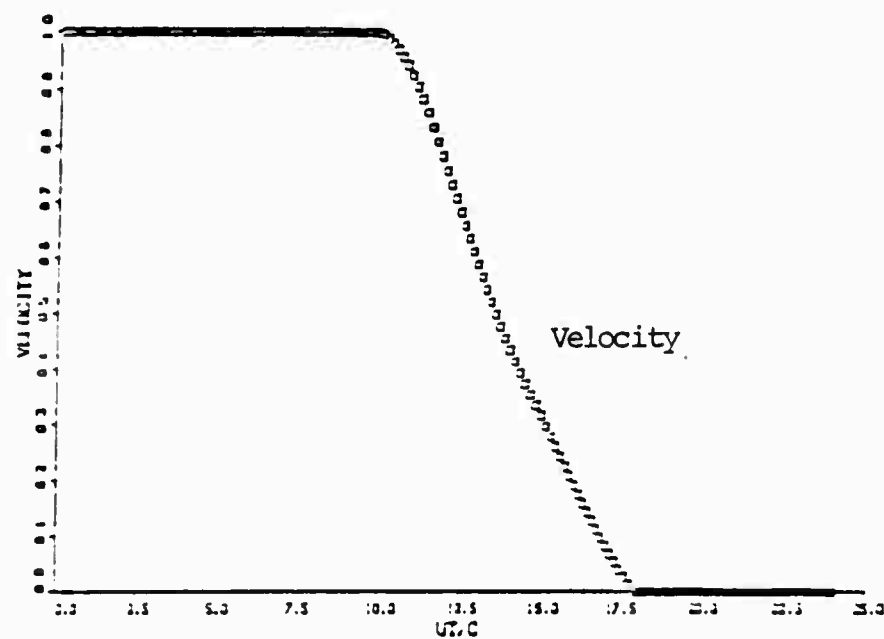
Fig. 29 Variations of the Velocity and Acceleration
(Case No. 2 for the Model A)

in two sets of experiments. Evidently, the calculations can be carried out for any specified variation of the velocity.

The computer program provided, at times specified, the positions of all the vortices, the rate of shedding of vorticity from the tips of the camber, the velocity distribution on the upstream and downstream faces of the camber, the total and differential pressure distributions, and the force coefficients.

Figures 30 through 32 show, at $T^* = 4.35$, the evolution of the wake, the tangential velocities at the upstream and downstream faces of the camber, the velocity profile along the radial line passing through the tip, and the total and differential pressure distributions, obtained through the use of the first ambient velocity history [see Eqs. (39a) and (39b)]. The second ambient velocity history gave very similar results. They will not be reproduced here for sake of brevity.

Figures 30 through 32 and others show that the characteristics of the flow develop symmetrically prior to the onset of deceleration (at $T^* = 8.65$) and the differential pressure is positive everywhere (i.e., the pressure inside the camber is larger than that outside).

Following the onset of deceleration (see e.g., Figs. 33 through 35 at $T^* = 10.84$), the differential pressure

POSITION OF VORTICES

UT/C= 4.35

TANGENTIAL VELOCITY
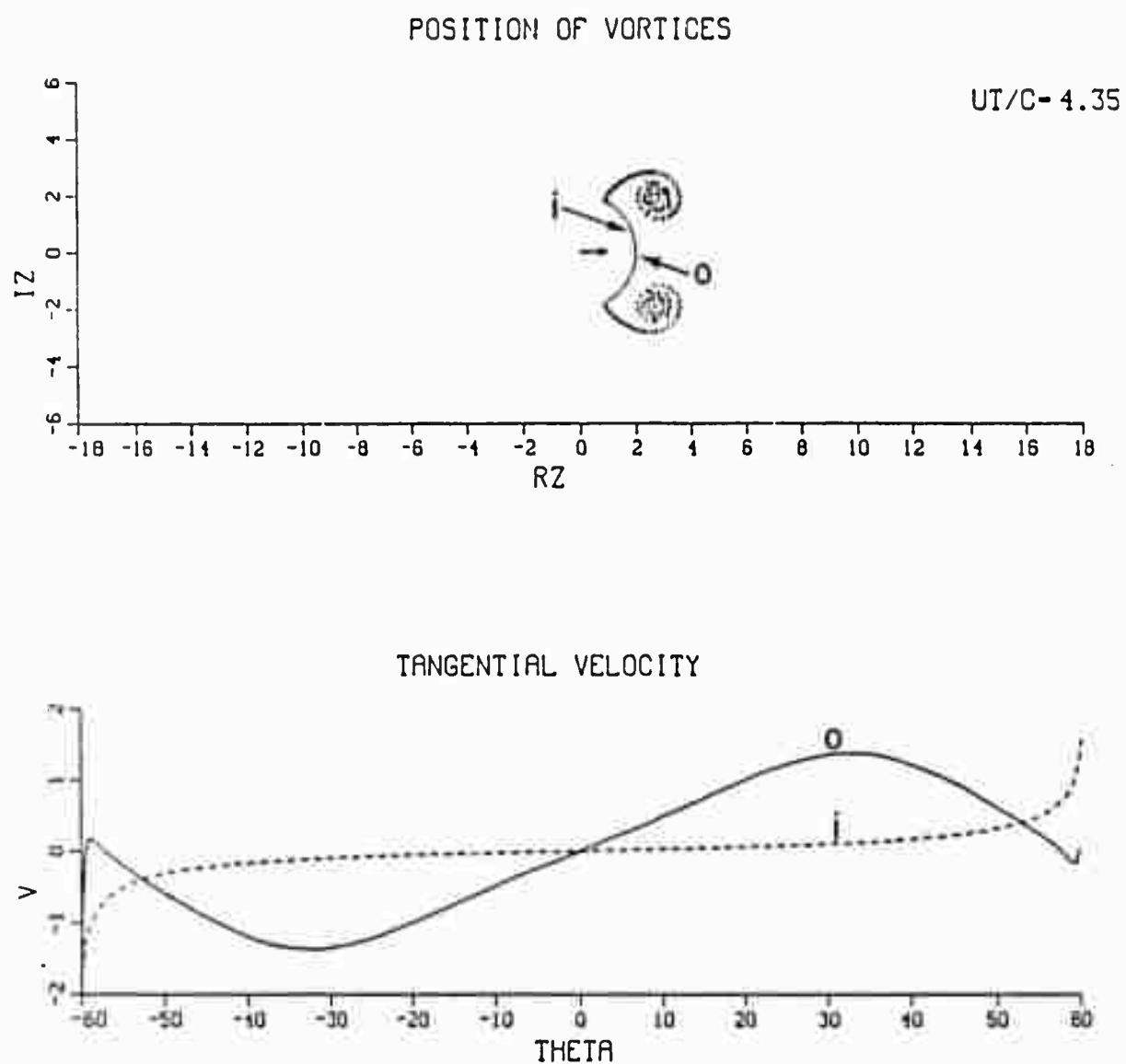
Fig. 30   Position of Vortices and Tangential Velocity Distribution
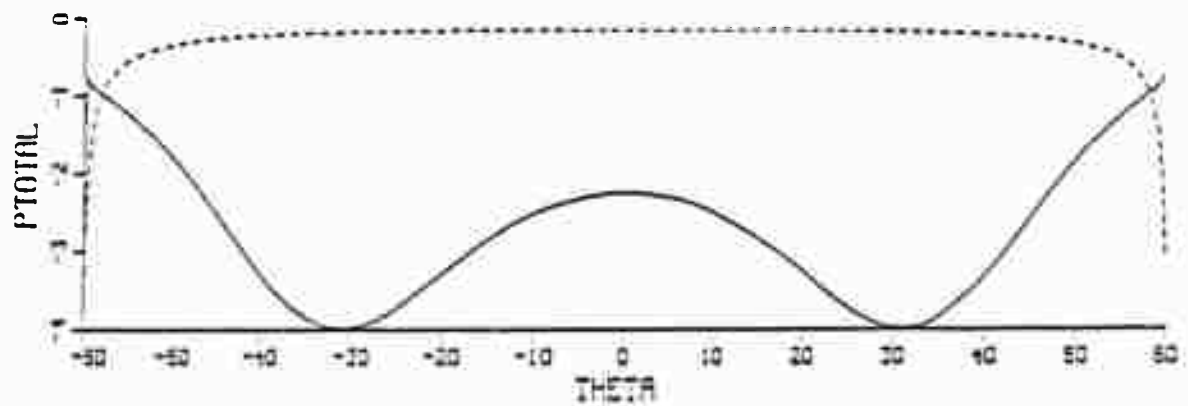
103
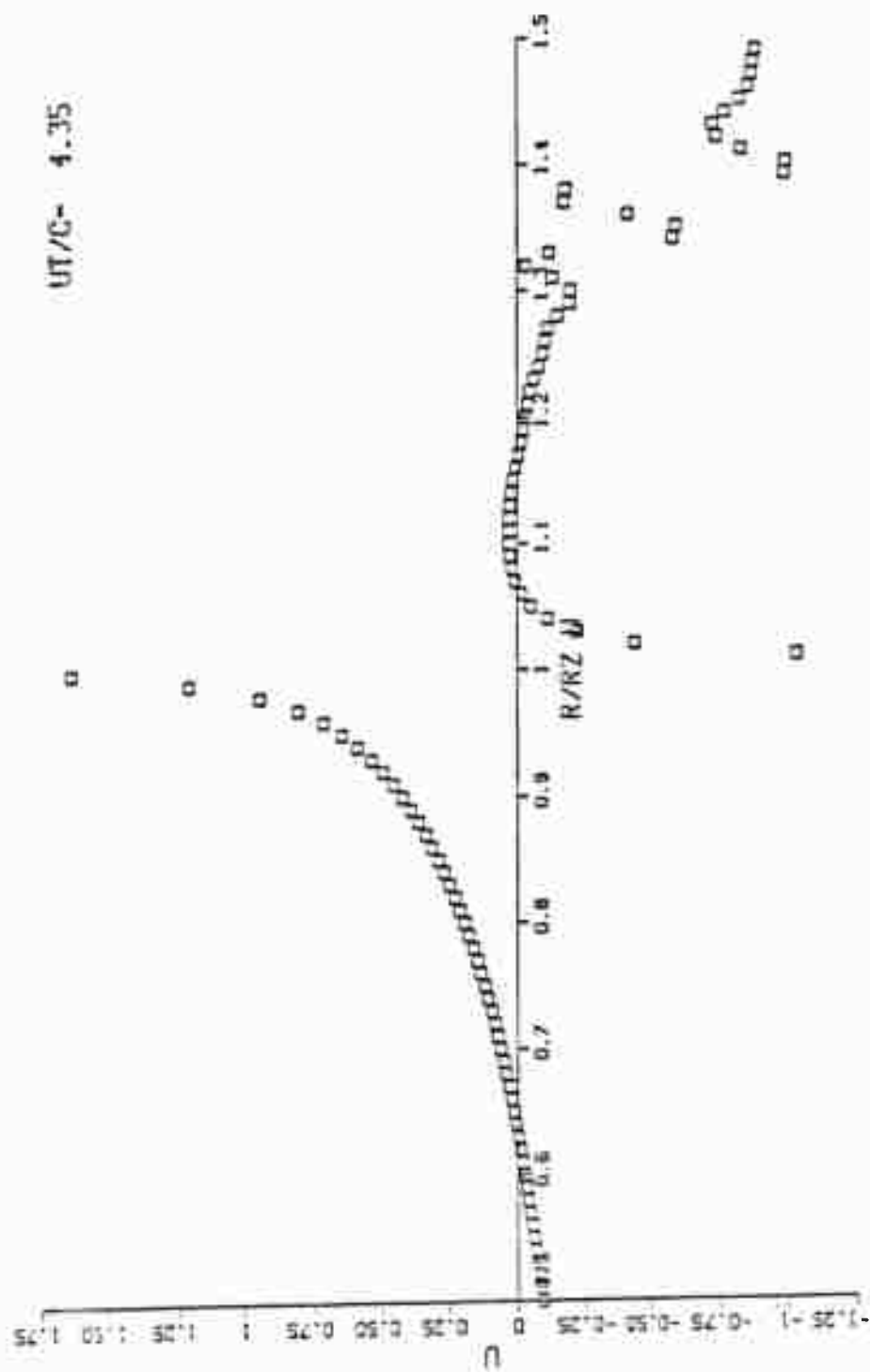
Fig. 31 Velocity Profile along the Radial Line Passing through the Tip
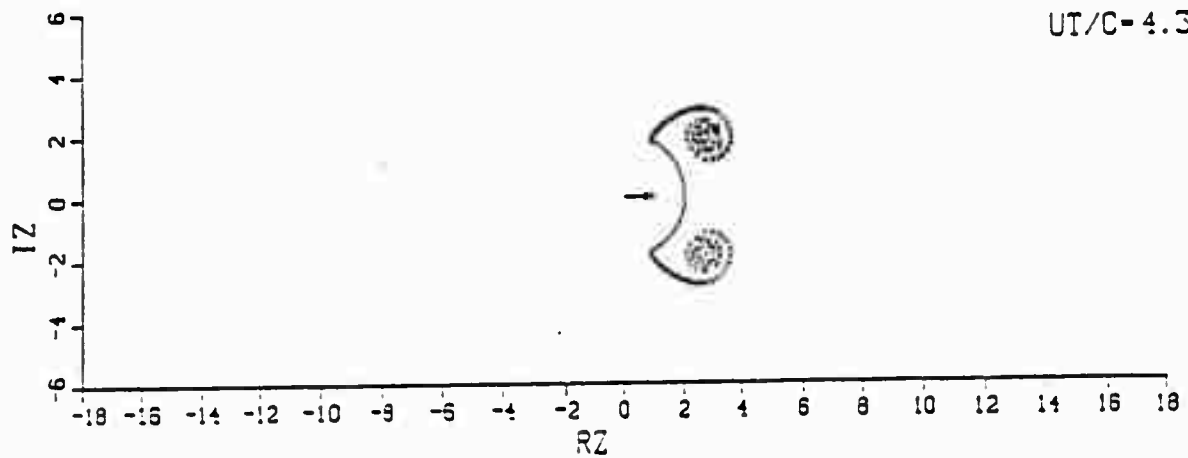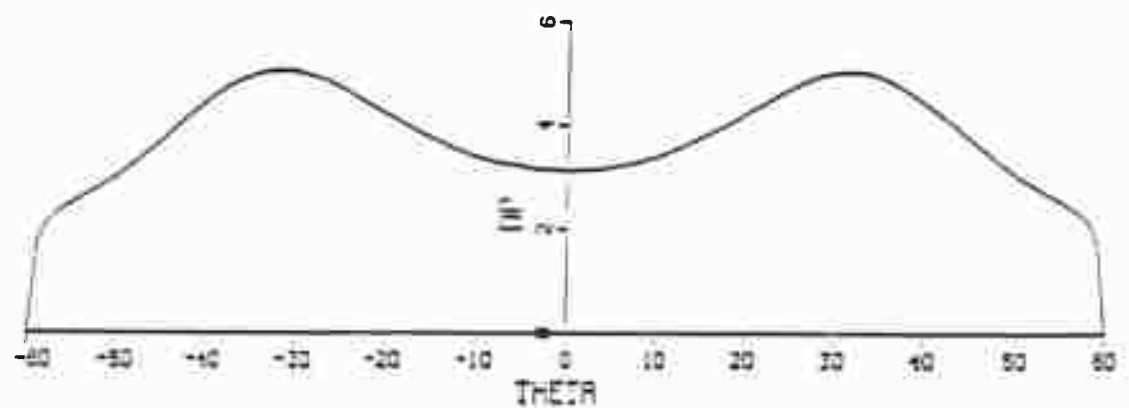
Fig. 32 Pressure Distribution on the Upstream and Downstream Faces

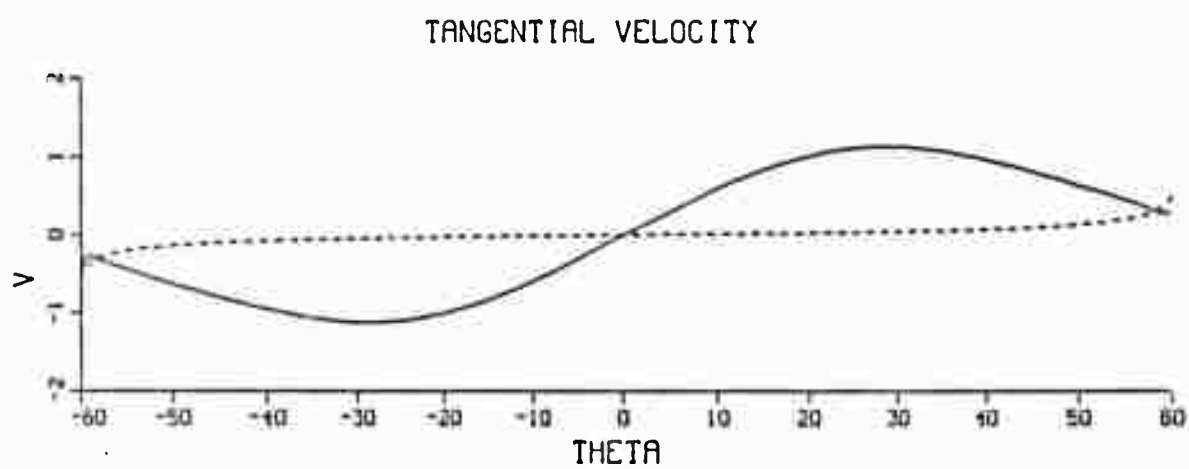POSITION OF VORTICES

UT/C= 10.84

TANGENTIAL VELOCITY
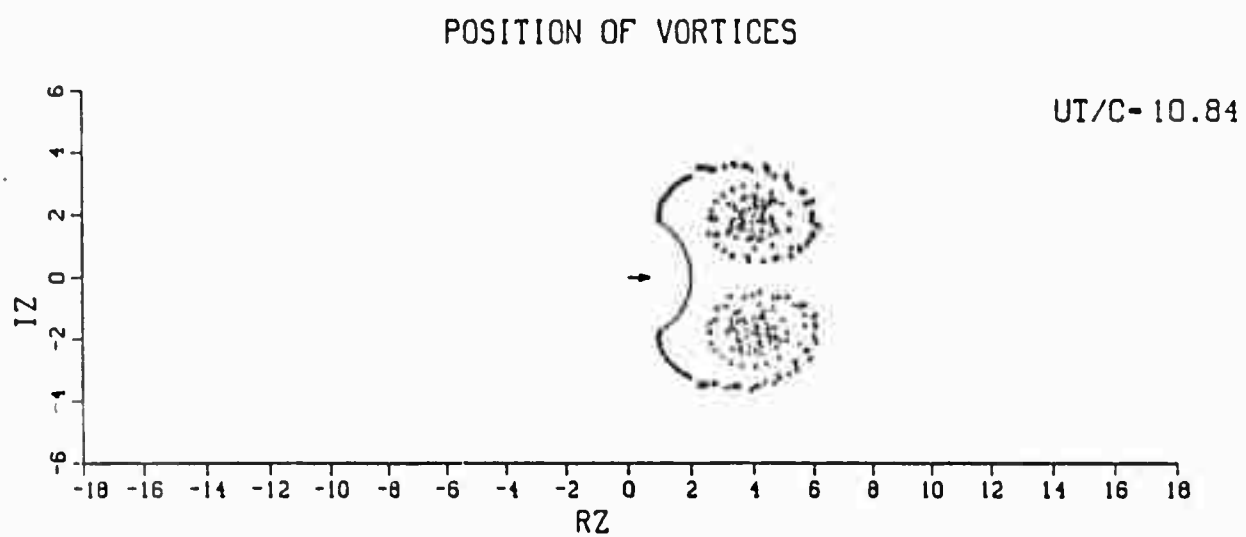
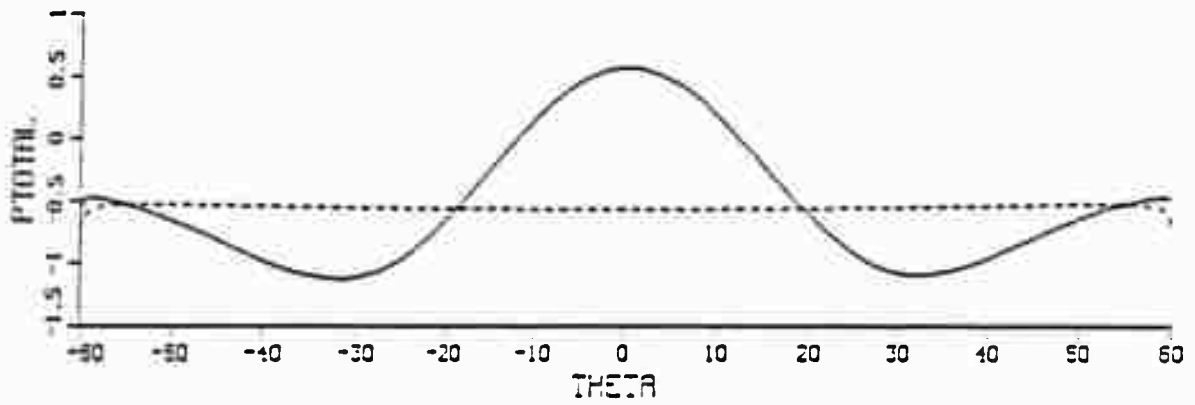Fig. 33 Tangential Velocity at T* = 10.84

106

VELOCITY PROFILE ALONG RZ
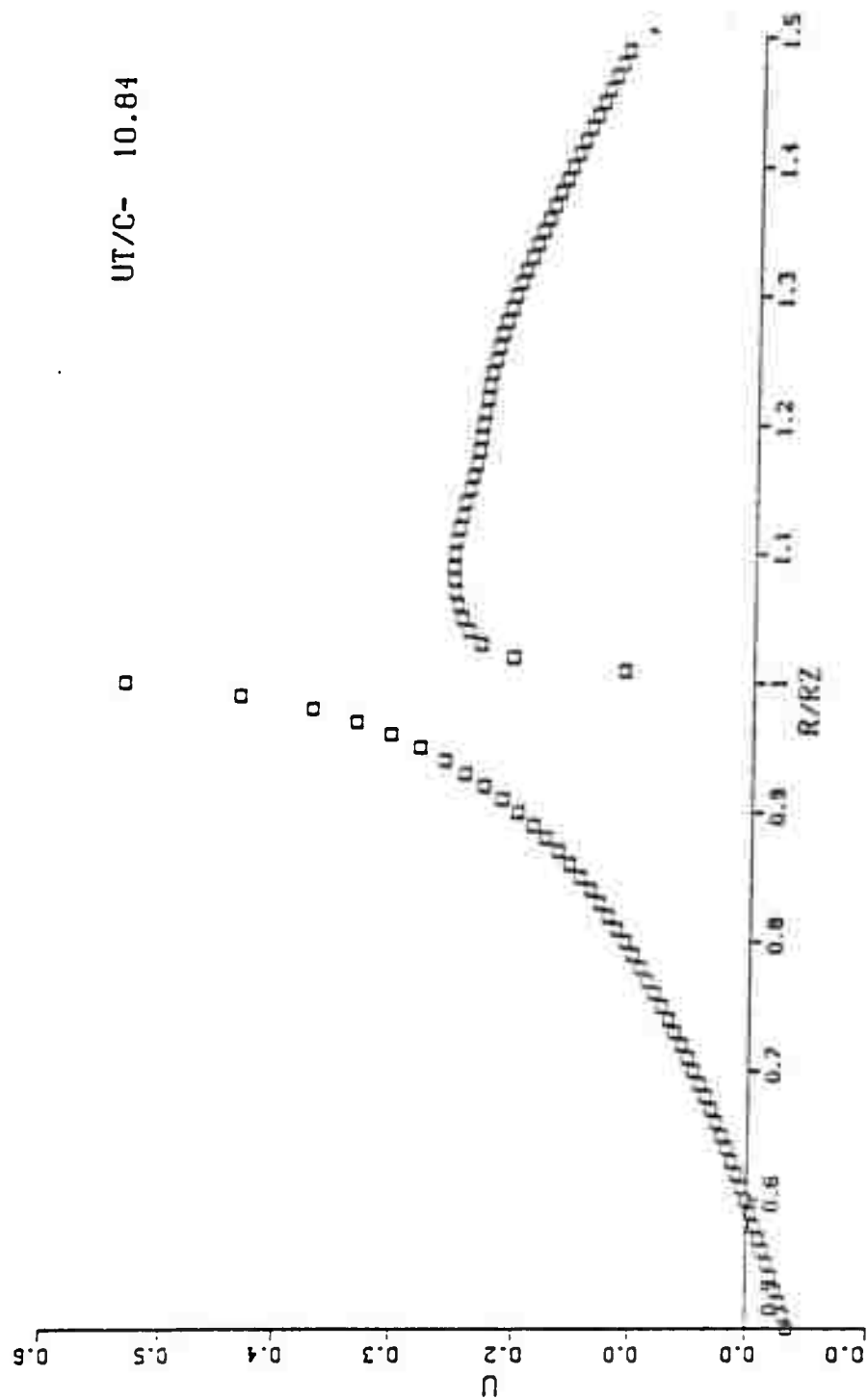
UT/C- 10.84

Fig. 34 Tip Velocity at T* = 10.84

107

POSITION OF VORTICES
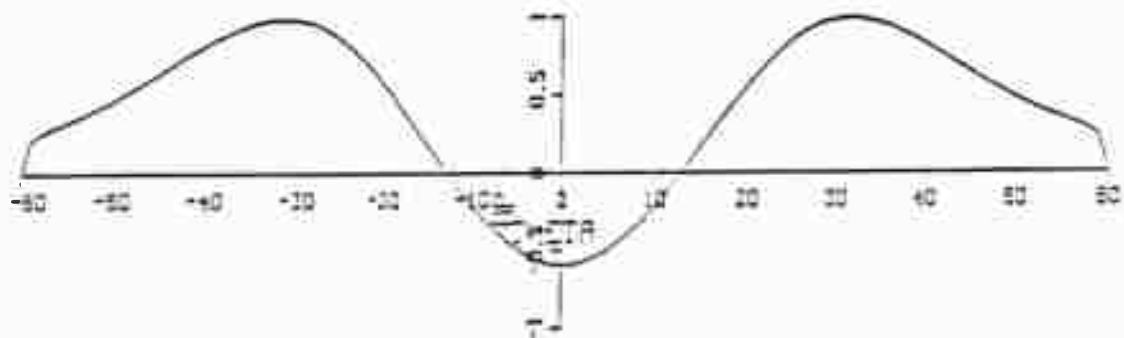

UT/C- 10.84
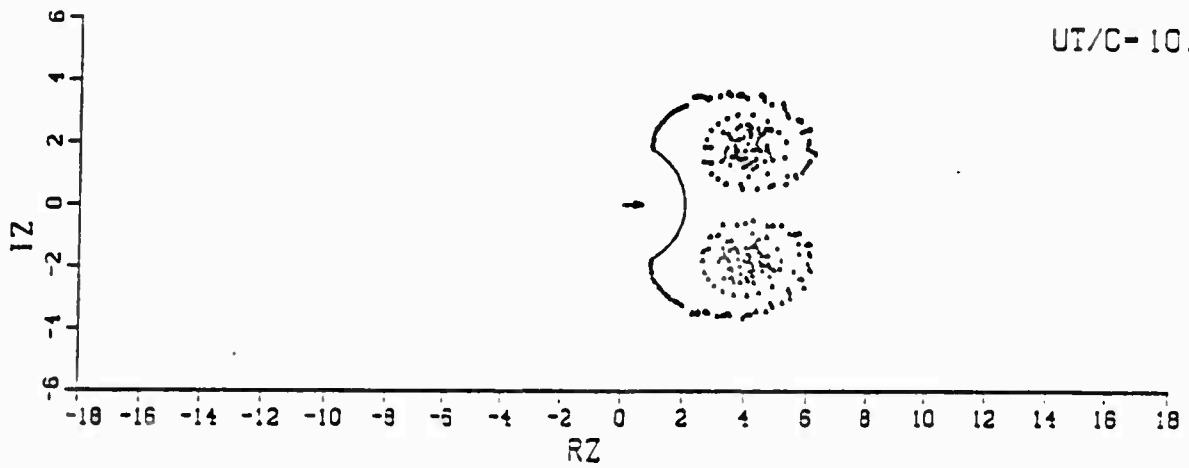
TOTAL PRESSURE

DIFFERENTIAL PRESSURE

Fig. 35   Pressure Distribution at T* = 10.84

108

near the axis of the camber becomes increasingly negative. The reason for this is that the deceleration of the flow brings the vortices closer to the camber. The significance of this result is that had the model been flexible (as in the case of a parachute) the central part of the camber would have collapsed as a result of the particular deceleration it is subjected to. Evidently, the collapse phenomenon would not have remained symmetrical, as evidenced by field experiments with large axisymmetric parachutes.

For T^* larger than about 13 (for the ambient flow under consideration), the velocities induced at the downstream edges of the camber by the large vortices moving towards the camber give rise to oppositely-signed vorticity. This, in turn, leads to the rapid growth of the secondary vortices (see e.g., Figs. 36 through 38 at $T^* = 17.86$). The secondary vortices are relatively weaker than the primary vortices partly because they have been in existence only for a short time and partly because the vorticity flux is not as large as that in the primary shear layers. Consequently, the centroid of the secondary vortices tends to orbit about the centroid of the primary vortices.

A comparison of Figs. 35 and 38 shows that the region of negative differential pressure grows with time
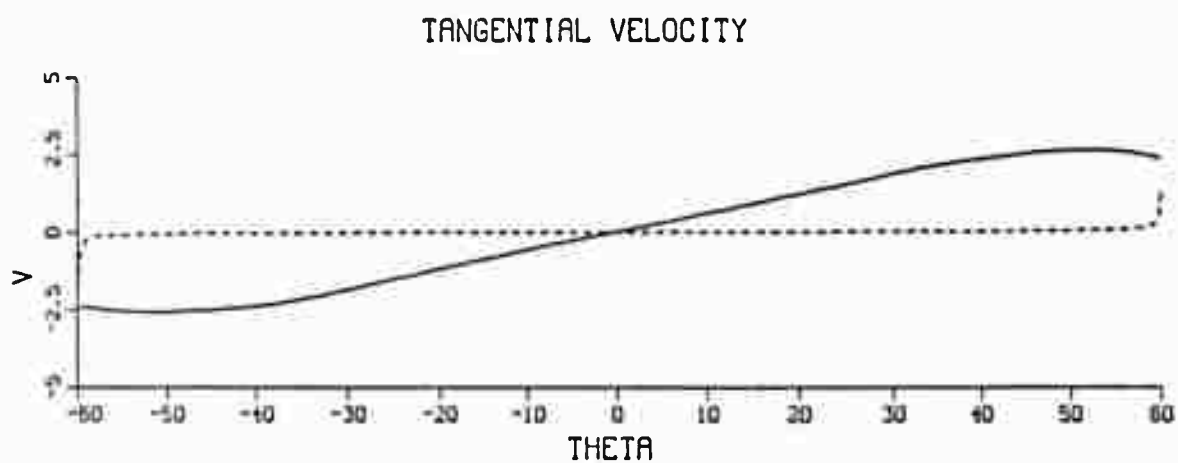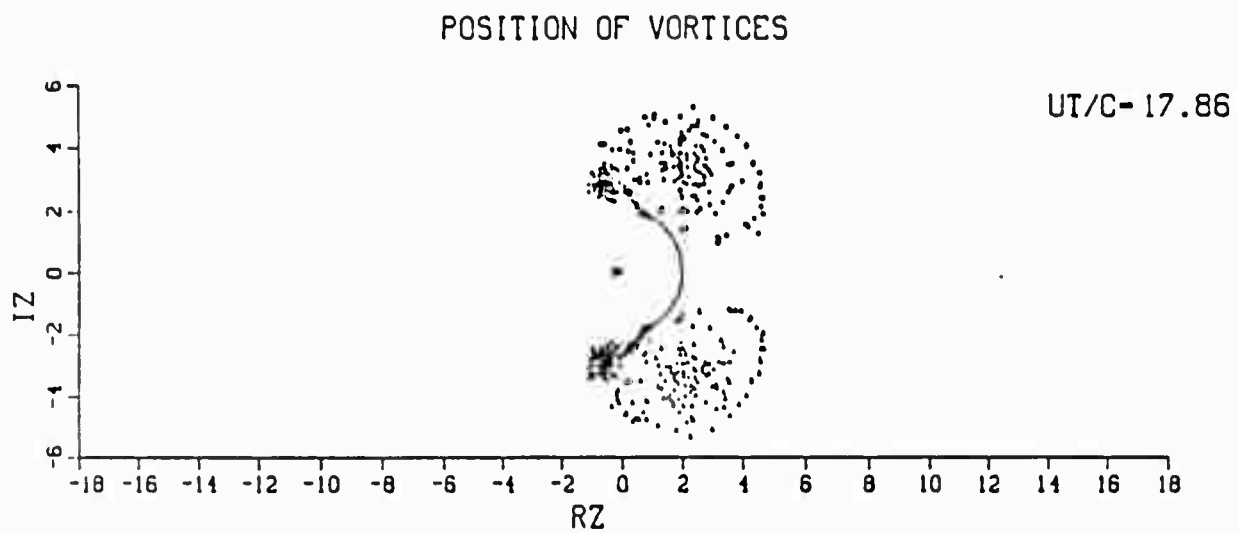
109

POSITION OF VORTICES

UT/C- 17.86

TANGENTIAL VELOCITY

Fig. 36   Tangential Velocity at T* = 17.86
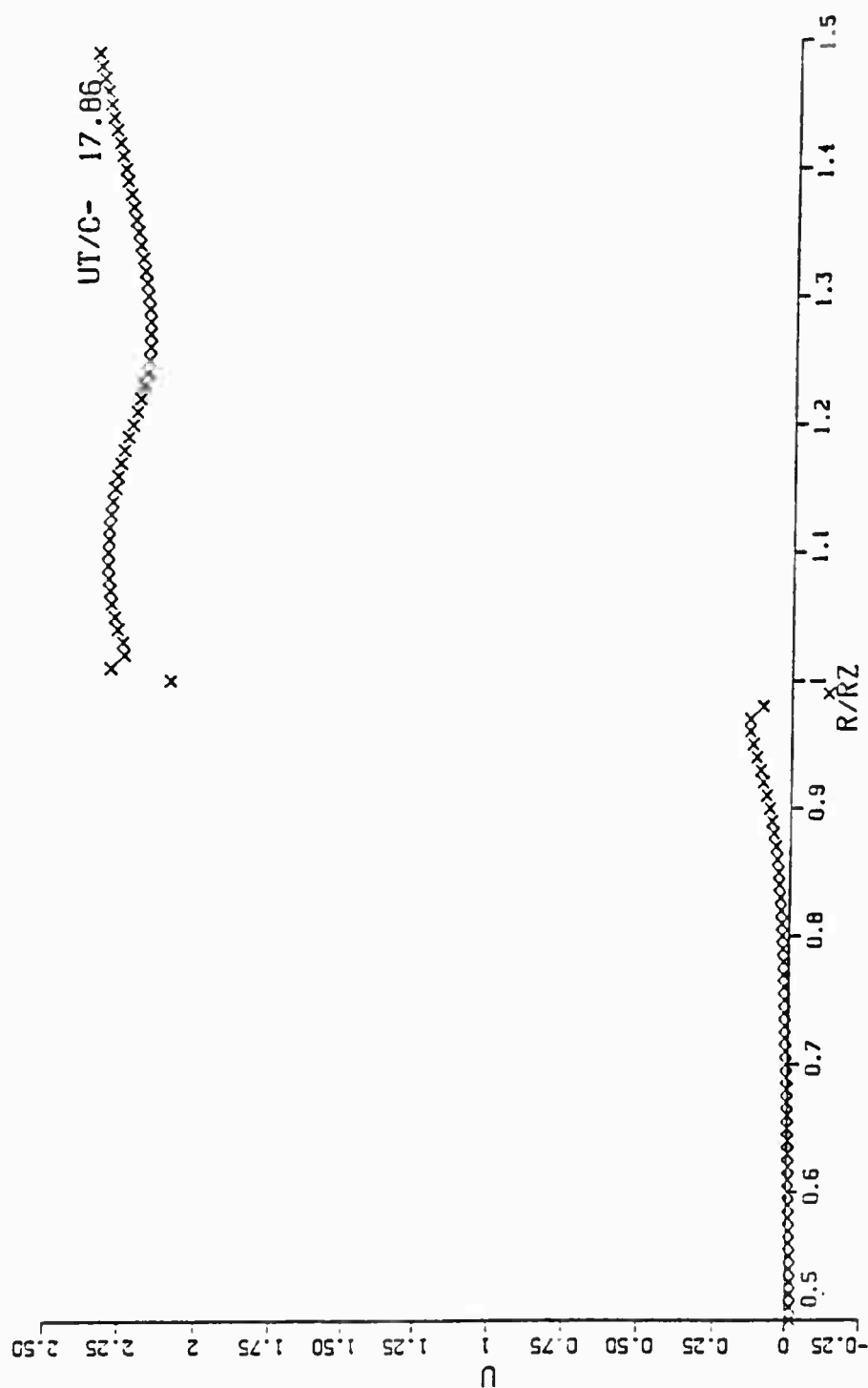
110

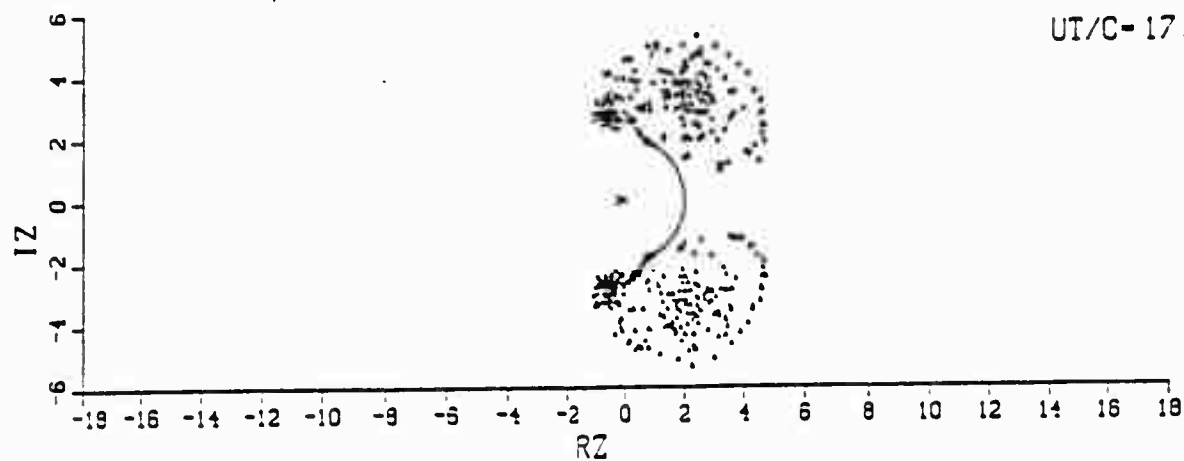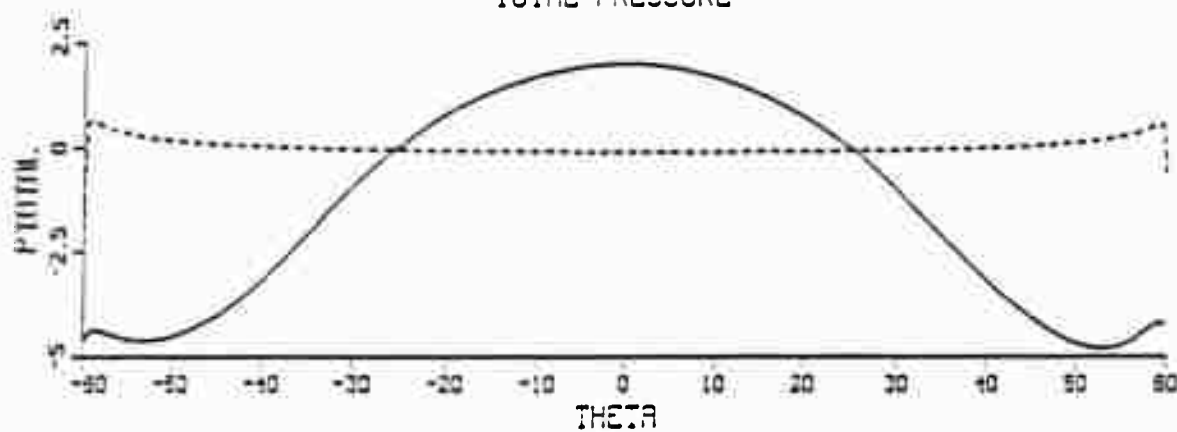VELOCITY PROFILE ALONG RZ

Fig. 37 Tip Velocity at T* = 17.86

111

POSITION OF VORTICES

UT/C= 17.86

TOTAL PRESSURE
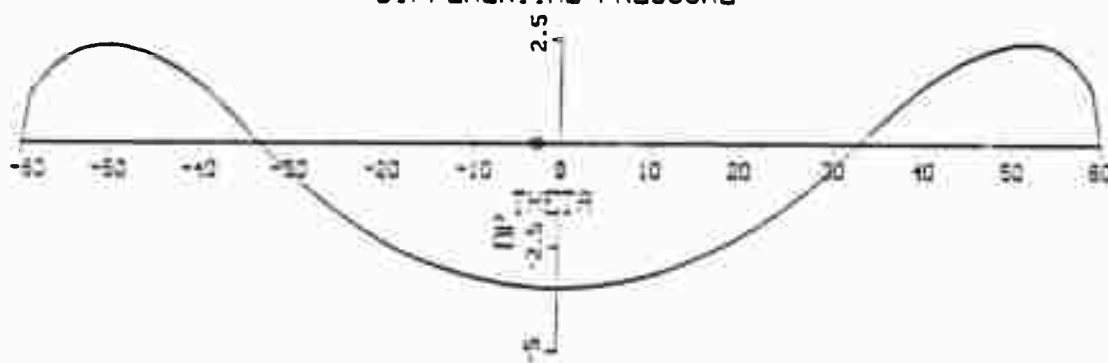

DIFFERENTIAL PRESSURE

Fig. 38 Pressure Distribution at T* = 17.86

112

and occupies a large central portion of the camber. In fact, the drag force acting on the camber becomes negative, as it will be seen shortly.

Figures 39 through 44 show, at suitable times, the velocity field about the camber. The rapid growth of the wake during the period of steady uniform flow is exhibited in Figs. 39 and 40. Figure 41 nearly corresponds to the time at which the deceleration is imposed on the flow. Figures 42 through 44 show clearly the backward motion of the primary vortices and the rapid growth of the secondary vortices. It is seen from Fig. 44 that the fluid motion is entirely due to the motion of the vortices in the flow field. The two vortices on each side of the camber form a counter-rotating couple and remove themselves rapidly from the field under the influence of their mutual induction velocity. Subsequently, the absolute value of the differential pressure begins to decrease. Eventually, the differential pressure reduces to zero everywhere on the camber as the conditions approach to that of a body in a fluid at rest.

Figures 45 and 46 show the velocities V_1 and V_2 as a function of T^*. The tip velocity V_1 decreases from an initially large value of about 3.5 to a nearly constant value of about 1.5 just prior to the onset of
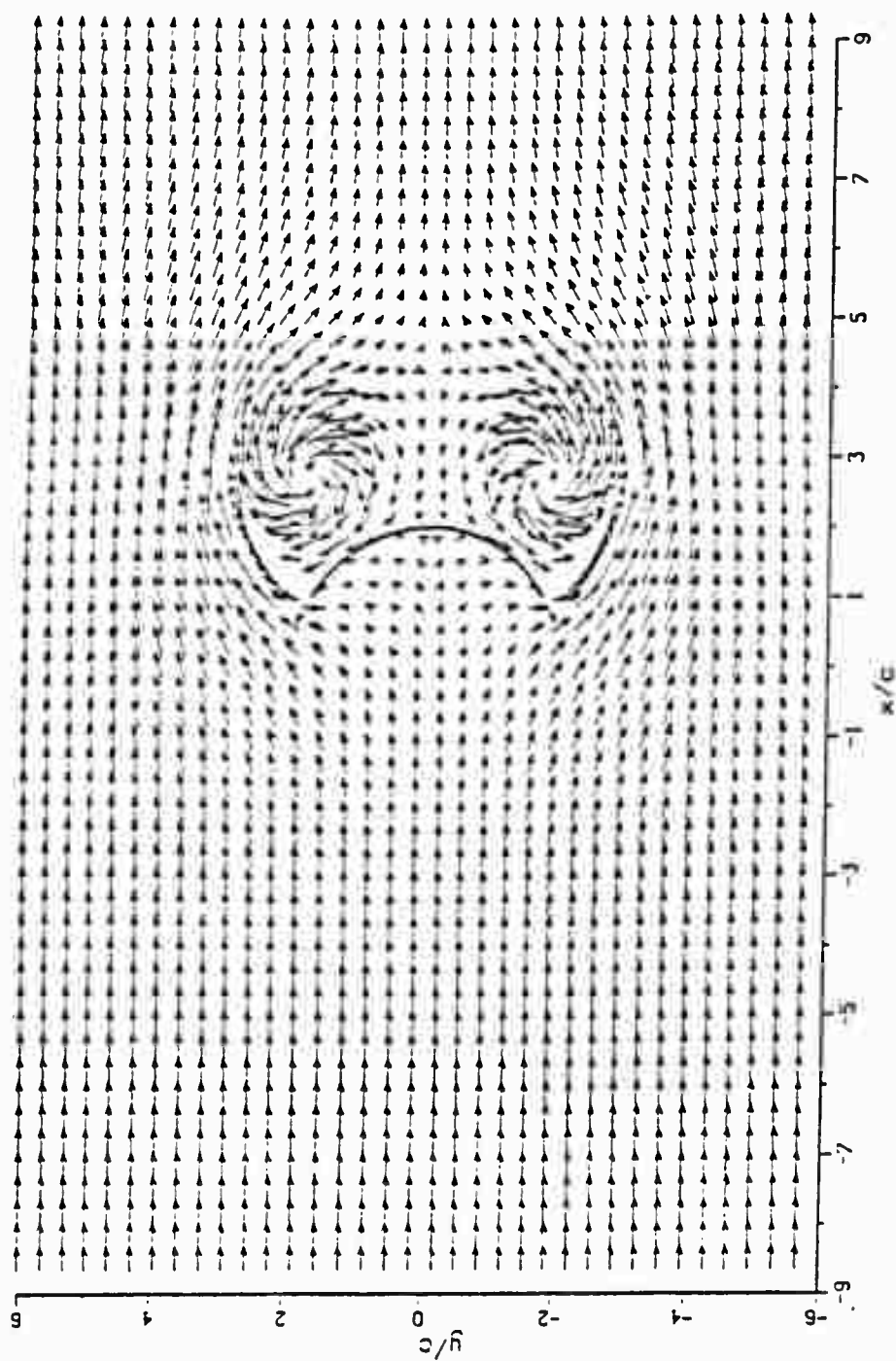
113

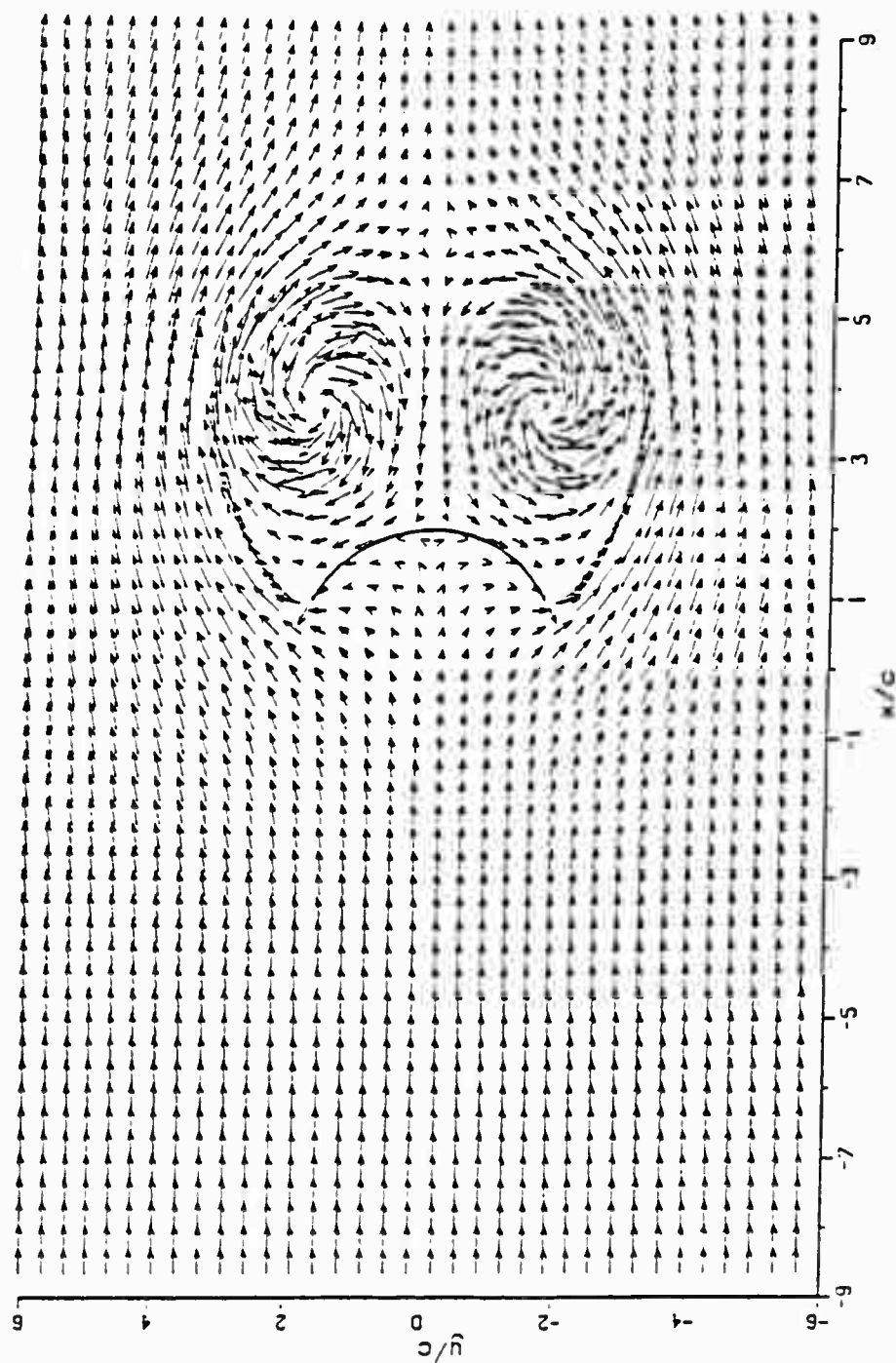Fig. 39 The Velocity Field about the Camber at T* = 4.35

114

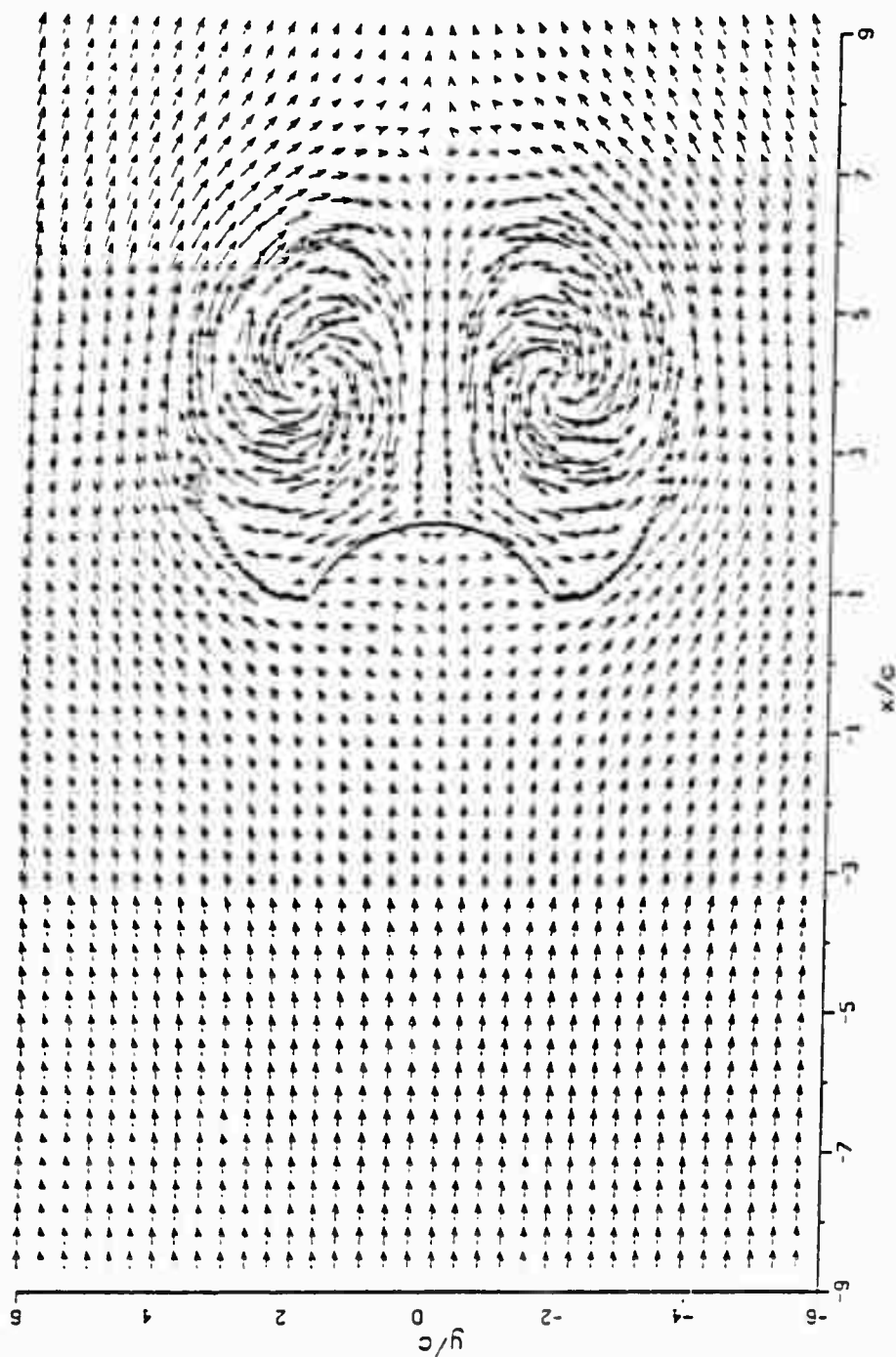Fig. 40   The Velocity Field about the Camber at T* = 6.05

Fig. 41 The Velocity Field about the Camber at T* = 8.55
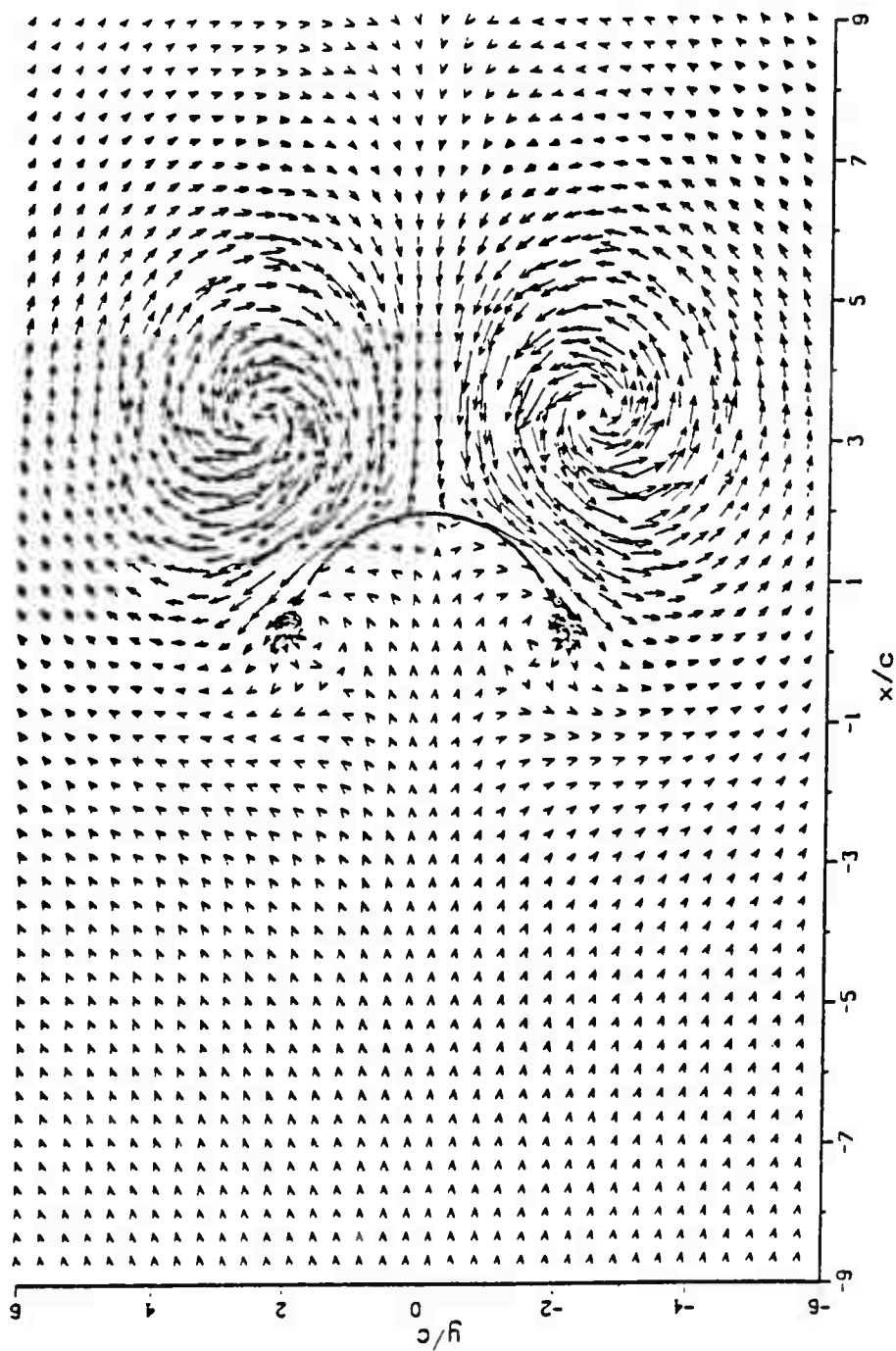
116

Fig. 42   The Velocity Field about the Camber at $T^* = 14.20$
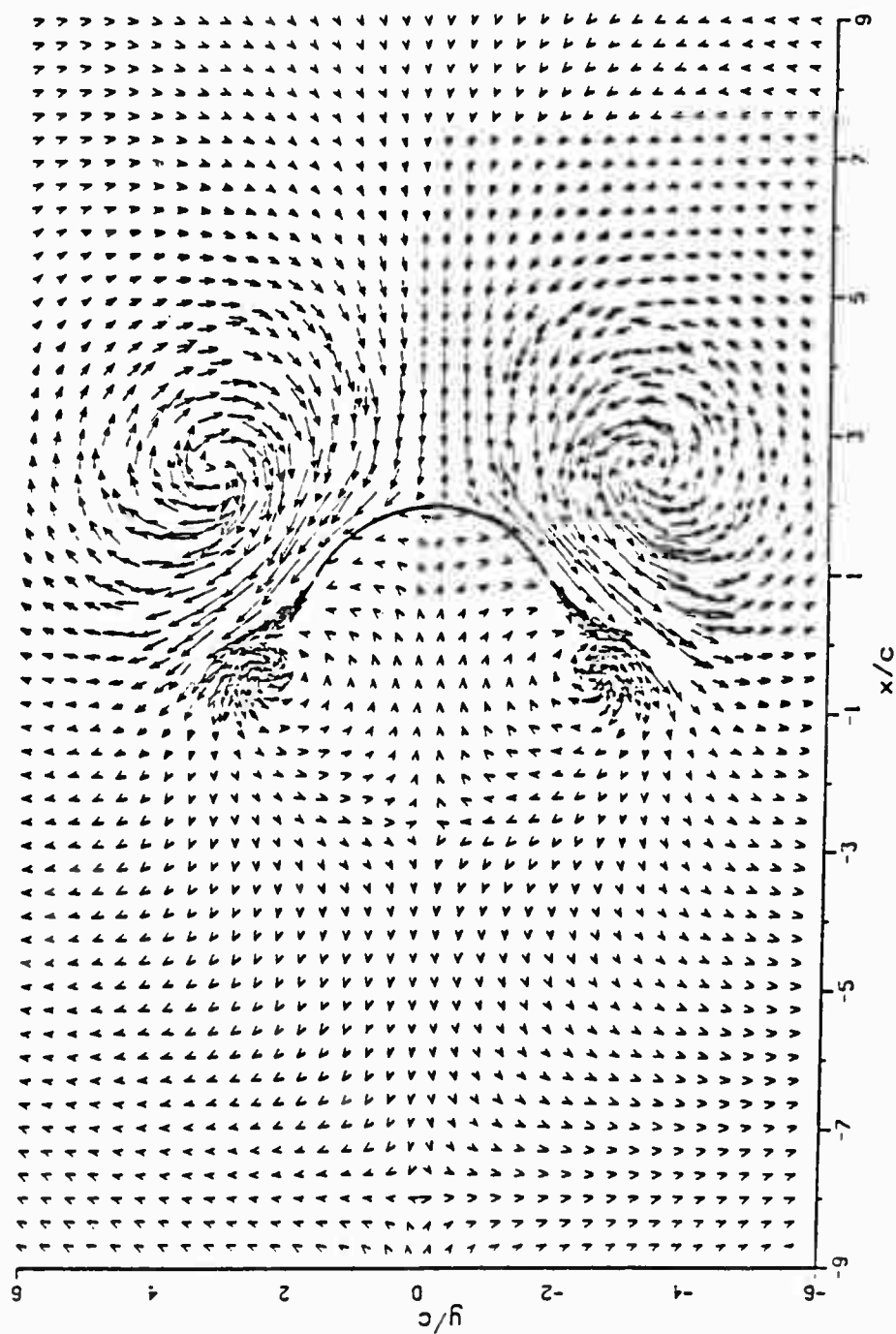
117

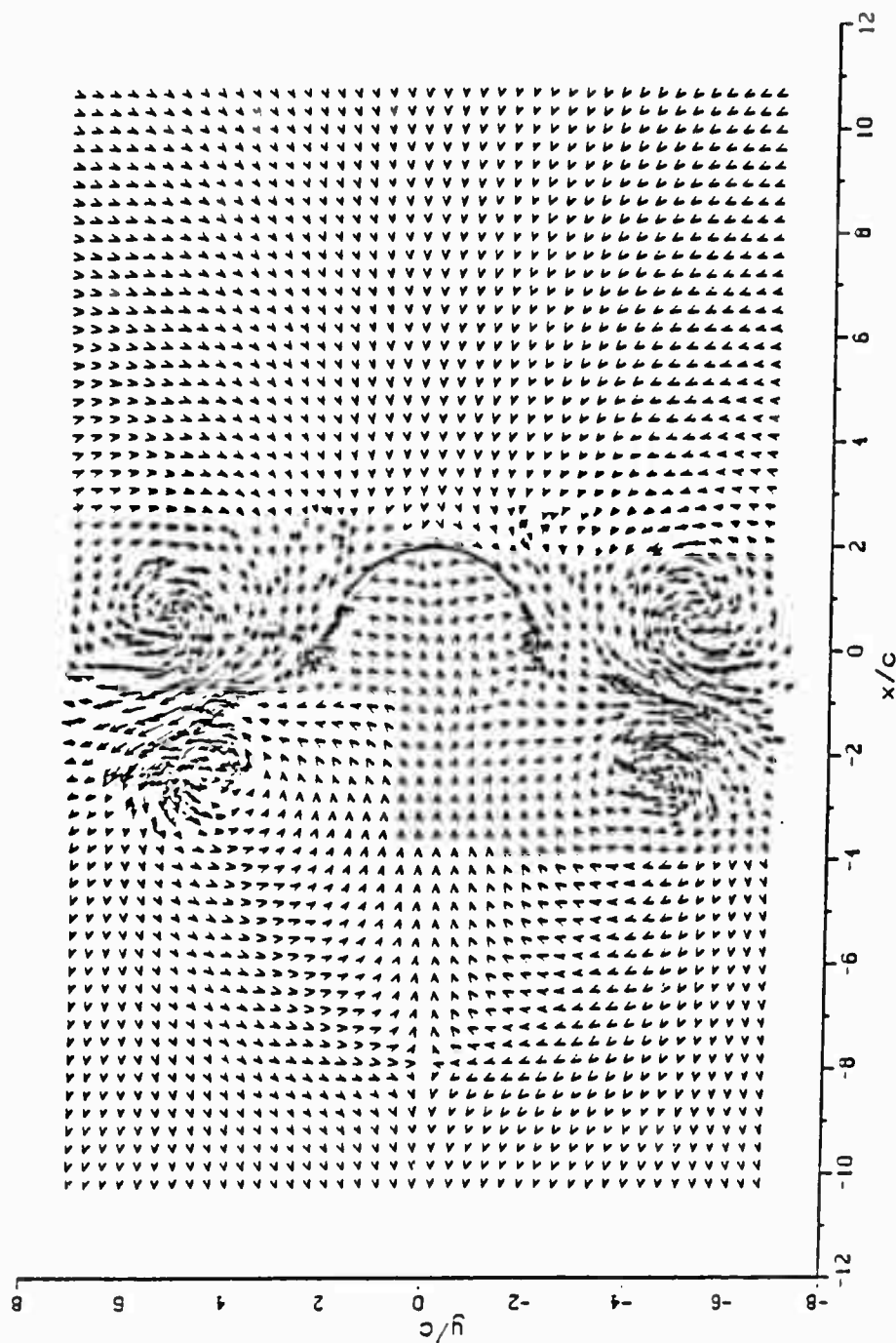Fig. 43   The Velocity Field about the Camber at T* = 16.30

118

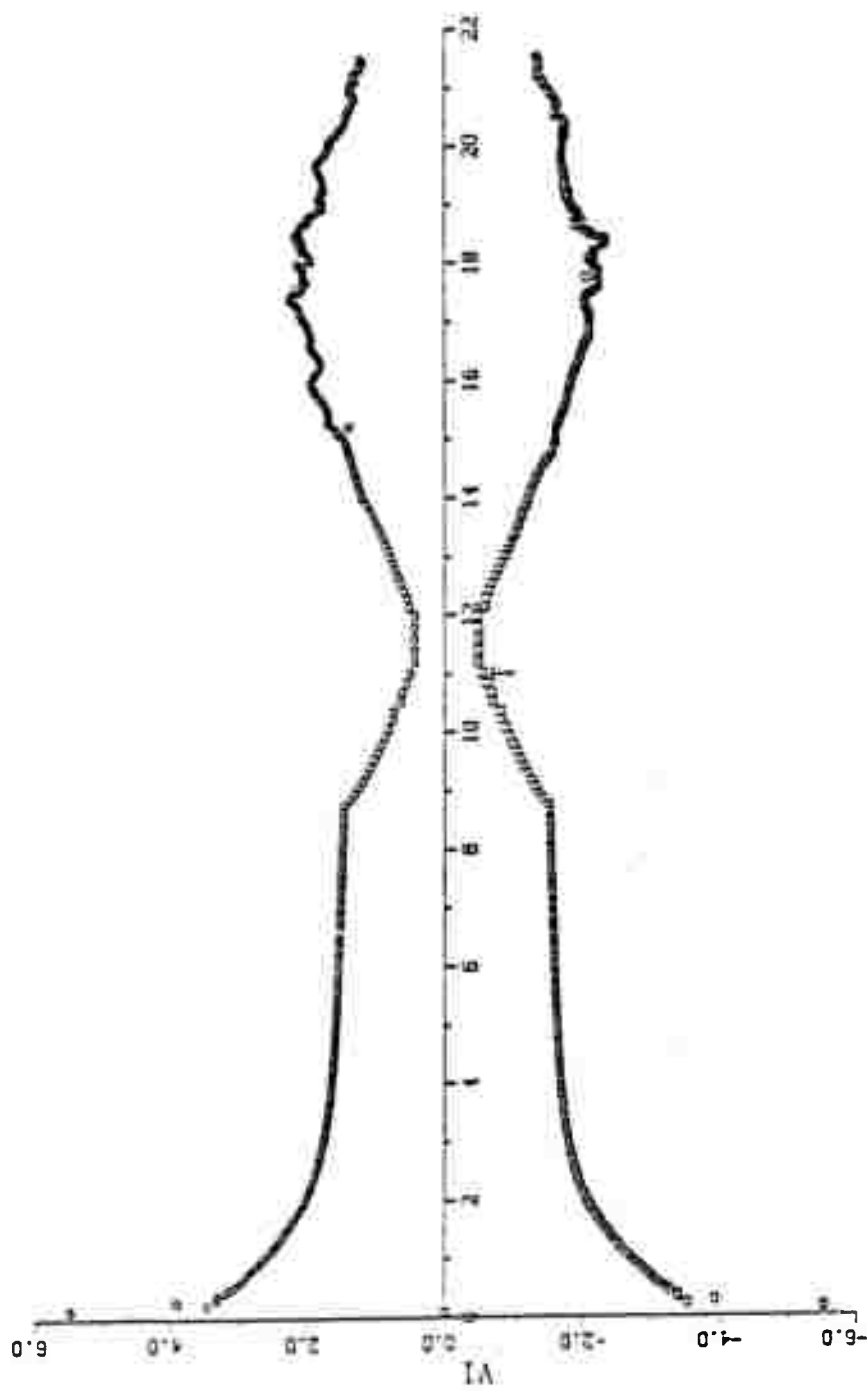Fig. 44 The Velocity Field about the Camber at T* = 21.50
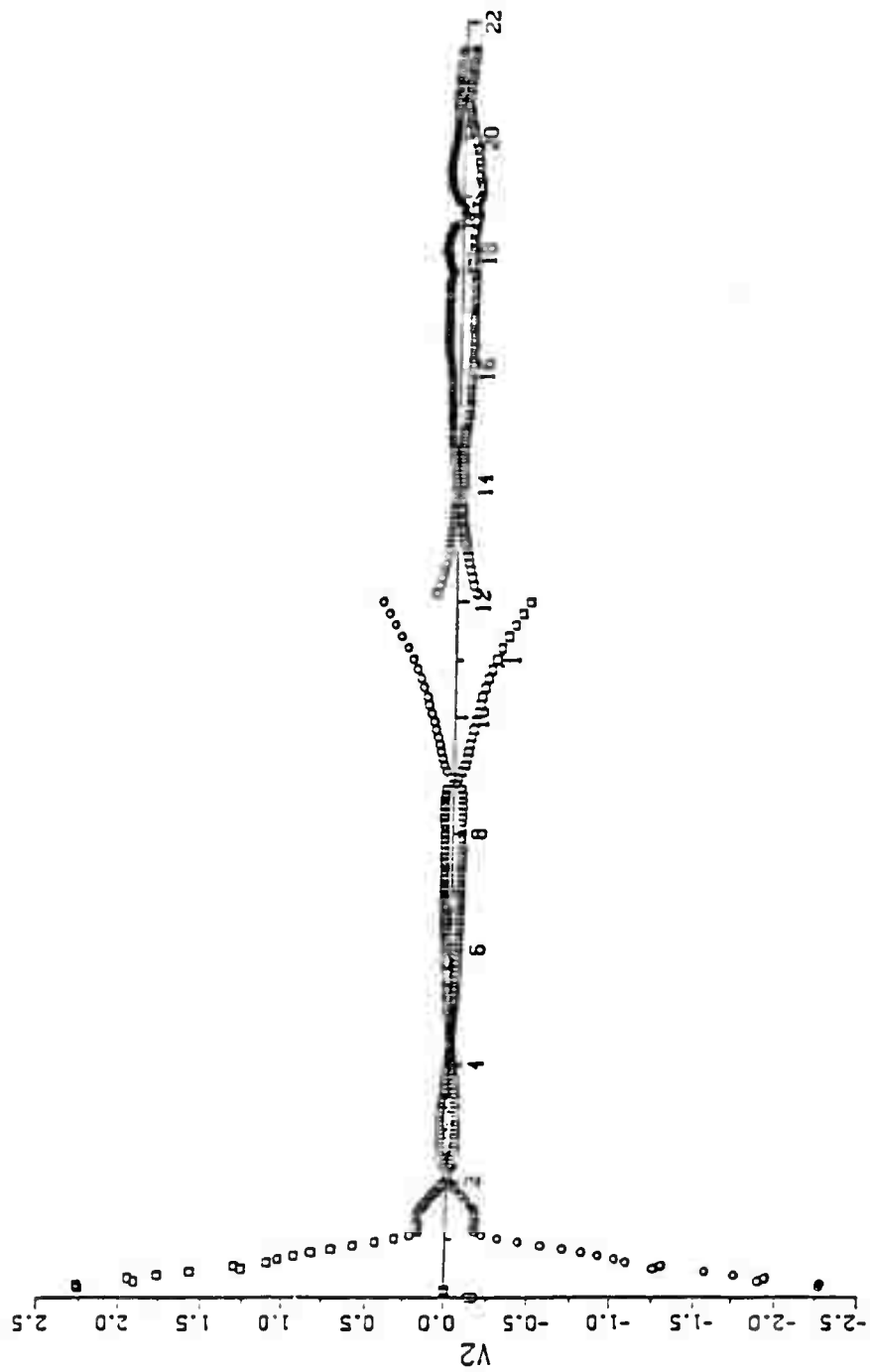
Fig. 45 Variation of V_1 with Time

120

Fig. 46   Variation of V₂ with Time

121

deceleration. Subsequently, V_1 decreases rapidly during the period of deceleration and prior to the inception of the secondary separation. Then V_1 increases to about 2 because of the backward motion of the large vortices near the tips of the camber. Finally, V_1 decreases once again as the primary and secondary vortices move sideways and away from the tips of the camber due to their mutual induction (see Fig. 44).

The variation of V_2 with T* is significant only during two, relatively short, time intervals: at the start of the motion and at the start of deceleration. These are the periods during which the vorticity flux changes rapidly in order to maintain the Kutta condition. During the remainder of time V_2 is negligibly small, as expected on the basis of the pioneering experiments of Fage and Johansen (1928) with steady flow over various types of bluff bodies.

Figures 47 and 48 show the variation of the drag and lift coefficients as a function of time. The former is based on the integration of pressure and the latter on the rate of change of impulse. The drag coefficient calculated through the use of the rate of change of impulse is somewhat larger than that obtained through the integration of the instantaneous differential-pressure distribution. This is due to the fact that the impulse
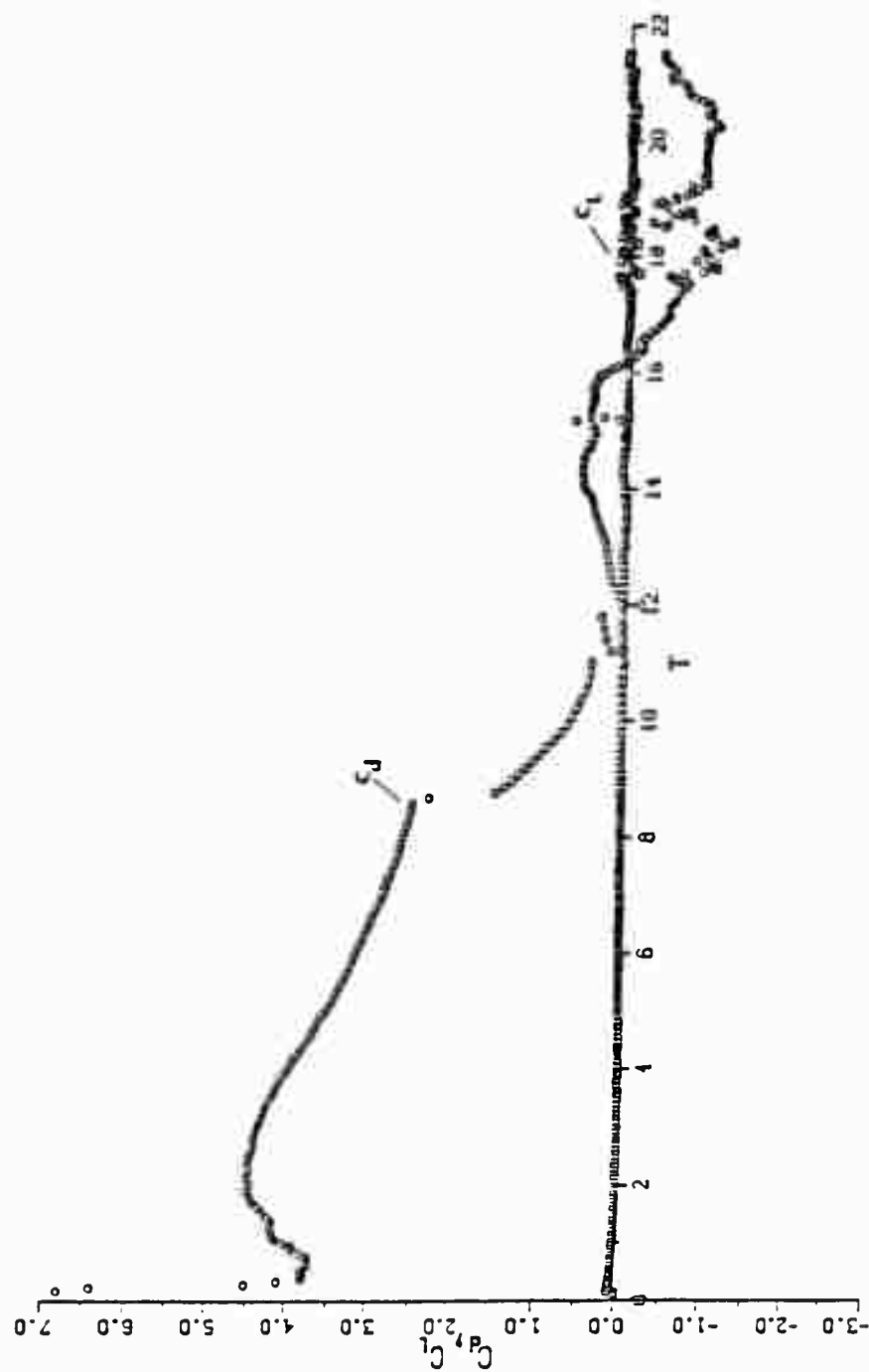
122

Fig. 47 Drag Coefficient Calculated from the Pressure Distribution
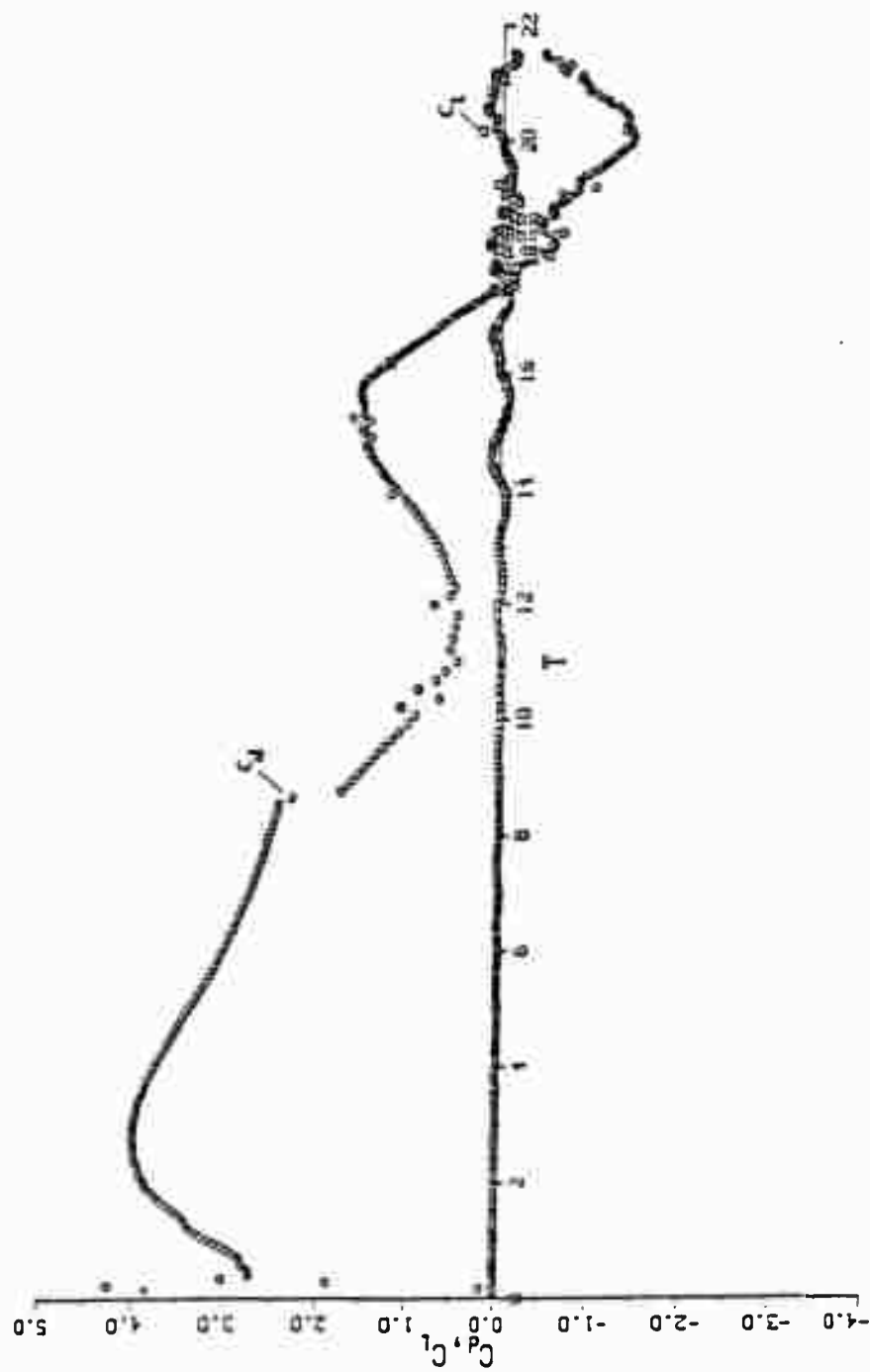(Case No. 1 for the Model)

Fig. 48   Drag Coefficient Calculated from the Rate of Change of Impulse
(Case No. 1 for the Model A)

124

expression includes the rate of change of circulation between two successive time steps whereas the pressure expression does not. It is a well-known fact that in real fluids the memory of the fluid resides in its vorticity. Whereas in inviscid flows there is no memory and the dynamic characteristics of the flow (pressures and forces) are functions of only the instantaneous state of the flow. The analysis presented herein is for an inviscid fluid even though the phenomenon concerns the motion of a real fluid. The question of whether the rate of change of circulation should be included or excluded in the discrete vortex analysis (first discussed by Sarpkaya 1968) is an unsettled issue. It appears that only the comparisons with experiments can clarify the question.

Figure 47 and 48 also show that C_d rises rapidly (due to the rapid accumulation of vorticity in the growing vortices) and begins to decrease as the vortices develop under the influence of a constant ambient velocity. Then the force decreases sharply at the onset of deceleration and goes through zero near the middle of the deceleration period ($T^* = 11$). The force acquires its largest negative value towards the end of the deceleration period. Subsequently, the force gradually decreases to zero.

Also shown in Figs. 47 and 48 is the variation of
the lift force. It is negligible even in the later
stages of the motion. This is primarily due to the fact
that there is not sufficient time for the development of
alternate vortex shedding either during the period of
steady flow or during the period of rapid deceleration.

Figure 49 shows a comparison of the calculated
(through pressure integration) and measured drag
coefficients. In general the agreement between the
calculated and the measured drag coefficient is quite
good. In the time intervals between 13 and 16 and
between 19 and 22, the calculated C_d is somewhat larger.
The primary reasons for this are as follows. In the said
time intervals, the drag coefficient is relatively small
and the viscous and turbulent effects are important in
diffusing the vortices. Furthermore, experiments have
shown (see Section 3.1) that the deceleration period is
accompanied with strong three-dimensional instabilities
in the vortices. Thus, the relatively small drag force
occurring during the deceleration period is an integrated
average of the effects of this three-dimensional
instability on the pressure distribution. This cannot be
taken into consideration in the numerical analysis. It
is possible to bring the calculated and measured values
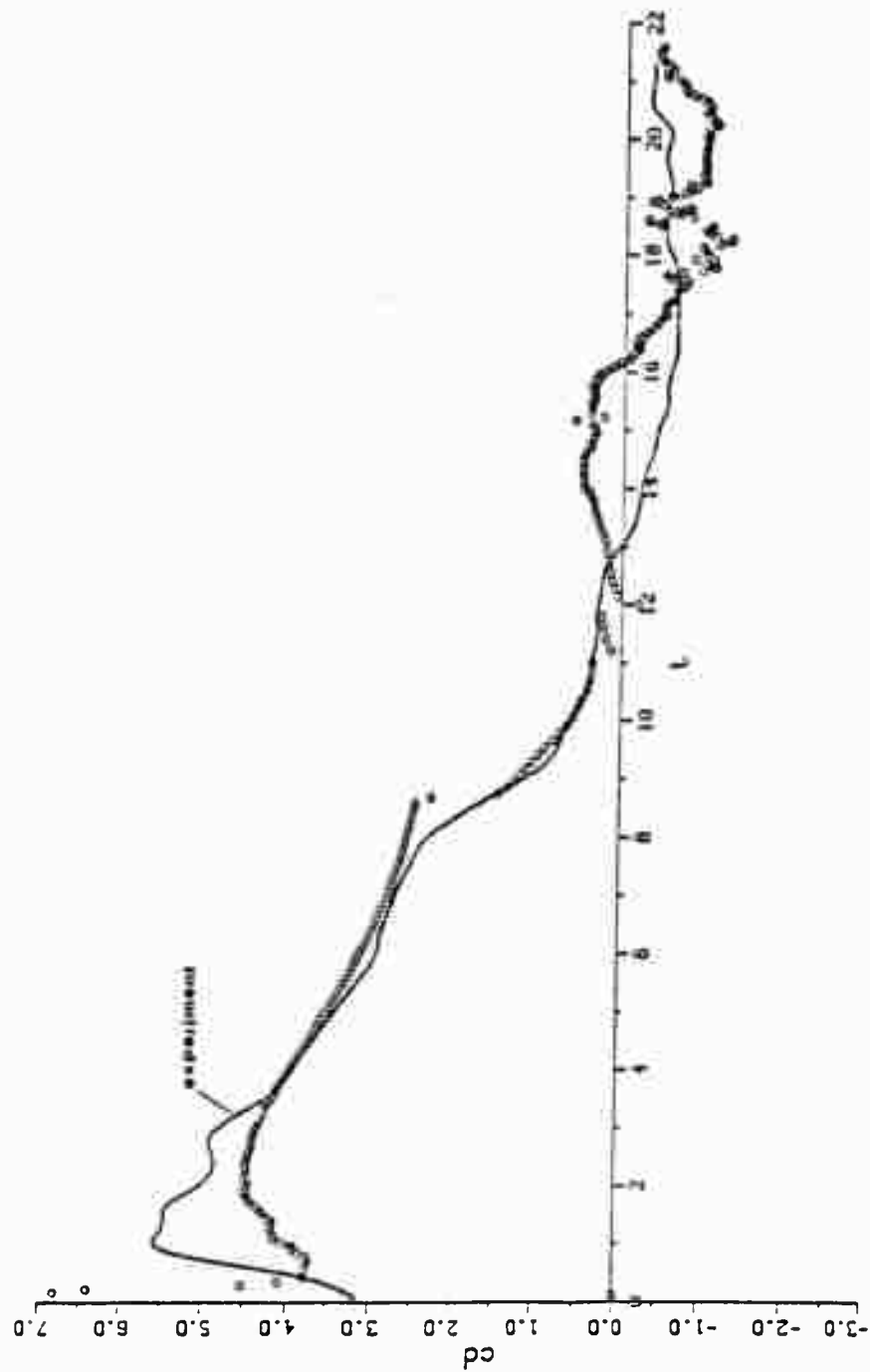into closer agreement in an ad hoc manner by introducing

126

Fig. 49 Comparison of the Calculated and Measured Drag Coefficients
(Case No. 1 for the Model A)

127

a small artificial reduction in circulation. This would account indirectly for the effects of the three-dimensional instability. This has been avoided in the present analysis in order to keep the discrete vortex analysis as pure and simple as possible. Figure 49 also shows that the calculation of the drag coefficient through the integration of pressure is superior to that through the use of the rate of change of impulse.

Figure 50 shows a comparison of the measured and calculated drag coefficients for the second ambient velocity history [Eqs. (40a)-(40c)]. Once again the measured and calculated drag coefficients are in good agreement, except in the region towards the end of the deceleration period. The possible reasons for this have already been discussed above.

Figures 51 through 53 show a comparison of the calculated and photographed flow fields at corresponding times (T* = 6.05, 8.55, and 16.30). The agreement between the two flow fields is indeed very good, including the regions of secondary separation.

The objective of the present analysis was not the exact duplication of the experimental data but rather the development of a robust computer code based on the discrete vortex analysis with which numerical experiments can be conducted with confidence. The results presented
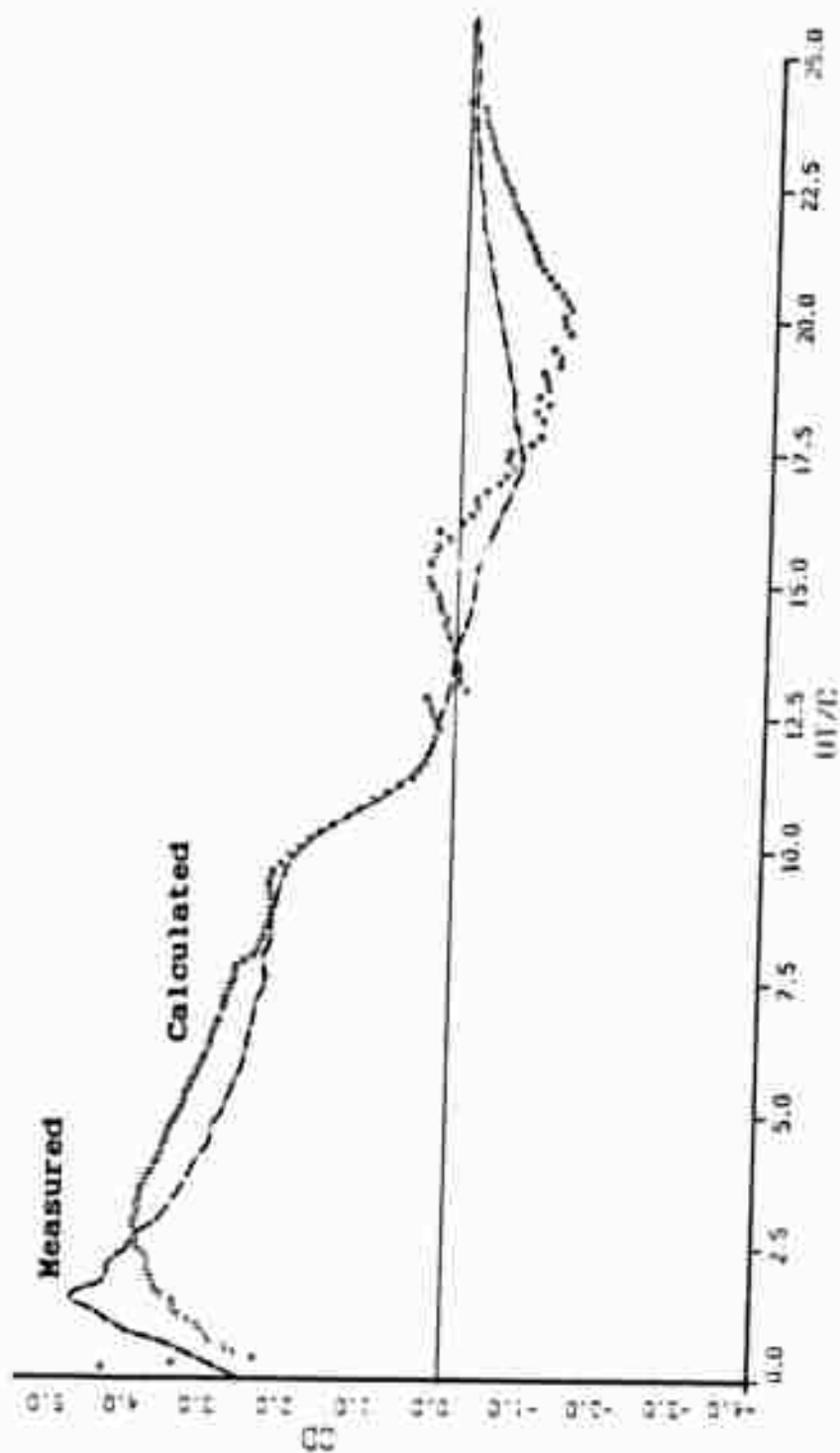
Fig. 50 Comparison of the Measured and Calculated Drag Coefficients
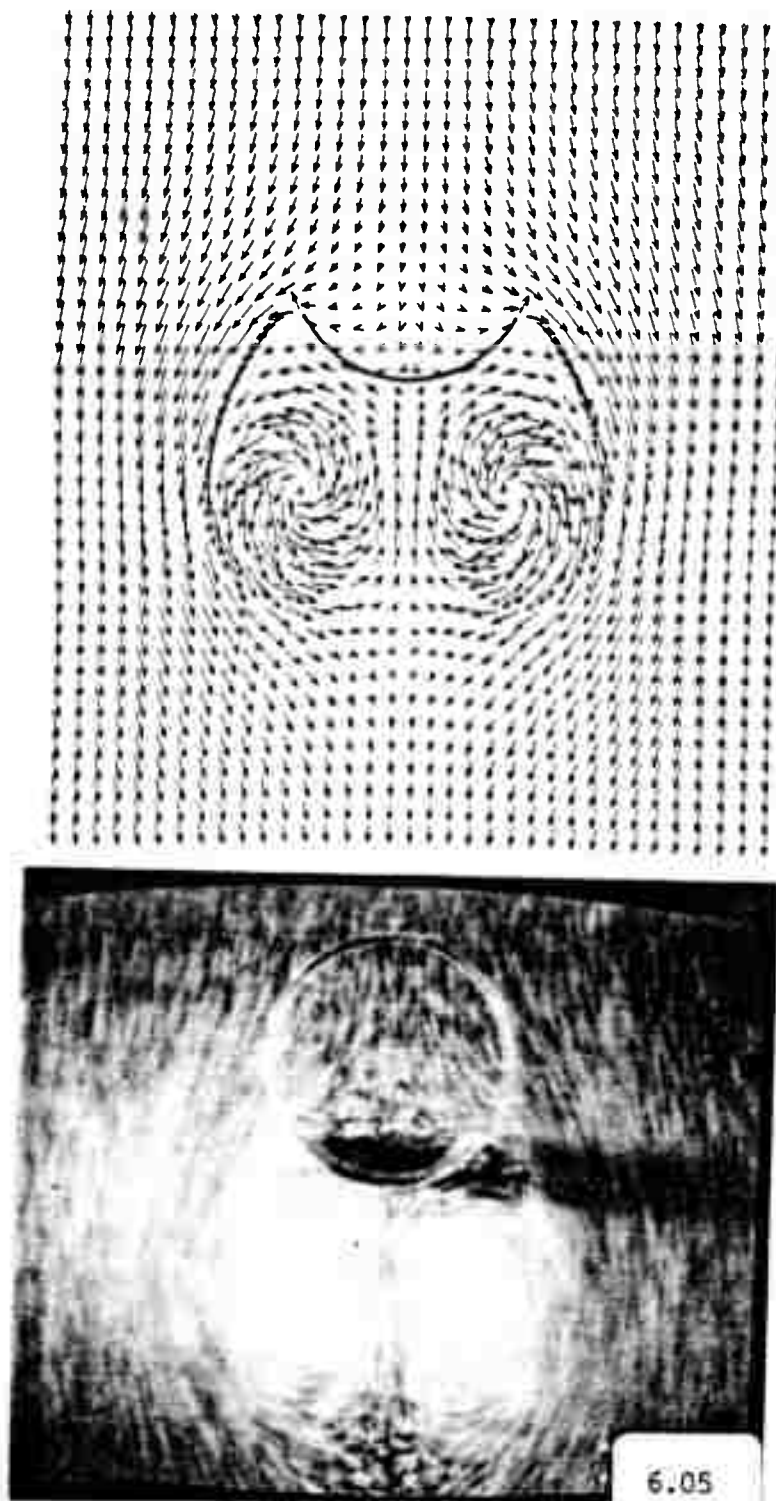(Case No. 2 for the Model A)
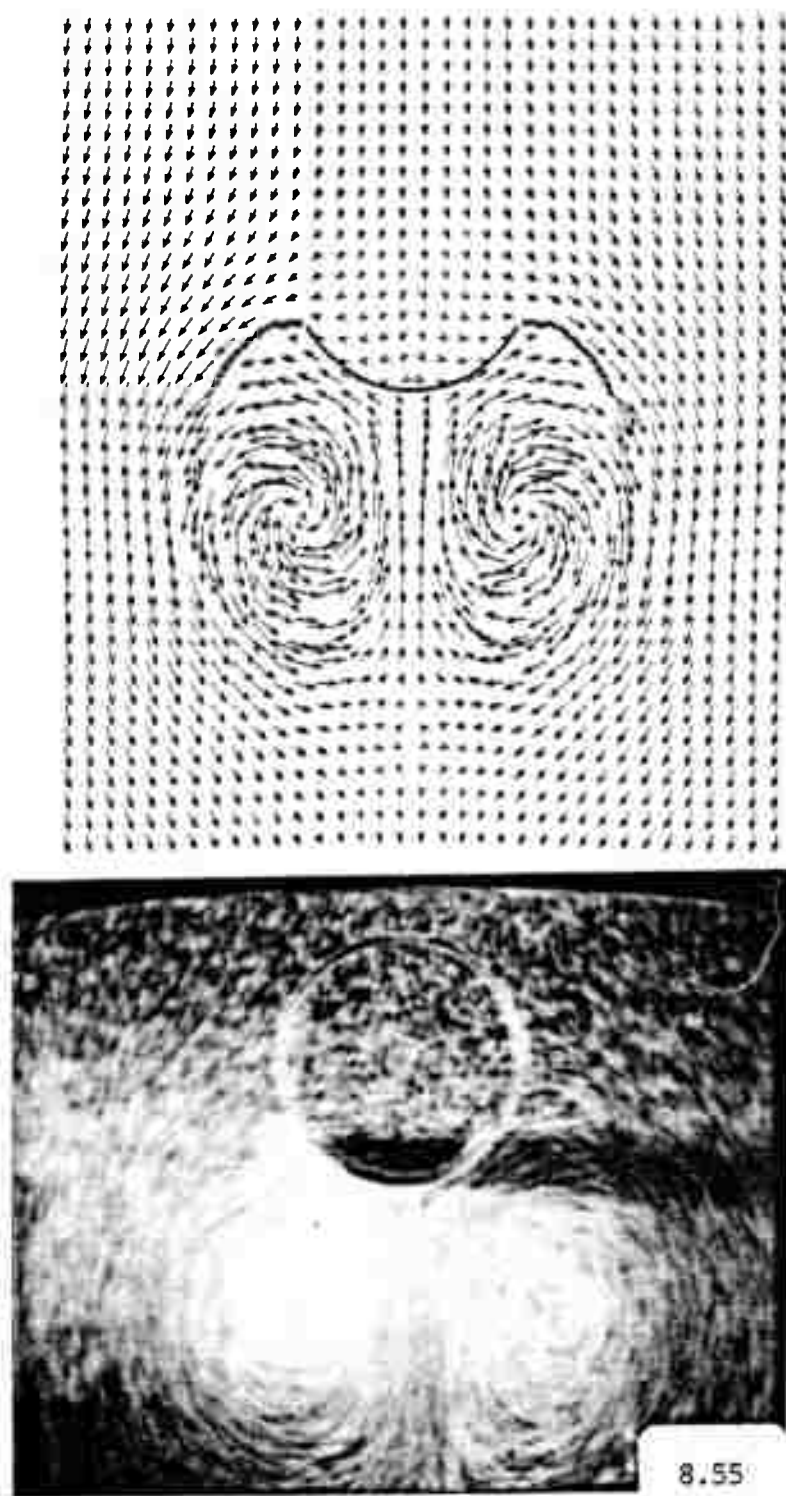
Fig. 51 Comparison of the Flow Fields at T* = 6.05
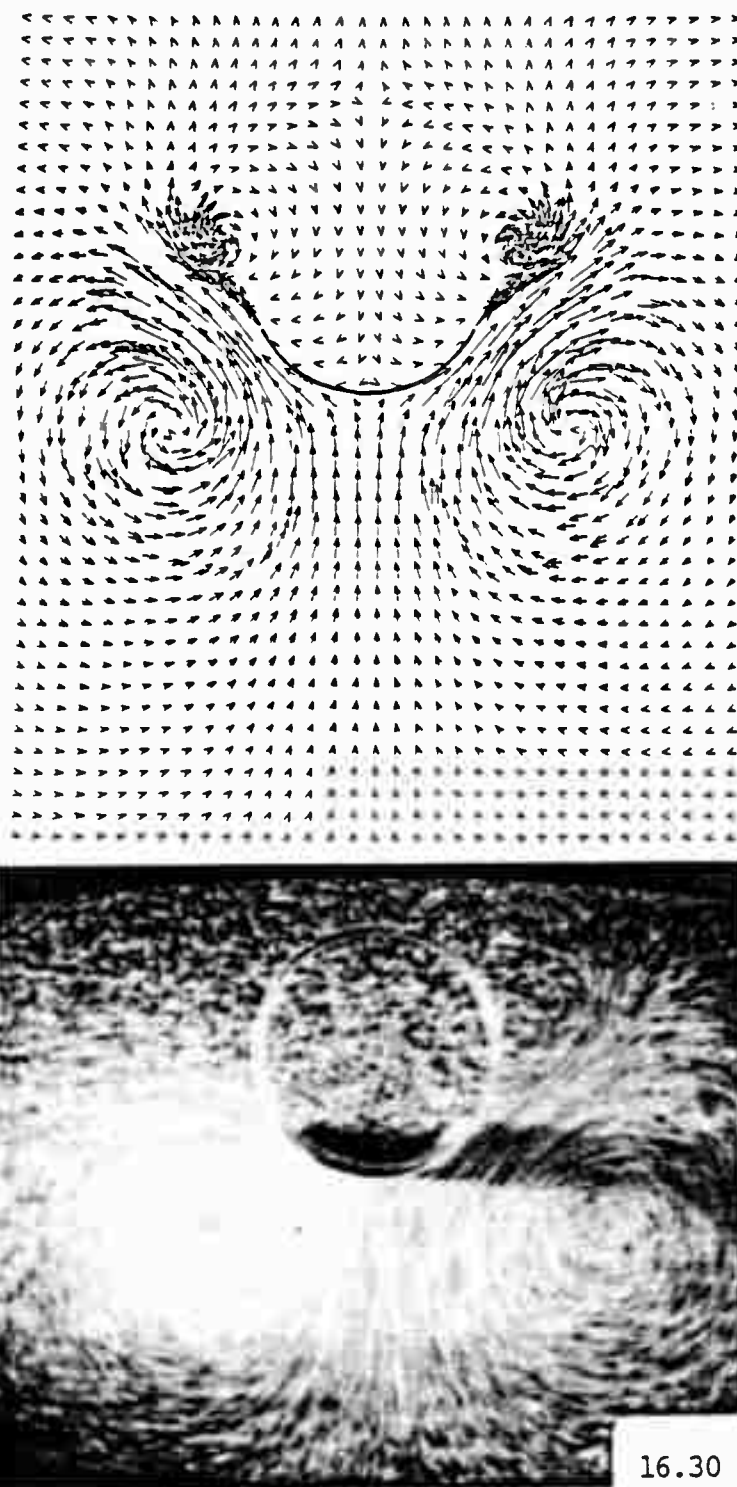
Fig. 52 Comparison of the Flow Fields at T* = 8.55

131

Fig. 53 Comparison of the Flow Fields at T* = 16.30

132

herein show that this objective has been achieved as far
as the Model A is concerned.

6.2 Model B

The   calculations   were   carried   out   for   a
representative,   time-dependent,   normalized   velocity,
given by

$$U/U_o = 1 \quad \text{for} \quad T^* < 10.2 \qquad\qquad (41a)$$
$$U/U_o = 0.5 + 0.5 \cos[0.5233 \ (T^* - 10.2)] \qquad (41b)$$
$$\text{for} \ 10.2 < T^* < 16.28$$

For this profile (see Fig. 54), the flow begins to
decelerate at $T^* = 10.2$ and the velocity of the ambient
flow reduces to zero at $T^* = 16.28$.

The computer program provided, at times specified,
the positions of all the vortices, the rate of shedding
of vorticity from the tips of the camber, the velocity
distribution on the upstream and downstream faces of the
camber,   the   total   and   differential   pressure
distributions, and the force coefficients.

Figures 55 through 60 show, at $T^* = 6.00$, 10.4,
13.4, 14.9, 19.4, and 23.9, the evolution of the wake and
the differential pressure distribution. It is seen that
the characteristics of the flow develop symmetrically

133
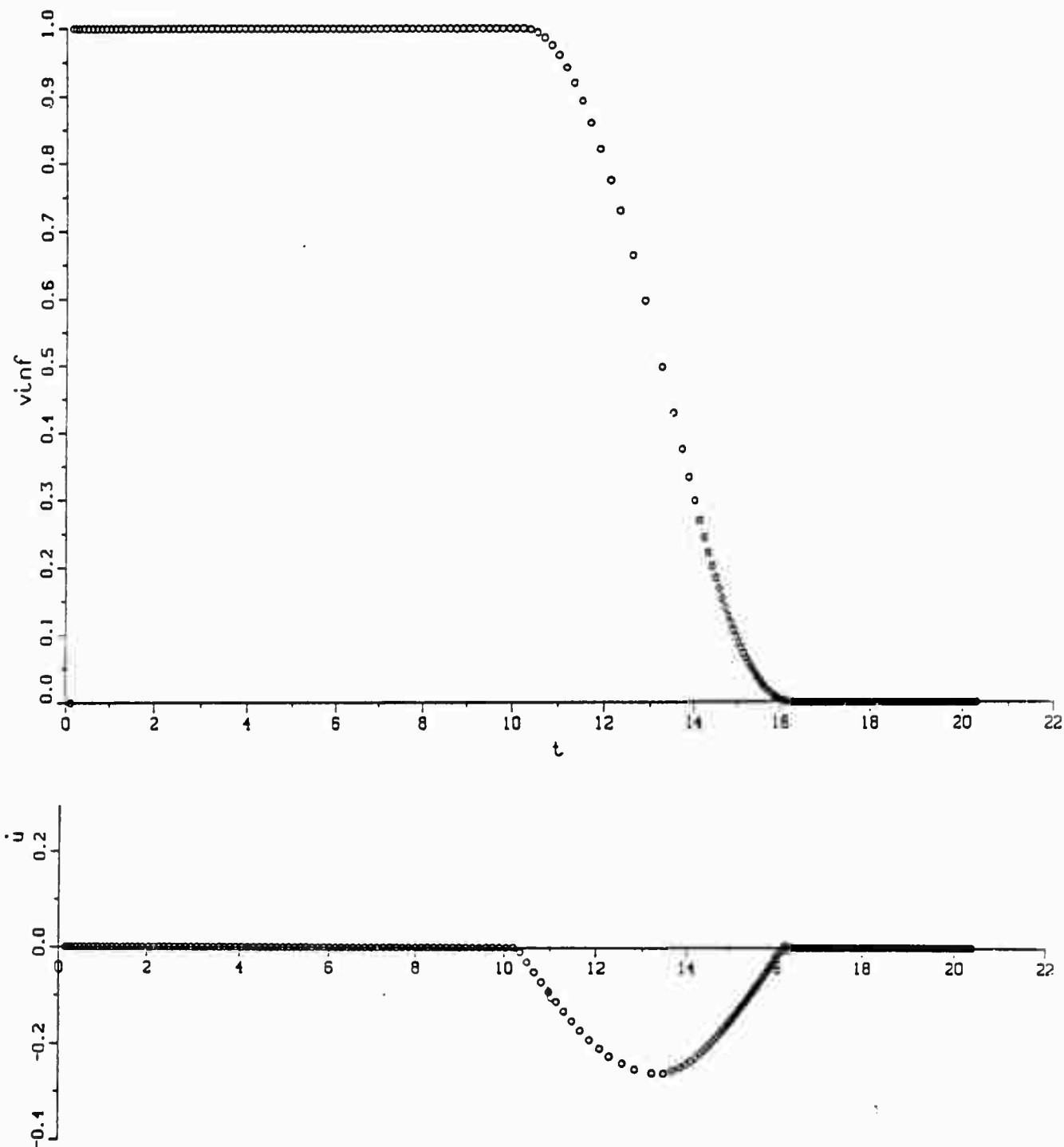
Fig. 54   Variations of the Velocity and Acceleration
           for the Model B

134

Fig. 55 Velocity Field and the Differential Pressure
Distribution at T* = 6.00 (Model B)

135

Fig. 56   Velocity Field and the Differential Pressure
Distribution at T* = 10.40 (Model B)

Fig. 57   Velocity Field and the Differential Pressure
           Distribution at T* = 13.40 (Model B)

137

Fig. 58   Velocity Field and the Differential Pressure
Distribution at T* = 14.90 (Model B)

138

Fig. 59 Velocity Field and the Differential Pressure
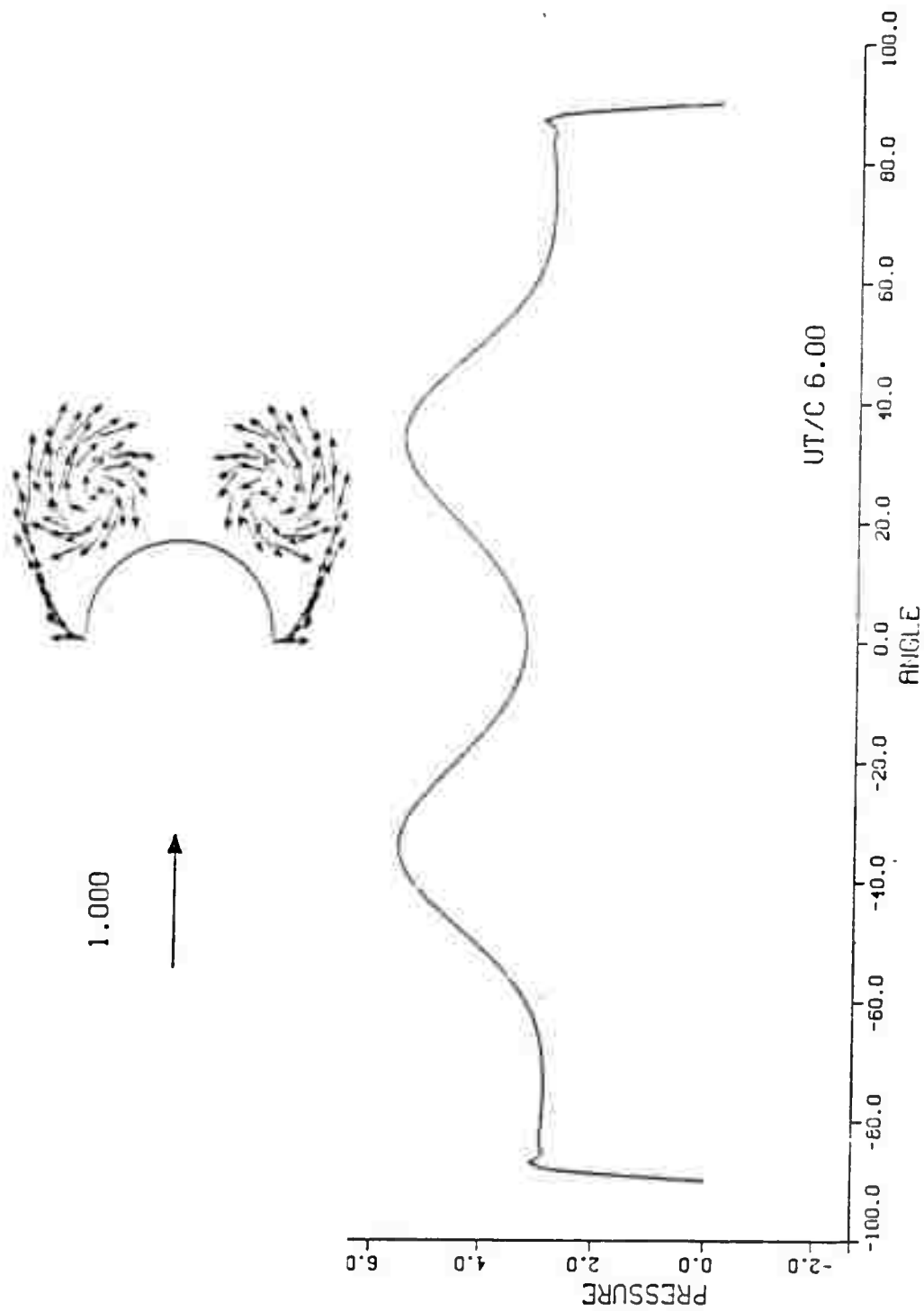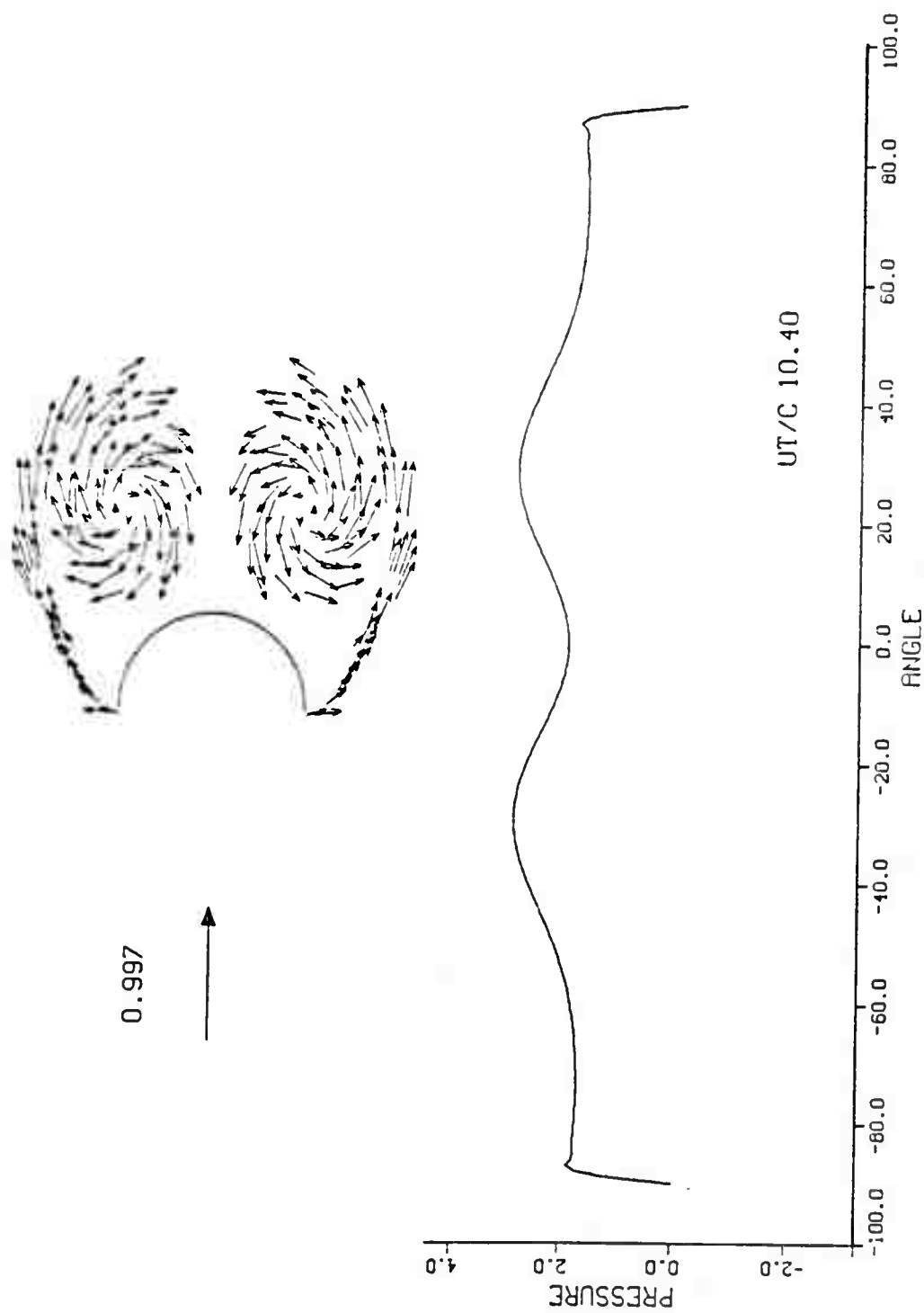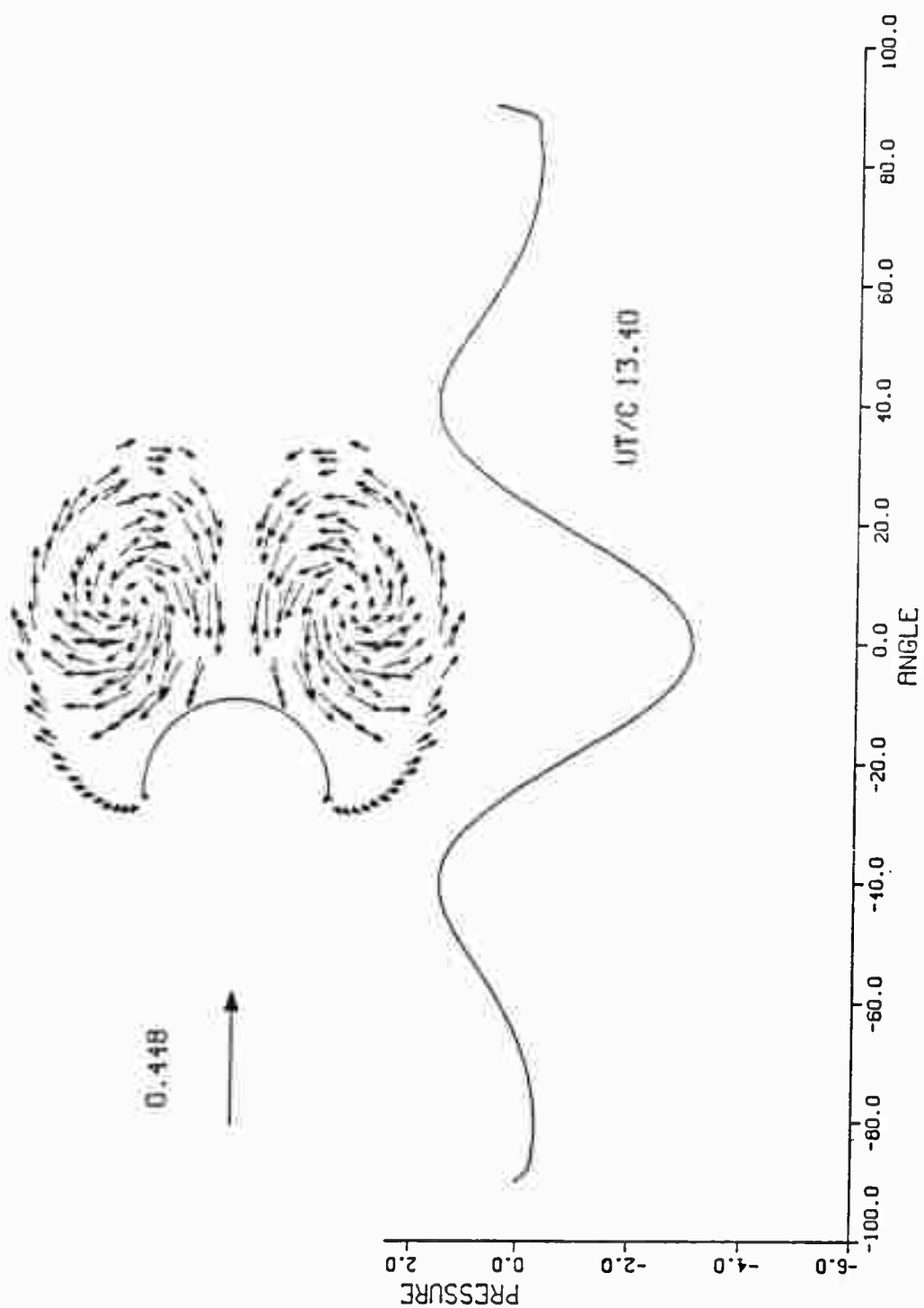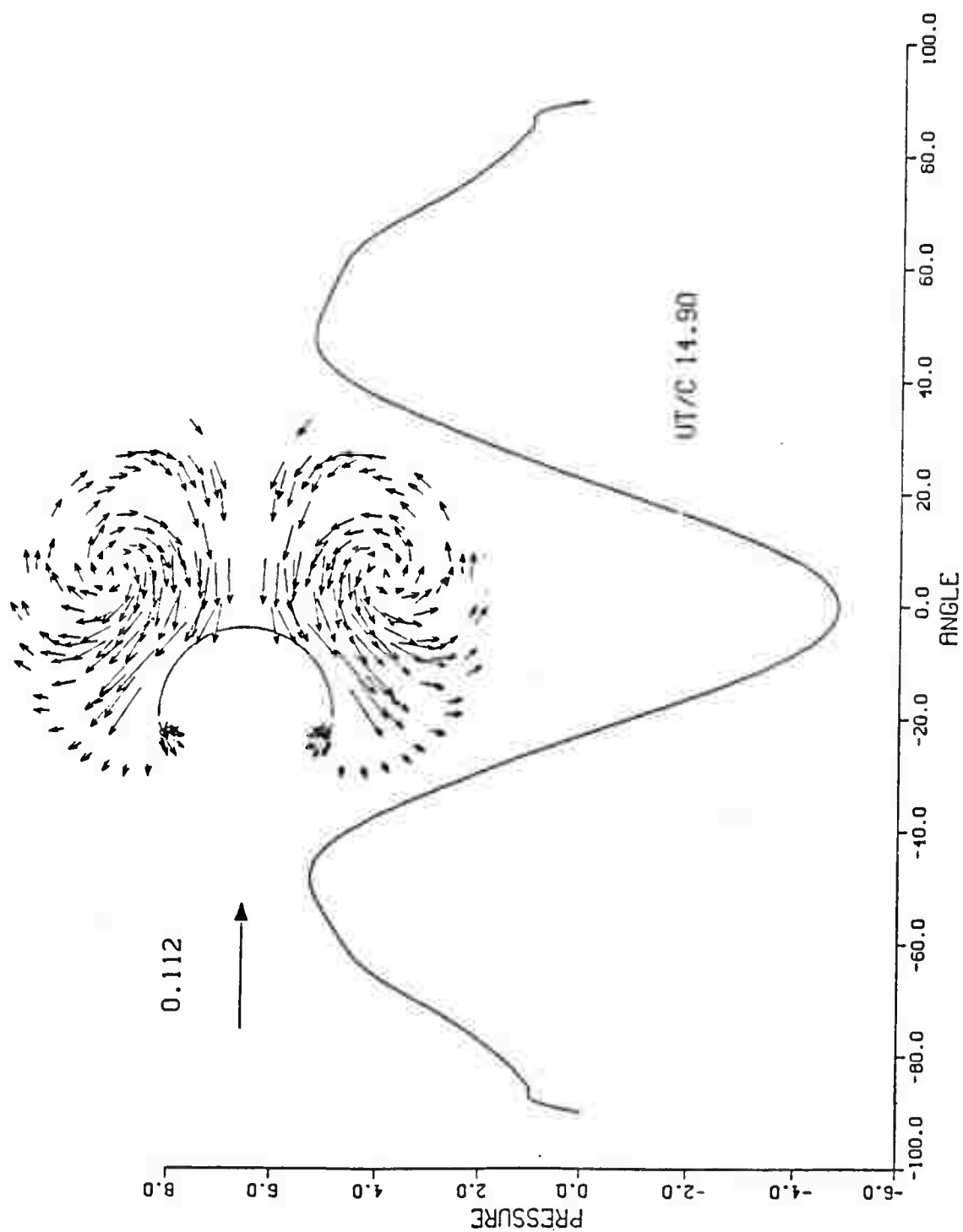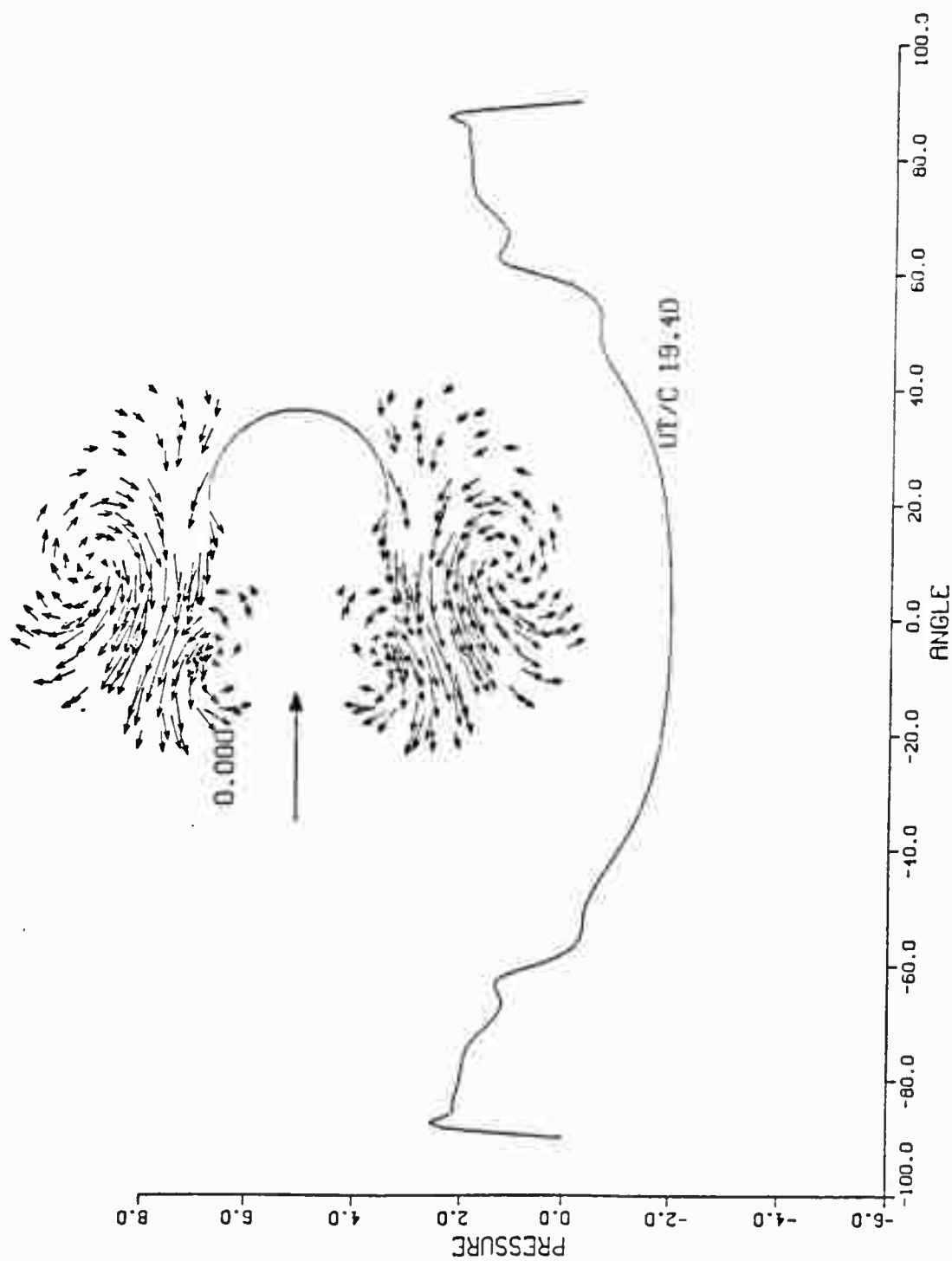Distribution at T* = 19.40 (Model B)

139
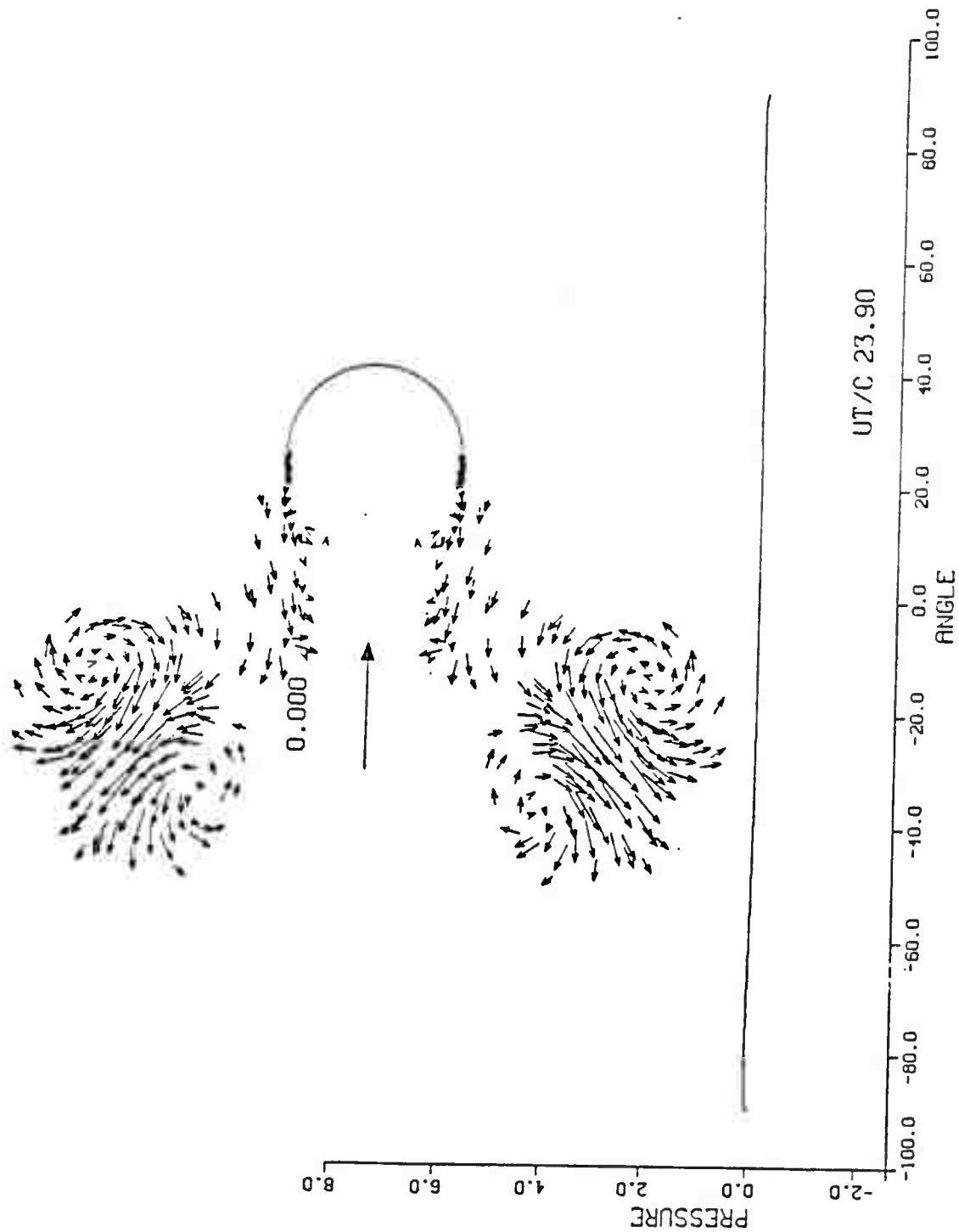
Fig. 60 Velocity Field and the Differential Pressure
Distribution at T* = 23.90 (Model B)

prior to the onset of deceleration (at T* = 10.20, see Figs. 54 and 56) and the differential pressure is positive everywhere (i.e., the pressure inside the camber is larger than that outside).

Towards the middle of the deceleration period (see Figs. 54 and 57 at T* = 13.40), the differential pressure near the axis of the camber becomes increasingly negative. The reason for this is that the deceleration of the flow brings the vortices closer to the camber. As noted earlier, had the model B been flexible the central part of the camber would have collapsed as a result of the particular deceleration it is subjected to.

For T* larger than about 14 (for the ambient flow under consideration), the velocities induced at the downstream edges of the camber by the large vortices moving towards the camber give rise to oppositely-signed vorticity. This, in turn, leads to the rapid growth of the secondary vortices (see Fig. 58 at T* = 14.90). The secondary vortices are relatively weaker than the primary vortices partly because they have been in existence only for a short time and partly because the vorticity flux is not as large as that in the primary shear layers. The primary and secondary vortices on each side of the camber form a counter-rotating couple and remove themselves rapidly from the field under the influence of their

141

mutual induction velocity (see Figs. 59 and 60). Subsequently, the absolute value of the differential pressure begins to decrease (see Fig. 59). Eventually, the differential pressure reduces to zero everywhere on the camber as the conditions approach those of a body in a fluid at rest (see Fig. 60).

Figure 61 shows a comparison of the calculated (through pressure integration) and measured drag coefficients as a function of T^*. It is seen that C_d rises rapidly (due to the rapid accumulation of vorticity in the growing vortices). Then the measured force decreases sharply at the onset of deceleration and goes through zero at $T^* = 12.3$, as the magnitude of deceleration increases towards its maximum value (see Fig. 54). The measured force acquires its largest negative value at about $T^* = 14$, as the magnitude of the deceleration begins to decrease. Subsequently, the measured force gradually decreases to zero.

The calculated C_d also goes through zero at $T^* \approx 12$ but then rises to a relatively large plus value at the end of the deceleration period ($T^* \approx 15.5$). Subsequently, it crosses zero at $T^* \approx 17$ and gradually approaches zero from a relatively large negative minimum.

It is clear from the foregoing that the calculated and measured drag coefficients are not in good agreement
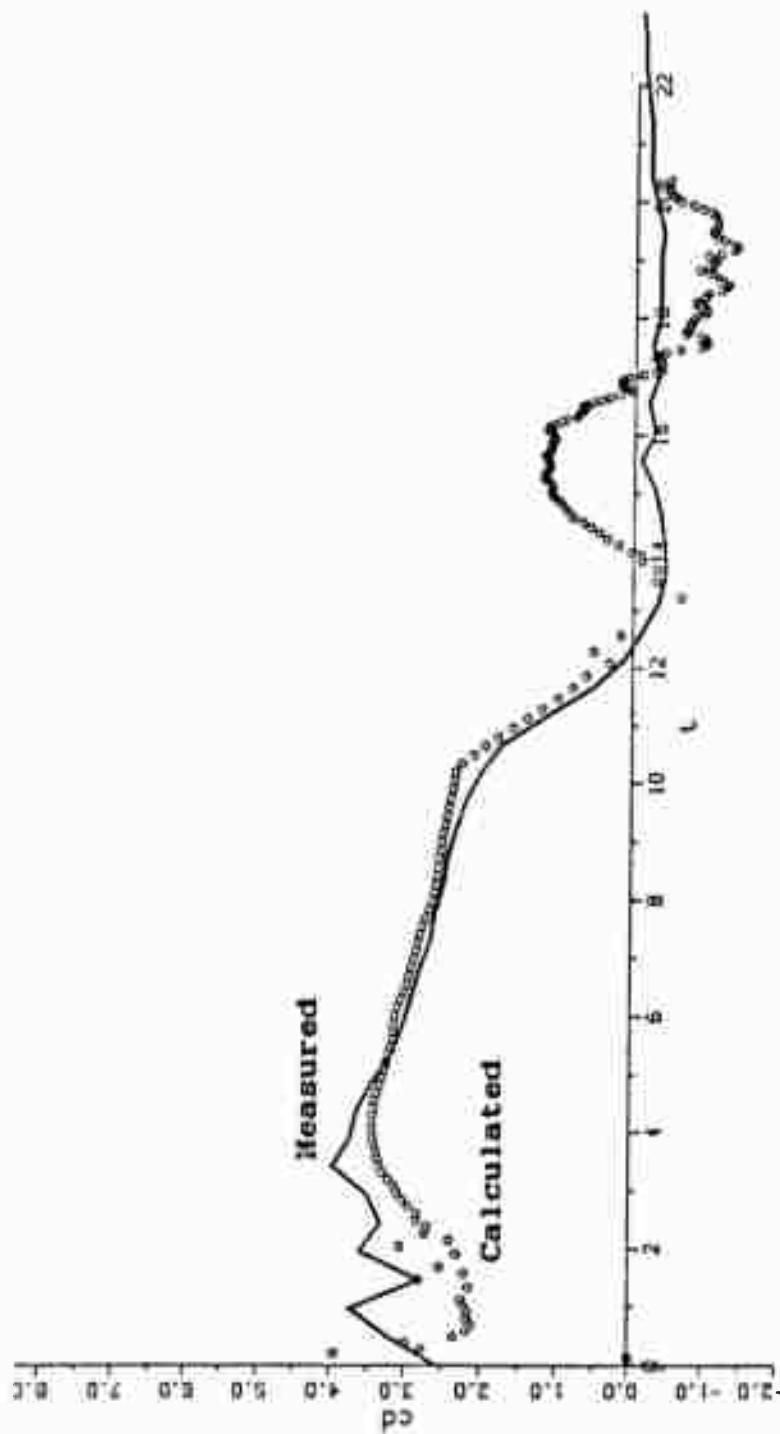
142

Fig. 61 Comparison of the measured and Calculated
Drag Coefficients (Model B)

143

after the second half of the deceleration period (see T^* = 13.5 in Figs. 54 and 61). There are three possible reasons for this disagreement. First, for $T^* > 13$ the drag coefficient is relatively small and the viscous and turbulent effects are important in diffusing the vortices (assumed to be point vortices in the analysis). Second, the experiments have shown that the deceleration period is accompanied with strong three-dimensional instabilities in the vortices. Thus, the relatively small drag force occurring during the deceleration period is an integrated average of the effects of this three-dimensional instability on the pressure distribution.

The third reason for the said differences is thought to be the occurrence of additional separations behind the camber. As noted in connection with the discussion of the experimental results, the return of the primary vortices to the camber gives rise to separations on the back face of the camber, during part of the deceleration period (in the interval $11 < T^* < 14.5$). These precede the occurrence of secondary separations at the tips (which occur at $T^* > 14.5$) and are far more pronounced for cambers with large included angles (180 and 240 degrees). The separation on the downstream face of the camber has not been included in the analysis in order to minimize time and to perform the calculations with a desk-top computer. It is clear that the effect of such

144

separations is to produced oppositely-signed. vorticity, reduce the strength of the primary vortices, and minimize the effect of the subsequent separation and vortex formation at the tips of the camber. This has not yet been taken into consideration in the numerical analysis.

It is possible to bring the calculated and measured forces into closer agreement by introducing a small artificial reduction in circulation in order to account (albeit indirectly) for the effects of the three-dimensional instability. This has been avoided in the present analysis partly to keep the discrete vortex analysis as pure and simple as possible, partly to understand the fundamental physical reasons, and partly to discover the shortcomings of the numerical methodology leading to the differences between the measured and calculated forces.

The numerical simulation of the behavior of flow during the deceleration period (occurrence of back-face separation, followed by tip separation) emerges as an important and challenging problem. This is currently under investigation. Suffice it to note that for cambers with relatively small included angles (e.g., the model A) the effect of the back-face separation is negligible. Thus, the comparison of **the difference** between the measured and calculated forces for the model A (Figs. 49

145

and 50) with that of the model B (Fig. 61) shows that both the back-face separation and the three-dimensional instability play important and additive roles during the deceleration period.

The calculations have also shown that the lift force is negligible even in the later stages of the motion. A similar result was found for the model A. This is primarily due to the fact that there is not sufficient time for the development of alternate vortex shedding either during the period of steady flow or during the period of rapid deceleration.

Figure 62 shows a sample comparison of the calculated and photographed flow fields at corresponding representative times $(T^* = 10.4, 13.4, \text{ and } 14.9)$. The agreement between the two flow fields, as judged by the positions of the vortices, is indeed very good. The comparison of the vortex strengths at corresponding times is left for future studies.

The numerical and experimental studies with the model B have shown that the measured and calculated forces agree quite well from the time of inception of the flow to the early stages of the deceleration period. There are, however, some important differences between the measurements and predictions during the remainder of the deceleration period and during the period for which
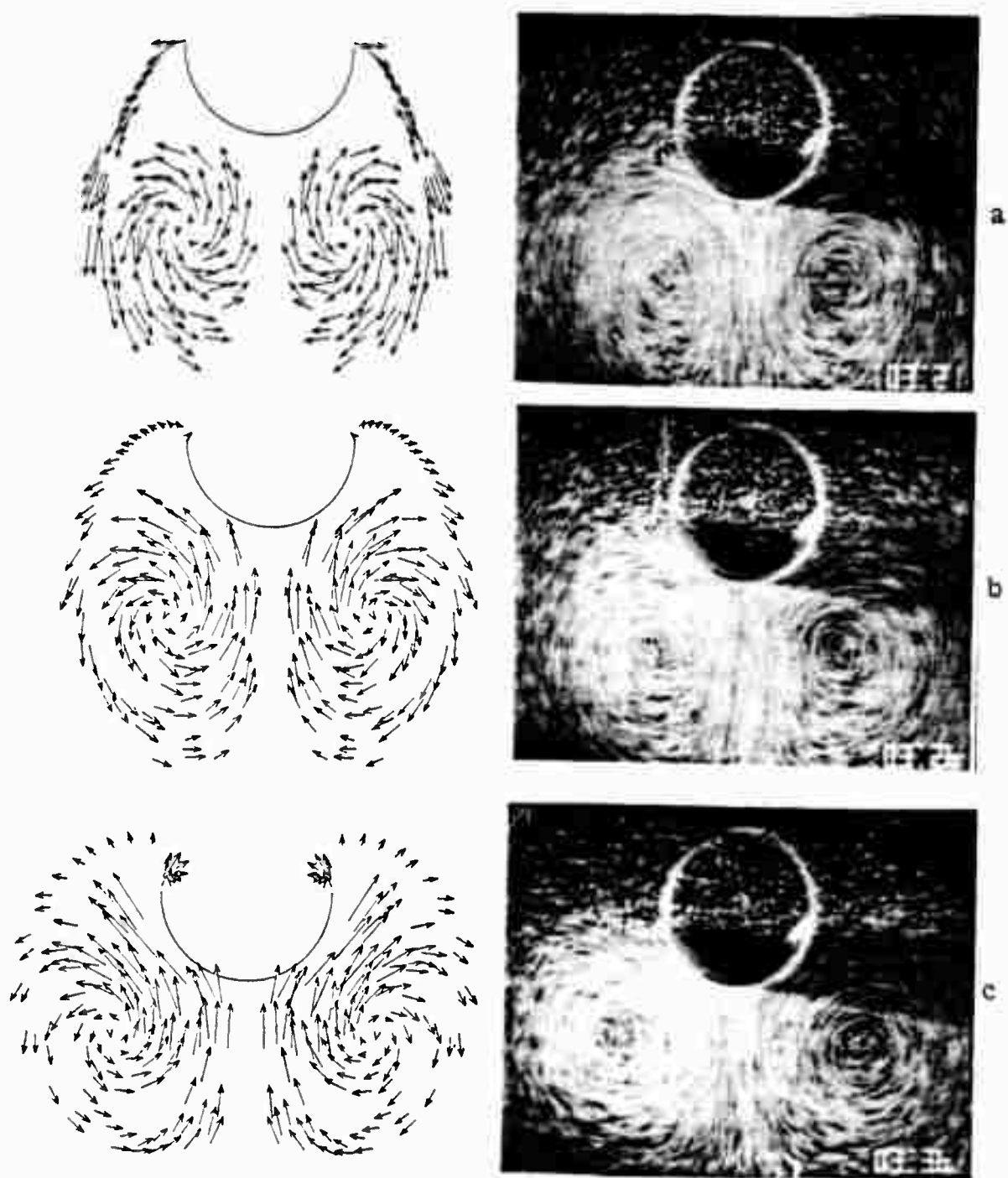
146

Fig. 62   Comparison of the calculated and photographed
          Flow Fields at (a) T* = 10.40, (b) T* = 13.40,
          and (c) T* = 14.90

the velocity of the ambient flow is zero. The reasons for these differences have been discussed in detail. They will be the subject of further studies. As in the case of the model A, the lift force was found to be negligible. Finally, it has been shown, through the use of representatives plots and photographs, that the kinematics of the flow field is well represented by the numerical analysis.

6.3   Model C

The calculations were carried out for a representative, time-dependent, normalized velocity, given by

$$U/U_o = 1 \quad \text{for} \quad T^* < 10 \tag{42a}$$

$$U/U_o = 0.5 + 0.5 \cos[0.34 \, (T^* - 10)] \tag{42b}$$
$$\text{for} \quad 10 < T^* < 19.25$$

For this profile (see Fig. 63), the flow begins to decelerate at $T^* = 10$ and the velocity of the ambient flow reduces to zero at $T^* = 19.25$.

The computer program provided, at times specified, the positions of all the vortices, the rate of shedding of vorticity from the tips of the camber, the velocity distribution on the upstream and downstream faces of the
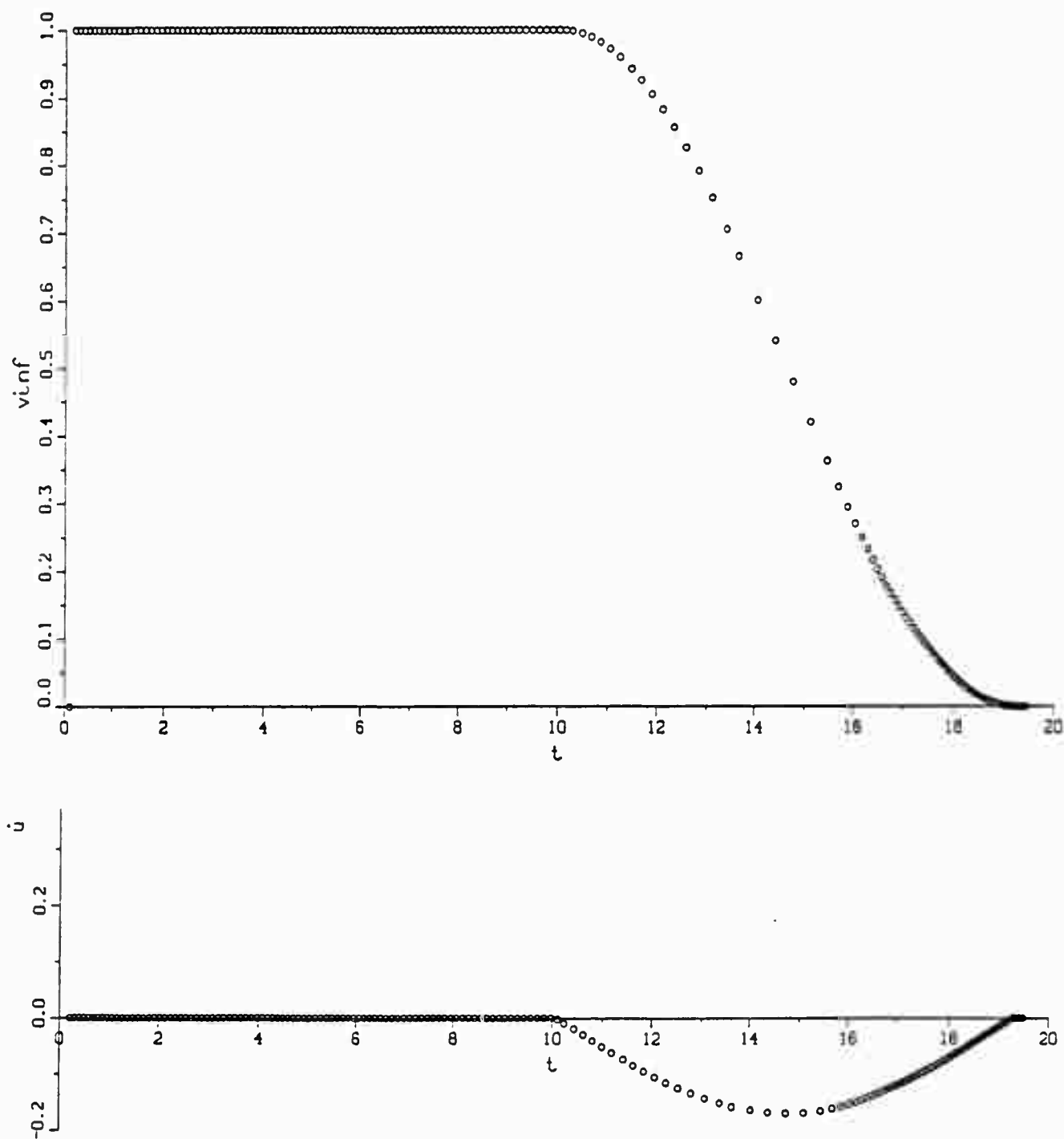
148

Fig. 63 Variations of the Velocity and Acceleration
         for the Model C

149

camber, the total and differential pressure distributions, and the force coefficients.

Figures 64 through 70 show, at $T^* = 2.37$, 4.12, 7.77, 9.78, 12.99, 15.34, and 17.71, the evolution of the wake (in two scales) and the differential pressure distribution. It is seen that the characteristics of the flow develop symmetrically prior to the onset of deceleration (at $T^* = 10$, see Figs. 63 and 67) and the differential pressure is positive everywhere (i.e., the pressure inside the camber is larger than that outside).

Towards the first quarter of the deceleration period (see Figs. 63 and 68 at $T^* \approx 13$), the differential pressure near the axis of the camber becomes increasingly negative. The reason for this is that the deceleration of the flow brings the vortices closer to the camber. As noted earlier, had the model C been flexible the central part of the camber would have collapsed as a result of the particular deceleration it is subjected to.

For T^* larger than about 16 (for the ambient flow under consideration), the velocities induced at the downstream edges of the camber by the large vortices moving towards the camber give rise to oppositely-signed vorticity. This, in turn, leads to the rapid growth of the secondary vortices (see Fig. 70 at $T^* = 17.71$). The secondary vortices are relatively weaker than the primary

POSITION OF VORTICES

DIFFERENTIAL PRESSURE
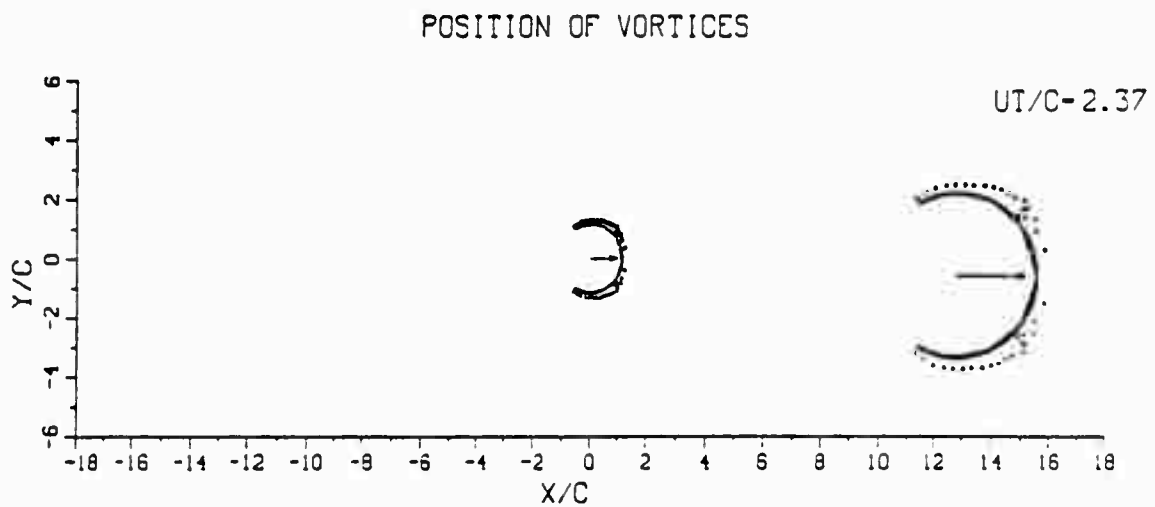
Fig. 64 Velocity Field and the Differential Pressure
Distribution at $T^* = 2.37$ (Model C)

151

POSITION OF VORTICES

DIFFERENTIAL PRESSURE

Fig. 65   Velocity Field and the Differential Pressure
           Distribution at T* = 4.12 (Model C)

152

POSITION OF VORTICES

DIFFERENTIAL PRESSURE
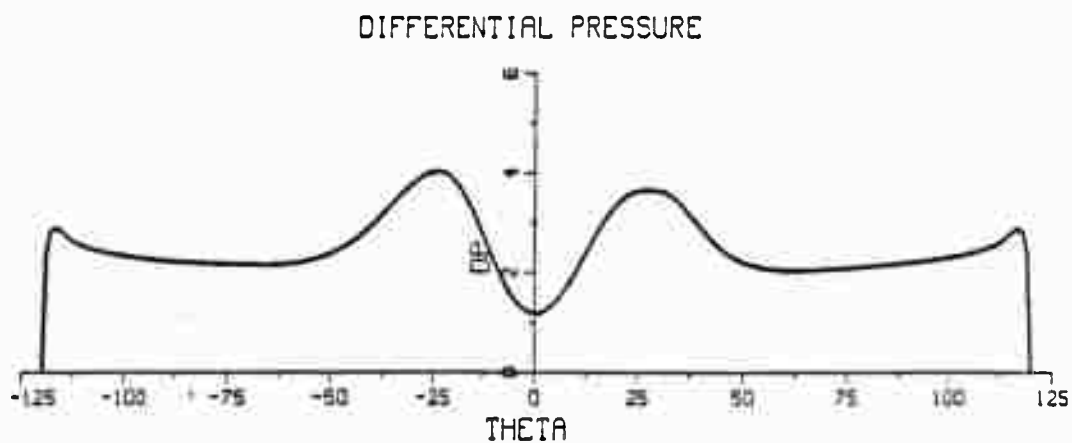
Fig. 66   Velocity Field and the Differential Pressure
          Distribution at T* = 7.77 (Model C)

153

POSITION OF VORTICES

DIFFERENTIAL PRESSURE
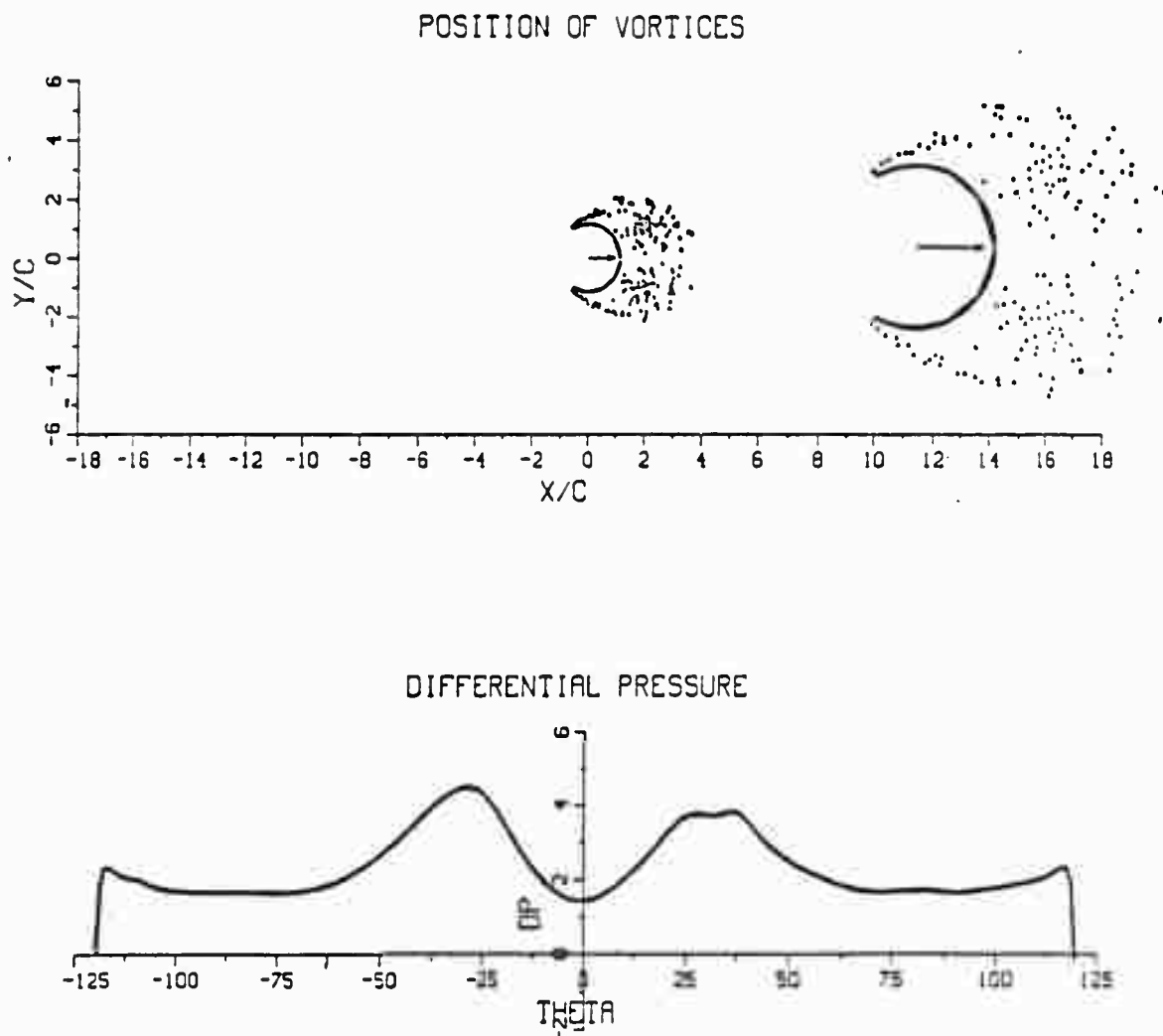
Fig. 67 Velocity Field and the Differential Pressure
         Distribution at T* = 9.78 (Model C)

154

POSITION OF VORTICES

DIFFERENTIAL PRESSURE
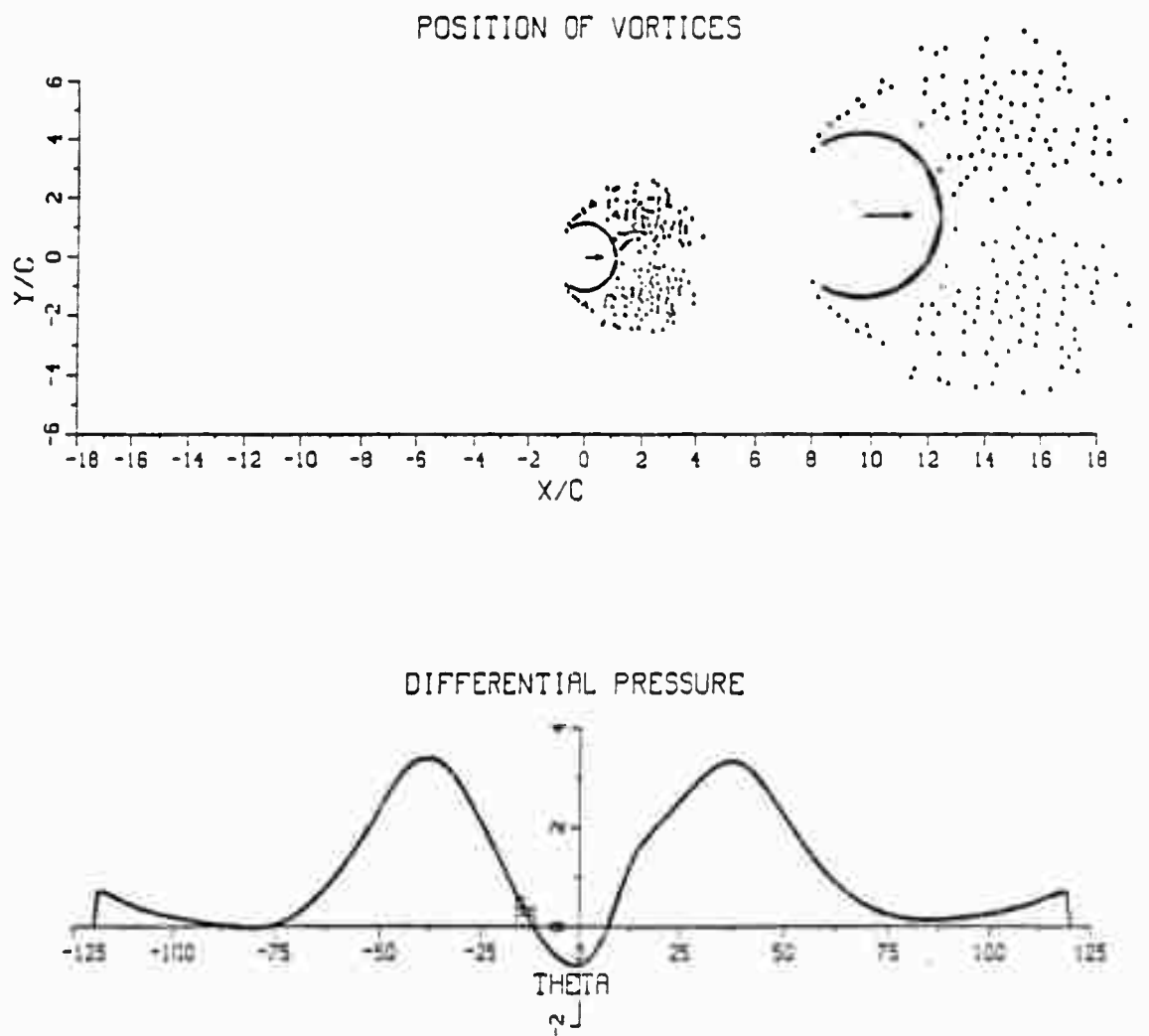
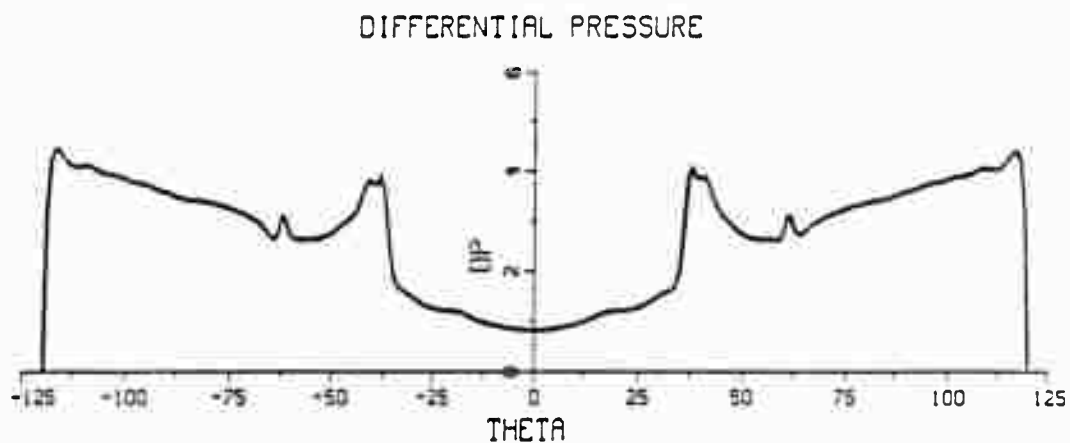

Fig. 68   Velocity Field and the Differential Pressure
Distribution at T* = 12.99 (Model C)

155

POSITION OF VORTICES

DIFFERENTIAL PRESSURE

Fig. 69 Velocity Field and the Differential Pressure
Distribution at T* = 15.34 (Model C)

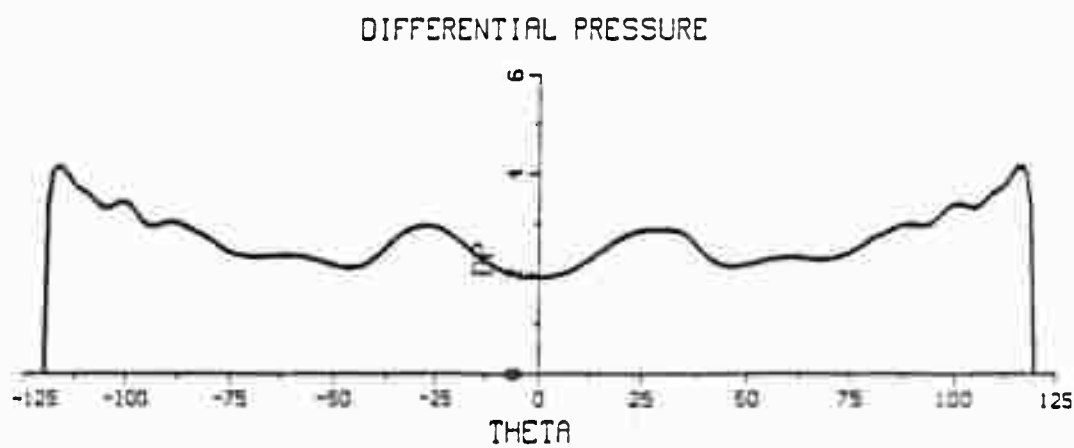156
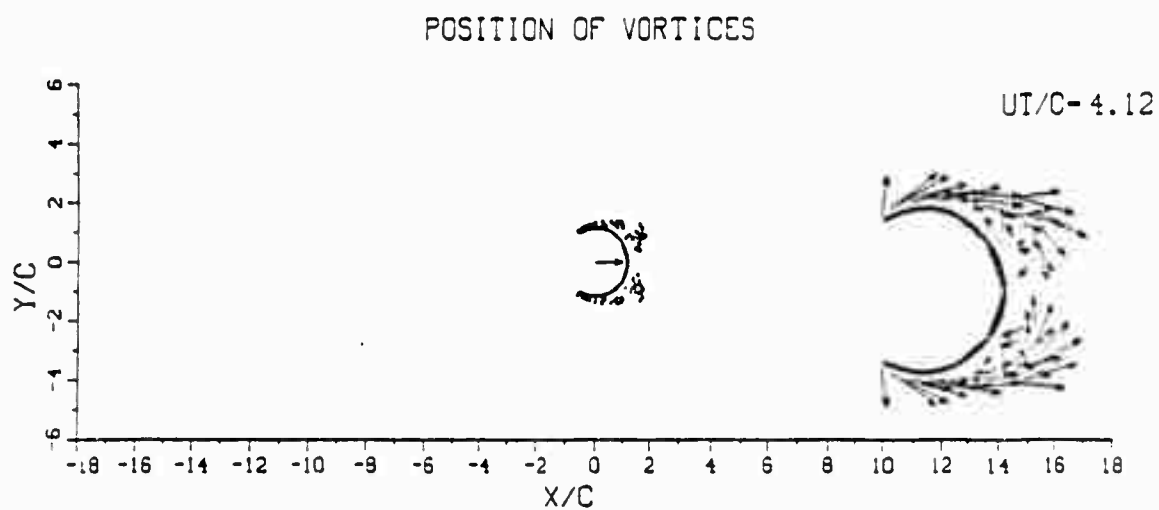
POSITION OF VORTICES

DIFFERENTIAL PRESSURE

Fig. 70 Velocity Field and the Differential Pressure
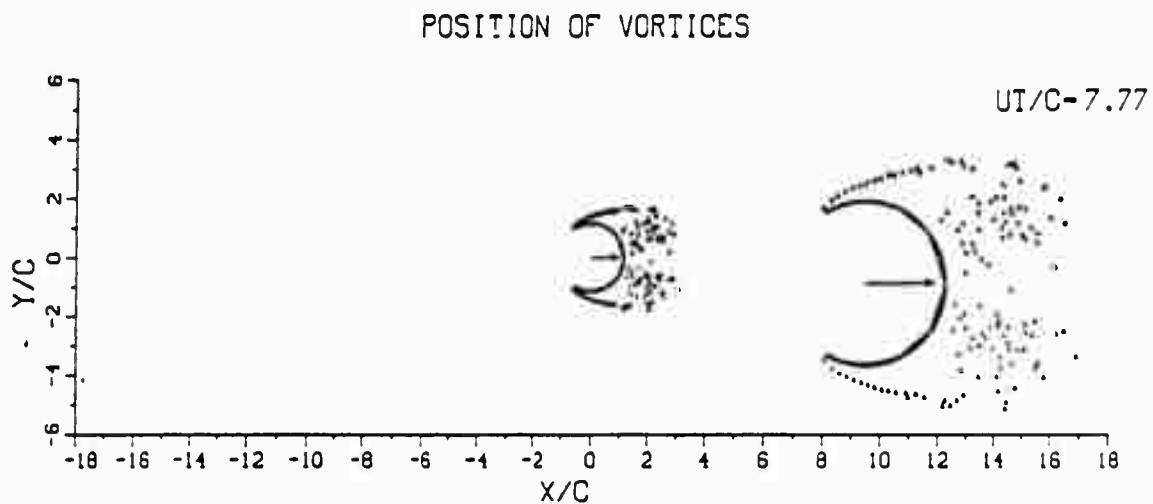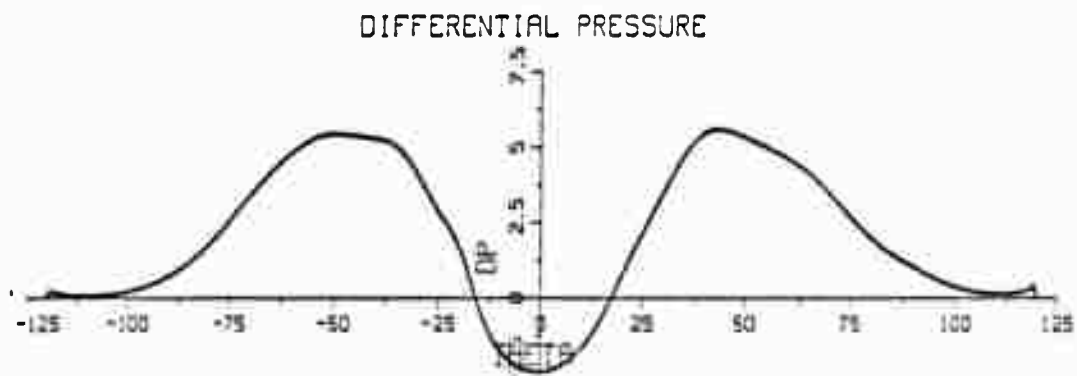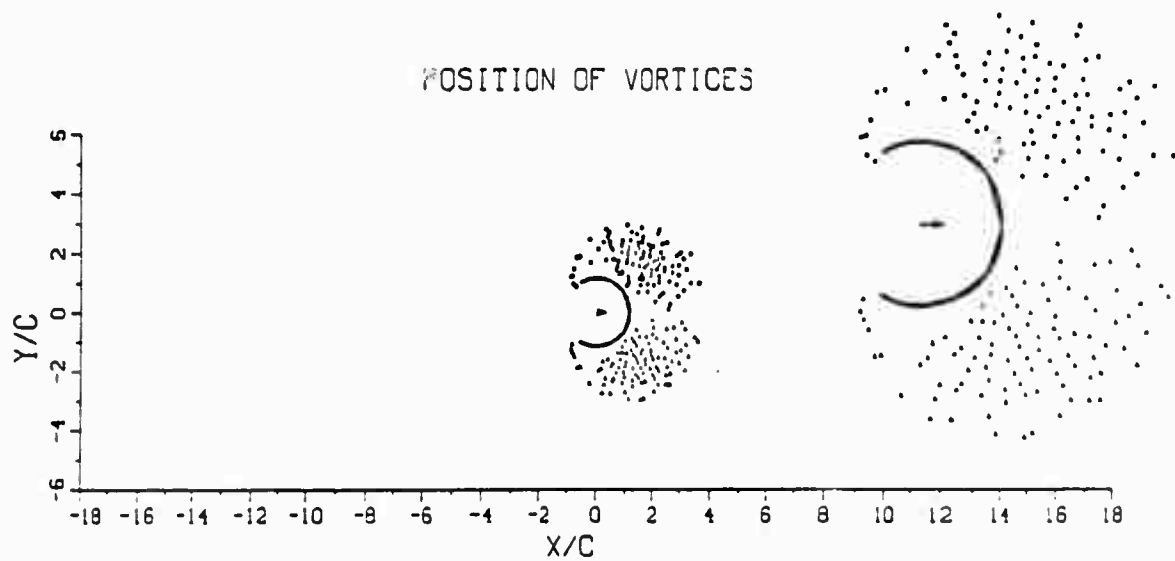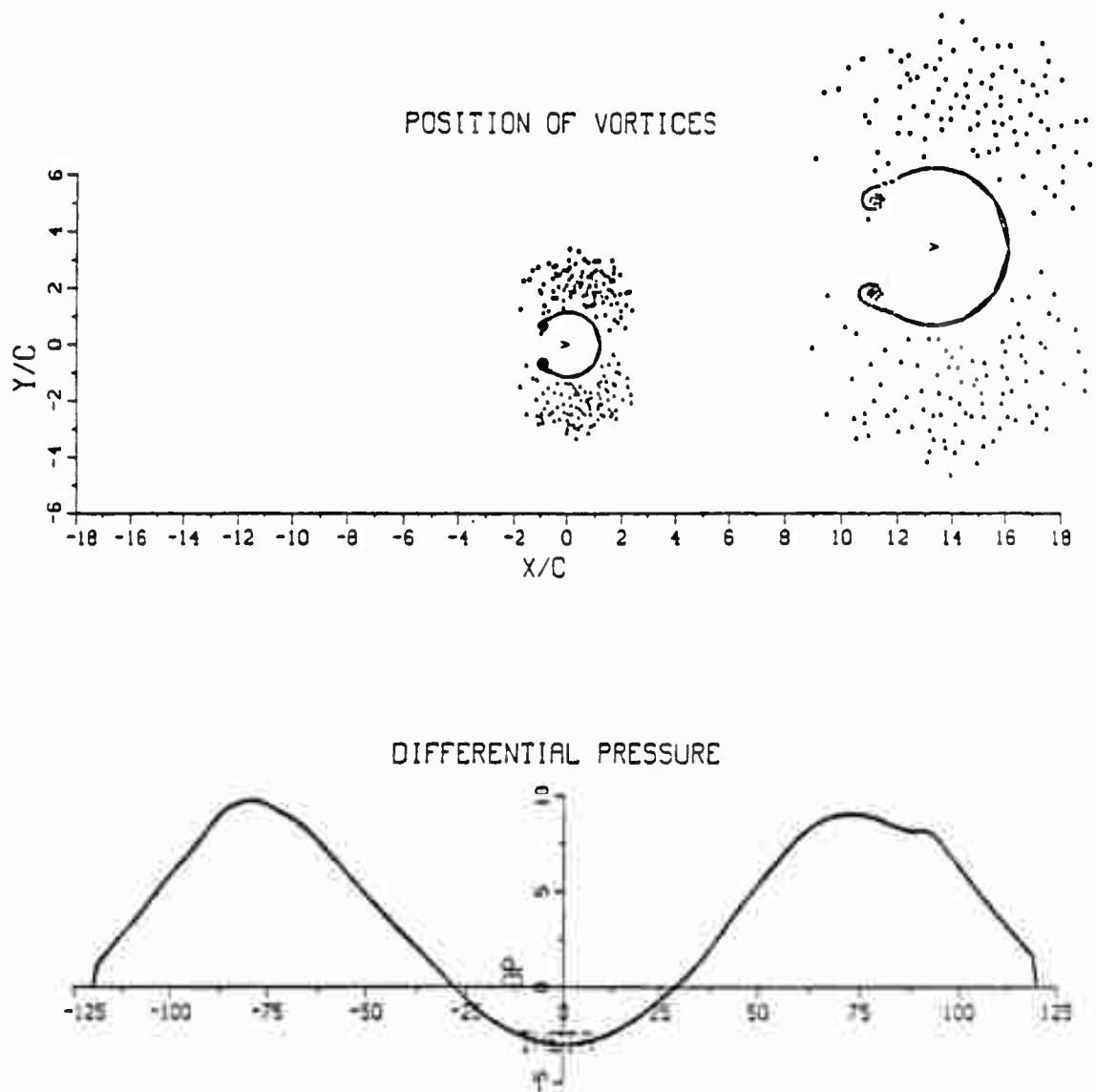Distribution at T* = 17.71 (Model C)

157
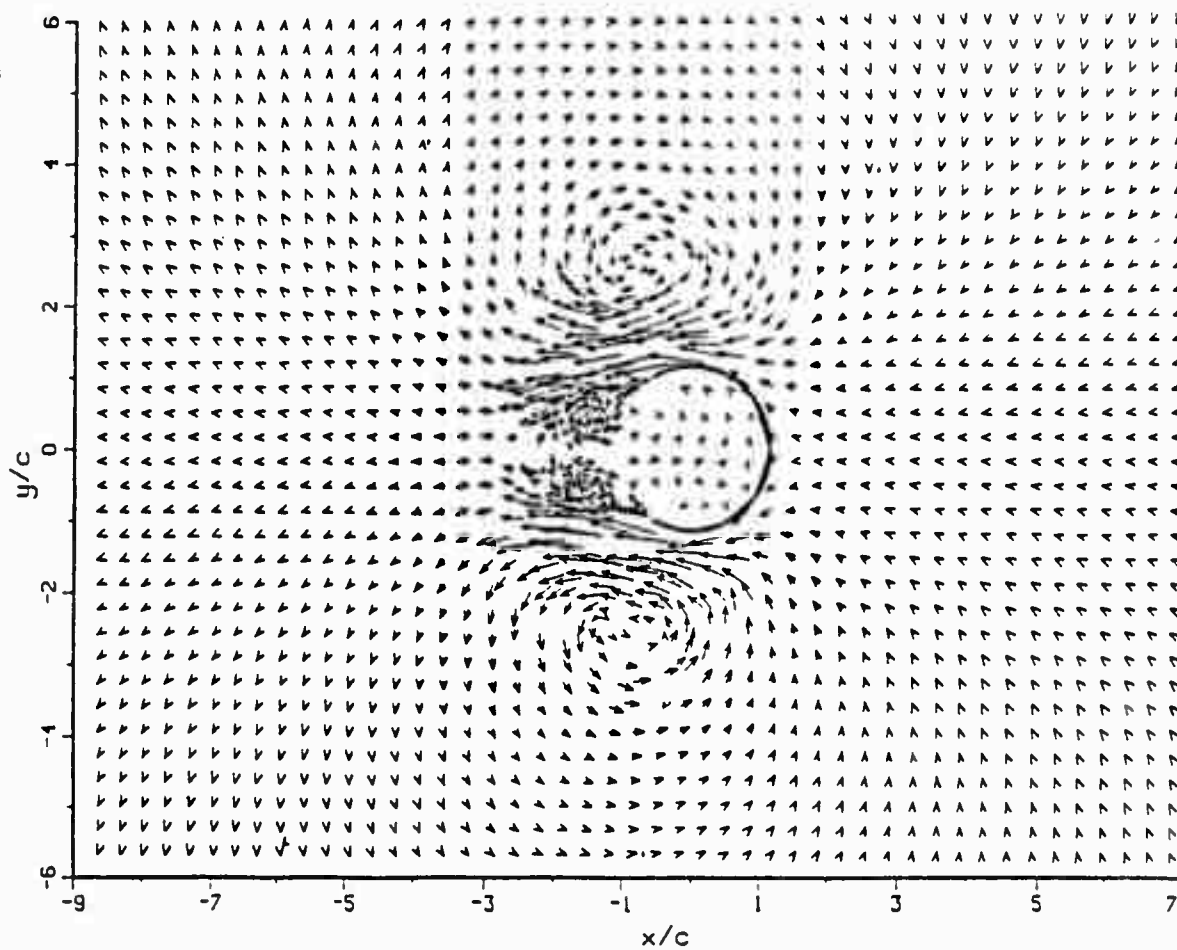
Fig. 71 Velocity Field at T* = 20 (Model C)

158

vortices partly because they have been in existence only for a short time and partly because the vorticity flux is not as large as that in the primary shear layers. The primary and secondary vortices on each side of the camber form a counter-rotating couple and remove themselves rapidly from the field under the influence of their mutual induction velocity (see Fig. 71 at $T^* = 20$). Subsequently, the absolute value of the differential pressure begins to decrease. Eventually, the differential pressure reduces to zero everywhere on the camber as the conditions approach those of a body in a fluid at rest.

Figure 72 shows a comparison of the calculated (through pressure integration) and measured drag coefficients as a function of T^*. The agreement between the two C_d values is not satisfactory, even during the period prior to the onset of deceleration. The fundamental reason for this disagreement is that not enough physics has yet been built into the numerical model to deal with either the boundary layer development during the early stages of the motion or with the back-face separation during the later stages of the motion.

Unlike the previous cases, the initial rise in the measured drag is followed first by a sharp decrease and then by a rise to a larger maximum. Subsequently, the
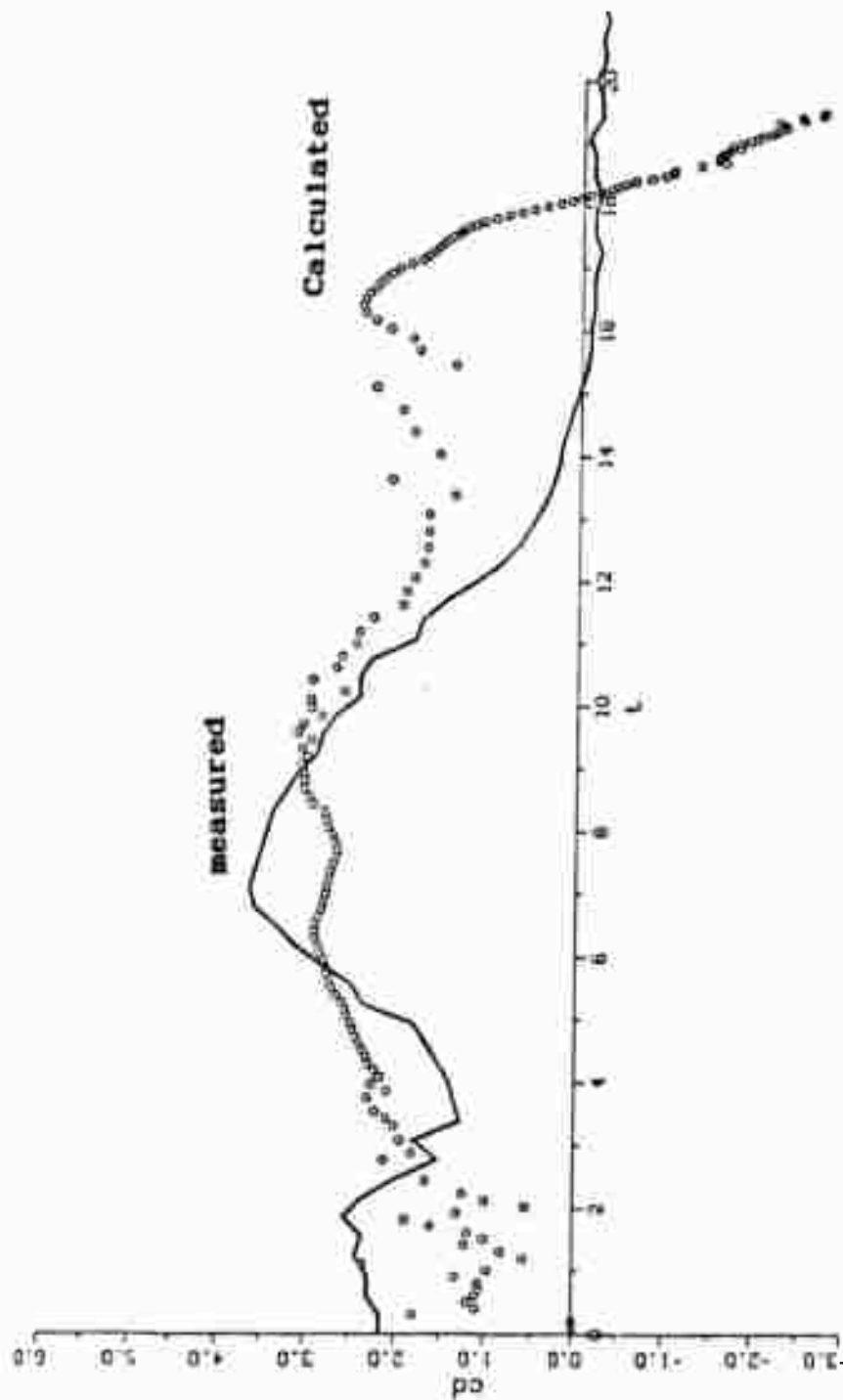
Fig. 72 Comparison of the measured and Calculated
Drag Coefficients (Model C)

160

drag coefficient decreases rapidly at the onset of deceleration, goes through zero near the middle of the deceleration period, and through a relatively small minimum (negative) value at the end of the deceleration period (see Figs. 63 and 72). Subsequently, C_d gradually decreases to zero.

Figure 73 shows a sample sequence of the pictures depicting the growth and motion of the vortices behind the Model C (see Section 3.3). It is clear from the first few frames that the flow **does not separate immediately at the sharp edges of the camber** as in the previous two cases. The separation begins at the bottom stagnation point (see the 4th and 5th frames) and leads to the formation and growth of two small vortices (see the frames 7-12). The initial rise of the drag is partly due to the acceleration of the flow and partly due to the formation of these two small vortices. Subsequently, these vortices move towards the rear of the camber (the time at which the drag decreases sharply) and the separation points move rapidly to the edges of the camber (see frames 13 and 14). There is a time period during which there are four vortices in the wake (the two small vortices and the two larger ones, resulting from the separation at the sharp edges), (see frames 12-16). Subsequently, the small scale vortices are overtaken by

Fig. 73 Evolution of the Flow Field about the Model C
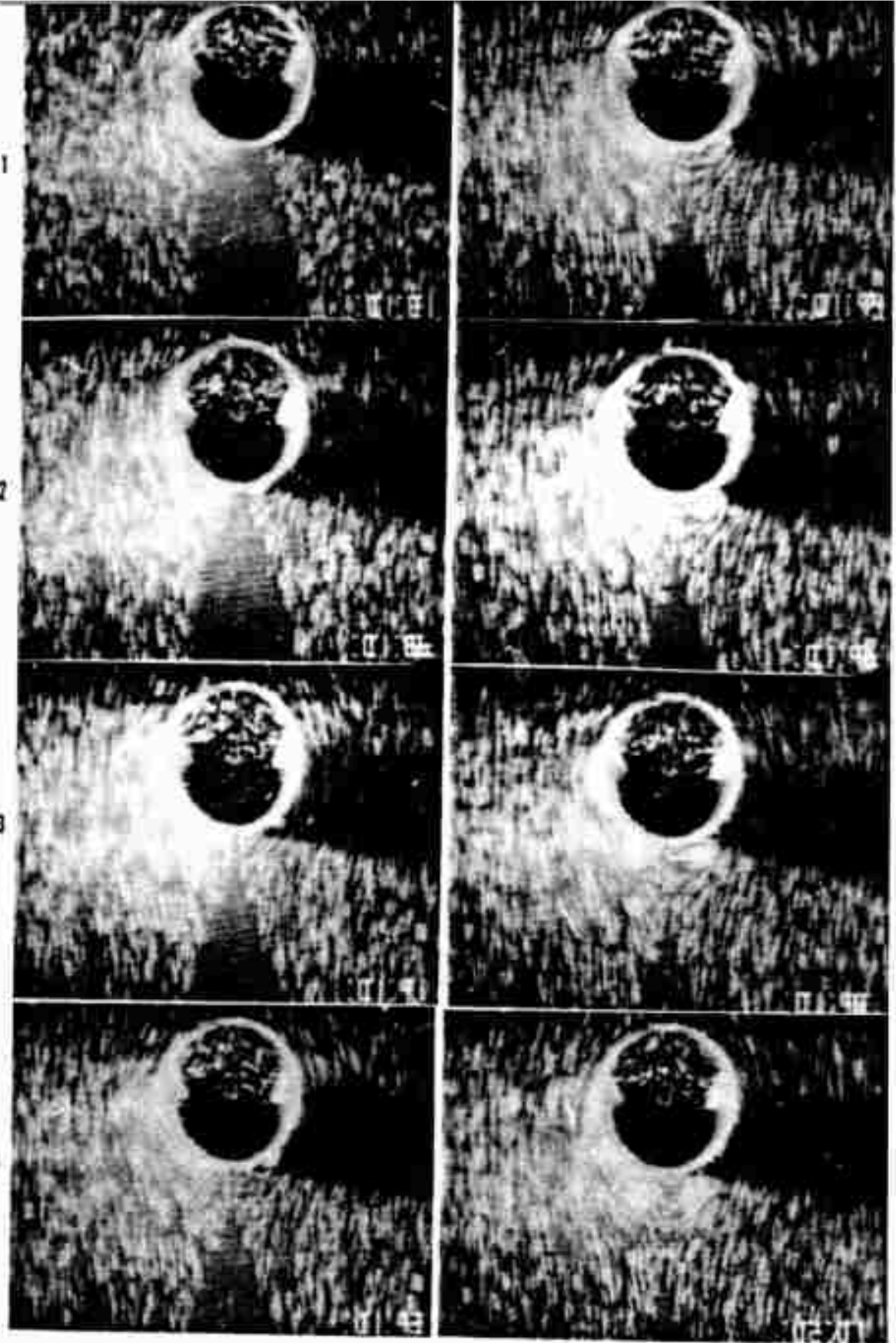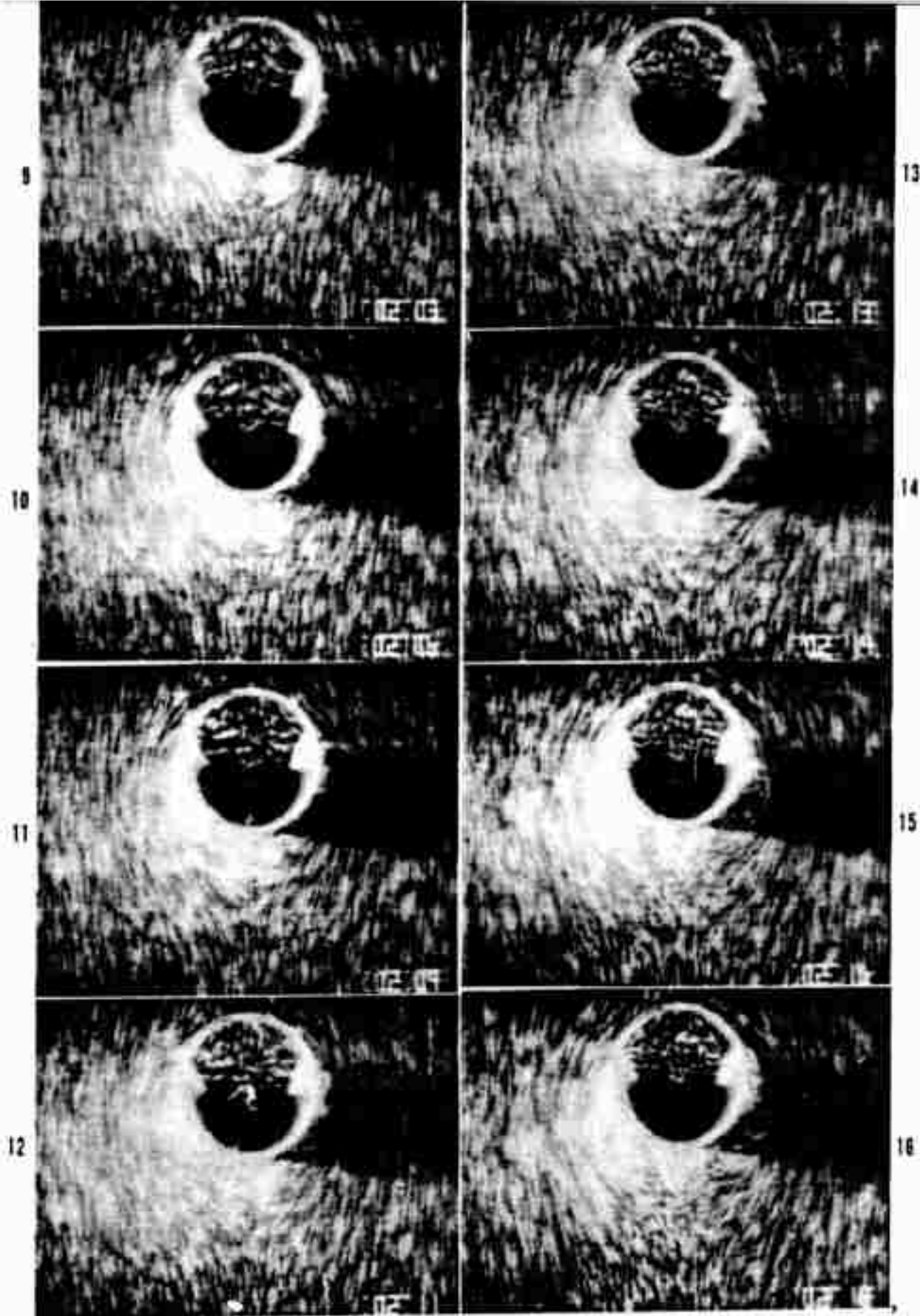(Continued)

162

Fig. 73   Evolution of the Flow Field about the Model C
(Continued)

163

Fig. 73   Evolution of the Flow Field about the Model C

164
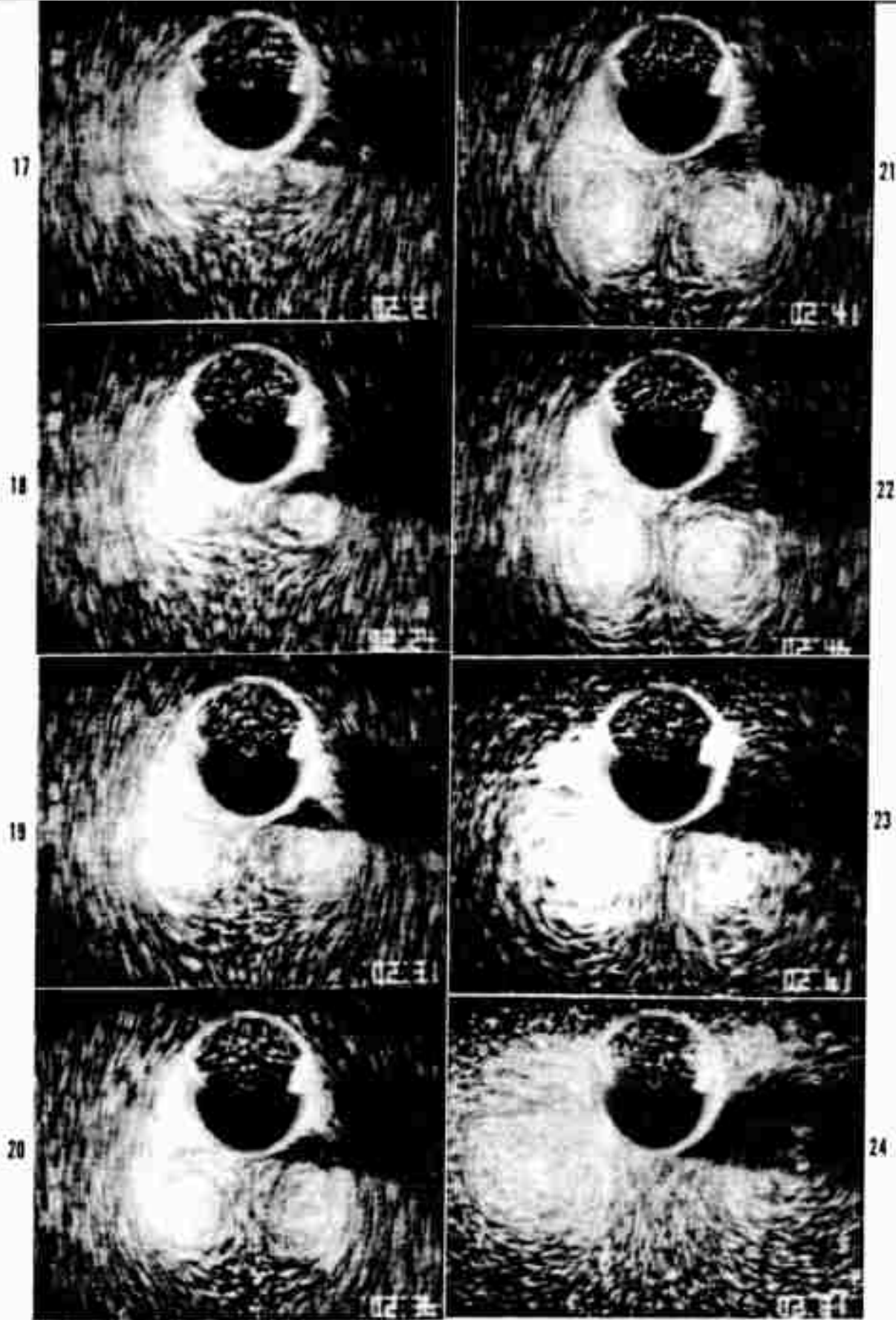
or merge with the larger ones (see frames 17-18). This merging takes place in a very short time (in about 0.03 seconds). The remaining vortices grow rapidly and give rise to two relatively large regions of secondary separation near the rear edges of the camber (see e.g., frame 21). The vortices continue to grow until the onset of deceleration (at about the 22nd frame). Subsequently, the vortices move upward and sideways (see e.g., the 23rd and 24th frames). It is important to note that separation during the period of deceleration occurs not only at the sharp edges but also at the downstream face of the camber (at about 30 degrees downstream from the edges) partly due to the presence of the large after body (240 degree arc) and partly due to the large velocities induced on it.

The foregoing explains in part the reason for the differences between the measured and calculated forces even during the early stages of the motion. The disagreement between the measured and predicted C_d values during the later stages of the motion is partly due to the carry-over effect of the earlier stages of the numerical simulation (history effects dictated by the model), partly due to the development of strong three-dimensional instabilities in vortices during the deceleration period, and partly due to the occurrence of

165

back-face separation. As noted earlier, the effect of the back-face separation becomes progressively more pronounced as the included angle of camber increases. This is true for all bluff-body problems where the afterbody (the part of the body beyond the mobile or fixed separation points) is large. In this sense, the model C becomes one of the most challenging bluff-body shapes as far as the computational methods with vortices are concerned. The problem is further compounded by the fact that the ambient flow is not steady and the vortices return to the body during the period of deceleration. The understanding of the attendant consequences of this wake-return in numerical analysis (additional separations) and in nature (parachute collapse) constitute the essence of the investigation. Sufficient physics will have to be incorporated into the numerical model to deal with these complex problems on a rational basis. The introduction of an artificial reduction in circulation in order to account (albeit indirectly) for the effects of the three-dimensional instability is not considered to be one of the rational approaches, however small the required reduction may be. This has been avoided in the present analysis partly to keep the discrete vortex analysis free from ad hoc assumptions, partly to under-stand the fundamental physical reasons, and partly to

166

discover the shortcomings of the numerical method leading to the differences between the measured and calculated forces.

Figure 74 shows a sample comparison of the calculated and photographed flow fields at corresponding representative times ($T^* = 8.75$, 11.42, and 13.83). The agreement between the two flow fields, as judged by the positions of the vortices, is fair. The comparison of the vortex strengths and velocities at corresponding times is most desirable for more definitive conclusions.

It should be noted, for sake of completeness, that the lift force for the model C also was found to be negligible. As noted earlier, this is primarily due to the fact that there is not sufficient time for the development of alternate vortex shedding either during the period of steady flow or during the period of rapid deceleration.
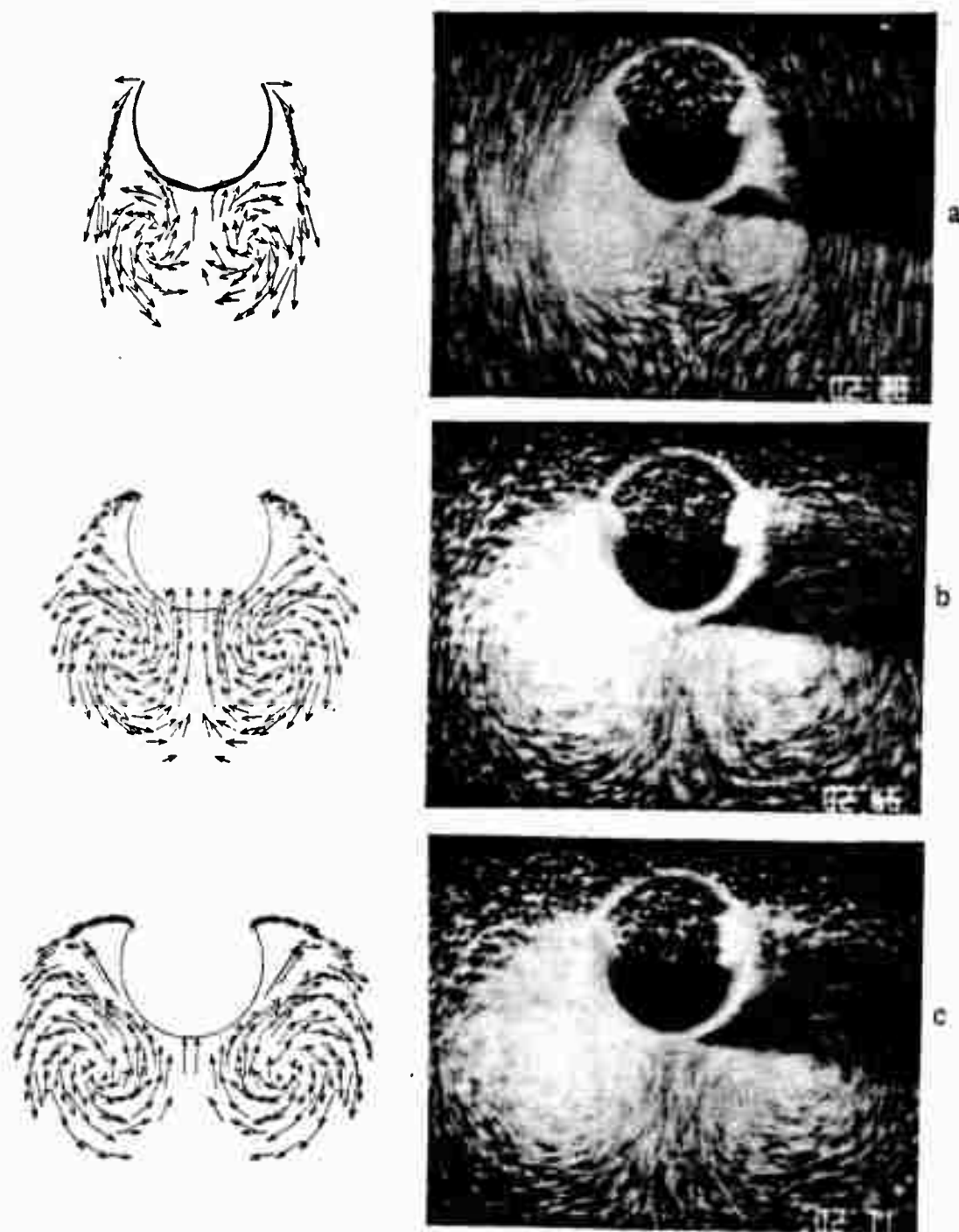
167

Fig. 74   Comparison of the Calculated and Photographed
          Flow Fields at (a) T* = 8.75, (b) T* = 11.42,
          and (c) T* = 13.83 (Model C)

168

7   CONCLUSIONS

A theoretical and experimental investigation of an Impulsively-started uniform flow, decelerating at prescribed rates, about two-dimensional cambered plates with included angles of 120, 180, and 240 degrees has been carried out.

The results have shown that:

1.   For a given camber, the drag coefficients prior to the onset of deceleration are nearly identical. The drag coefficients after the onset of deceleration are simply shifted in time by an amount equal to the difference between the durations of their steady states.

2.   For the Models A (120 degree camber) and B (180 degree camber), the drag coefficient decreases rapidly at the onset of deceleration, goes through zero near the middle of the deceleration period, and through a negative value at the end of the deceleration period. Then, the drag coefficient gradually decreases to zero.

3.   For the Models A and B, the flow separates at the sharp edges right from the start and remains there throughout the rest of the motion. Two, highly stable, symmetrical, primary vortices form and continue to grow during the periods of initial acceleration and subsequent steady fluid motion. The regions of secondary flow near the rear edges of the camber are quite small. During the period of deceleration, the vortices move towards the

camber, develop three-dimensional instabilities, and give rise to oppositely-signed circulation at the edges of the camber. Subsequently, the vortices continue to move sideways and the force acting on the camber reduces to zero as the vortices are diffused by both molecular and turbulent diffusion.

4. For the Model C (240 degree camber), the initial rise in the drag coefficient is followed by a sharp decrease and then by a rise to a larger maximum. Subsequently, the drag coefficient decreases rapidly at the onset of deceleration, goes through zero near the middle of the deceleration period, and through a relatively small (negative) minimum value at the end of the deceleration period.

5. For the Model C, the flow does not separate immediately at the sharp edges of the camber. The separation begins at the bottom stagnation point and leads to the formation and growth of two small vortices. Subsequently, these vortices move towards the rear of the camber (the time at which the drag coefficient decreases sharply) and the separation points move rapidly to the edges of the camber. Then two large primary vortices develop and quickly swallow the two small ones. As in the case of the Models A and B, the vortices become three dimensional during the period of flow

170

deceleration. This phenomenon takes place even when the total drag force acting on the parachute is still positive.

8   REFERENCES

Clements, R., (1973) "An Inviscid Model of Two-Dimensional Vortex Shedding," <u>Jour. of Fluid Mechanics</u>, Vol. 57, pp. 321-335.

Clements, R. R. and Maull, D. J., (1975) "The Representation of Sheets of Vorticity by Discrete Vortices," <u>Prog. in Aero. Sci.</u>, Vol. 16, pp. 129-142.

Cockrell, D. J., (1987) "The Aerodynamics of Parachutes," AGARD-AG-295.

Fage, A. and Johansen, F. C., (1928) "The Structure of the Vortex Sheet," <u>Phil. Mag.</u>, Vol. 7, No. 7, pp. 417-434.

Heinrich, H. G. and Saari, D. P., (1978) "Parachute Opening Shock Calculations with Experimentally Established Input Functions," **Jour. of Aircraft**, Vol. 15, No. 2, pp. 100-105.

Kiya, M. and Arie, M., (1977) "A Contribution to an Inviscid Vortex-Shedding Model for an Inclined Flat Plate in Uniform Flow," <u>Jour. of Fluid Mechanics</u>, Vol. 82, pp. 223-240.

Klimas. P. C., (1977) "Fluid Mass Associated with an Axisymmetric Parachute Canopy," **Jour. of Aircraft**, Vol. 14, No. 6, pp. 577-580.

Kuwahara, K., (1973) "Numerical Study of Flow Past an Inclined Flat Plate by an Inviscid Model," <u>Jour. Phys. Soc. Japan</u>, Vol. 35, pp. 1545-1553.

McVey, D. F. and Wolf, D. F., (1972) "Analysis of Deployment and Inflation of Large Ribbon Parachutes," **Jour. of Aircraft**, Vol. 11, pp. 96-103.

Mostafa, S. I. M., (1987), "Numerical Simulation of Unsteady Separated Flows," Ph. D. Thesis, Naval Postgraduate School, Monterey, CA.

Munz, P. M., (1987), "Unsteady Flow About Cambered Plates," M. S. Thesis, Naval Postgraduate School, Monterey, CA.

Muramoto, K. K. and Garrard, W. L., (1984) "A Method for Calculating the Pressure Field about a Ribbon Parachute Canopy in Steady Descent," AIAA 8th Aerodynamic Decelerator and Balloon Technology Conference, 2-4 April 1984, Hyannis, Mass., AIAA-84-0794.

172

Sarpkaya, T., (1967) "Separated Unsteady Flow about a Rotating Plate," In Developments in Mechanics, Vol. 4, pp. 1485-1499.

Sarpkaya, T., (1968) "An Analytical Study of Separated Flow about Circular Cylinders," Jour. of Basic Engineering, Trans. ASME, Vol. D-90, pp. 511-520.

Sarpkaya, T., (1975) "An Inviscid Model of Two-Dimensional Vortex Shedding for Transient and Asymptotically Steady Separated Flow over an Inclined Plate," Jour. of Fluid Mechanics, Vol. 68, pp. 109-128.

INITIAL DISTRIBUTION LIST

1. Defense Technical Information Center   2
    Cameron Station
    Alexandria, VA 22314-6145

2. Library, Code 0142   2
    Naval Postgraduate School
    Monterey, CA 93943-5000

3. Research Administration, Code 012   1
    Naval Postgraduate School
    Monterey, CA 93943-5000

4. Department Chairman, Code 69   2
    Naval Postgraduate School
    Monterey, CA 93943-5000

5. Prof. T. Sarpkaya, Code 69SL   10
    Mechanical Engineering
    Naval Postgraduate School
    Monterey, CA 93943-5000

6. LCDR Paul D. Munz   2
    39 Eagle Lane
    Hauppauge, NY 11788

7. Dr. Samir I. M. Mostafa   2
    Mechanical Engineering
    Naval Postgraduate School
    Monterey, CA 93943-5000

8. Sandia National Laboratories   25
    Parachute Division 1552
    Attn: Dr. James H. Strickland
    P. O. Box 5800
    Albuquerque, NM 87185

9. Dr. R. C. Maydew   2
    Sandia National Laboratories
    Code 1550
    P. O. Box 5800
    Albuquerque, NM 87185

10. Dr. D. D. McBride   2
    Code 1552
    Sandia National Laboratories
    P. O. Box 5800
    Albuquerque, NM 87185